

*Integrated Optical Distributed Bragg
Reflector and Distributed Feedback
Lasers in Er:LiNbO₃ Waveguides with
Photorefractive Gratings.*

Thesis

Submitted to the
Department of Physics, Faculty of Science
University of Paderborn, Germany
for the degree
Doctor of Philosophy (Ph.D/Dr.rer.nat)

By

Bijoy Krishna Das

Reviewers:

1. Prof. Dr. W. Sohler
2. Prof. W. von der Osten

Date of the Submission: 18.03.2003

Date of the Defence Examination: 24.04.2003

*Dedicated to my friends and well wishers
Chumki Saha, B. Umapathi, Lakshmi Bera, Bidyut Samanta, Satyajit Saha
Rajib, Makhan, Sidhu, Papu, Raju, Dilip, Bishu, Debu, and Bithika
who encouraged me to study Ph.D. in Germany*

Contents

1	Introduction	1
1.1	Background	1
1.2	Motivation	2
1.3	Organization of the Thesis	3
2	Photorefractive Gratings: Theoretical Analysis	5
2.1	Introduction	5
2.2	Photorefractive Effect in Fe:LiNbO ₃	5
2.3	Refractive Index Modulation by Two-Beam Interference	9
2.4	Thermal Fixing and Developing	12
2.5	Grating Response: Coupled Mode Theory Analysis	14
2.6	Conclusions	18
3	Doped Waveguides: Fabrication and Characterization	19
3.1	Introduction	19
3.2	Fabrication	19
3.2.1	Er-Diffusion Doping	22
3.2.2	Fe-Diffusion Doping	23
3.2.3	Fabrication of Ti-Indiffused Waveguides	25
3.2.4	Annealing	25
3.3	Characterization	26
3.3.1	Waveguide Loss and Mode-Size	26
3.3.2	Absorption and Gain	27
3.3.3	Amplified Spontaneous Emission (ASE)	30
3.4	Conclusions	31
4	Photorefractive Gratings: Fabrication and Characterization	33
4.1	Introduction	33
4.2	Fabrication	34
4.2.1	Grating Definition	34
4.2.2	Thermal Fixing and Development of Ionic Gratings	39
4.3	Properties of Fixed Gratings	40

4.4	Conclusions	47
5	Lasers with Photorefractive Gratings	49
5.1	Introduction	49
5.2	Basic Theory of Ti:Er:LiNbO ₃ Waveguide Lasers	49
5.3	DBR-Laser with One Grating	53
5.4	DBR Laser with Two Gratings	57
5.5	DFB Laser/Amplifier	62
5.6	DFB-DBR Coupled Cavity Laser	65
5.7	Conclusions	72
6	Summary and Conclusions	73

Chapter 1

Introduction

1.1 Background

Since the invention of the transistor in 1947, the development of integrated electronic circuits has led to increased reliability with increased performance and reduced cost, size, weight, and power requirements. With the expectation of realizing similar benefits for optical signal processing, computing, sensing, and communications, the research on integrated optical circuit (IOC) technology had been introduced after the invention of laser in 1960. For the first decade or so, the field of integrated optics research progressed very slowly, but in course of time the number of governmental, industrial, university, and other research laboratories involved in this field increased very rapidly.

The present research in the field of integrated optics is mainly focussed on finding a suitable material that can be used as a substrate for IOCs with higher functionality. Many kinds of materials and the corresponding process techniques have been considered. Some of the promising technologies are based on lithium niobate (LiNbO_3), glass (SiO_2 on Si), Gallium Arsenide (GaAs), polymers, etc.

Up to now, integrated optics technology based on ferroelectric LiNbO_3 is being widely investigated because of its attractive optical properties. This crystal of LiNbO_3 were grown for the first time by Ballman in 1965; it is not available in nature. The crystallographic structure and some fundamental physical properties of this ferroelectric crystal were intensively studied by Abraham et al in 1966 [1–5]. The basic experiments on acoustic wave propagation, electrooptic light modulation, optical second harmonic generation, parametric oscillation and holographic storage were performed between 1965-1968. Meanwhile, most of the physical and chemical properties of LiNbO_3 have been investigated and are understood very well. The most important crystallographic and physical parameters are also documented in the literature [6, 7].

The successful history of LiNbO_3 lies in the unique combination of excellent electrooptic, acoustooptic, nonlinear and photorefractive properties. Importantly, low-loss optical waveguide which is the back-bone of an integrated optical circuit (IOC), can be easily implemented by titanium (Ti) in-diffusion or by proton-exchange in this material. In fact, LiNbO_3 based integrated optic devices have been developed for optical switch arrays, fiber-optic gyroscope, cable TV (CATV) signal distribution, and long-haul telecommunications. Some of the device technologies have already been transferred to high-volume manufacturing in the latter two huge application markets [8].

Apart from the large number of passive/active devices already developed in LiNbO_3 , there is also a growing interest in rare-earth-doped optically pumped amplifiers and lasers [9–16] during the last years. In particular, erbium-doped titanium-indiffused lithium niobate (Ti:Er:LiNbO_3) laser sources ($1.53 \mu\text{m} < \lambda < 1.62 \mu\text{m}$) are attractive [17, 18]. Besides, cw Fabry-Perot lasers of high efficiency ($\sim 40\%$), acoustooptically tunable lasers, Q-switched lasers, actively mode-locked lasers, there have also been some attempts in developing narrow linewidth lasers [19, 20]. The approach was to integrate a grating structure in the waveguide to get single-frequency laser emission: this concept is routinely used to develop distributed Bragg reflector (DBR) and distributed feedback (DFB) lasers in semiconductors [21–23] and fibers [24–30]. Single-frequency lasers have major applications in the field of heterodyne detection and in fiber-optic ultra-dense wavelength division multiplexed systems.

1.2 Motivation

The first DBR laser was reported in Ti:Er:LiNbO_3 using a surface relief Bragg grating [19]. Single-frequency laser emission was observed frequently during its operation. Afterwards, an integrated optical transmitter unit consisting of such a DBR laser and a Mach-Zehnder interferometer was also demonstrated [31]. This type of transmitter unit is essential for fiber-optic communications. But, due to the complicated fabrication technology, limited quality of the gratings and high scattering losses of these surface relief Bragg gratings, work has not been progressed any more in this direction.

Besides their application in lasers, gratings or more general, periodic structures can also be used for couplers, add/drop filters, switches, dispersion compensators, etc, in integrated optical circuits [32, 33]. Therefore, it is a great challenge to fabricate efficient periodic structures in LiNbO_3 channel waveguides. As the surface relief Bragg grating in LiNbO_3 waveguides mentioned above is found to have some problems, photorefractive gratings generated by an illumination with a periodic light pattern on the sample surface can be exploited. Fiber Bragg gratings are examples with a periodic index modulation induced in the photosensitive fiber core. They are now commercially manufactured and used for a variety of applications, including dispersion compensa-

tion and wavelength add/drop filters.

Recently, Becker et al. [20] demonstrated an attractive integrated optical DBR laser consisting of (i) a photorefractive Bragg grating in a Ti:Fe:LiNbO₃ section at one end, (ii) an amplifying Ti:Er:LiNbO₃ section in the middle and (iii) a broadband dielectric mirror at the other end. Although, single-frequency laser emission could not be achieved with this type of laser, the work has opened a new direction in LiNbO₃ based integrated optics. To follow this direction and to explore the new field of integrated optical lasers with photorefractive gratings was the main goal of this thesis.

1.3 Organization of the Thesis

This work contributes some extended studies on photorefractive Bragg gratings and their applications in developing different DBR and DFB lasers in Er-doped LiNbO₃ waveguides. Single-frequency laser emission has been achieved with a DBR-cavity comprised of two photorefractive Bragg gratings fabricated in Ti:Fe:LiNbO₃ waveguide sections [34, 35]. By writing a photorefractive grating in a Ti:Fe:Er:LiNbO₃ waveguide section, a DFB-laser/amplifier combination has been developed [36, 37]. Finally, an attractive single-frequency laser has been demonstrated with a DFB-DBR coupled cavity design [38, 39].

It was known from the previous work of Becker et al [20] that an efficient photorefractive Bragg grating can be fabricated in Ti:Fe:LiNbO₃ with a grating vector parallel to the Z-axis (c-axis). To take this advantage, we choose to develop all of our devices with Z-propagating waveguides on X-cut LiNbO₃ wafers. Since single-mode Ti:LiNbO₃ waveguide fabrication is well-established and very good quality waveguides can be fabricated in our group (Prof. W. Sohler, Applied Physics, University of Paderborn, Germany), the work was mainly concentrated on the optimization of the fabrication of photorefractive Bragg gratings and the integration of such gratings with erbium-doped amplifier sections to develop different types of narrow linewidth lasers. Accordingly, the entire thesis is organized into the following four main chapters.

In Chapter 2, the origin of the photorefractive effect in LiNbO₃ and the principle of refractive index grating formation in Fe:LiNbO₃ are presented, respectively. Besides, the coupled mode theory allows us to investigate the optical properties of a Bragg grating without gain (in a Ti:Fe:LiNbO₃ waveguide) and with gain (in a Ti:Fe:Er:LiNbO₃ waveguide). Chapter 3 is dedicated to the fabrication and characterization of three differently doped waveguides, i.e, Ti:Fe:LiNbO₃, Ti:Er:LiNbO₃, and Ti:Fe:Er:LiNbO₃. The fabrication and characterization of thermally fixed photorefractive gratings are discussed in Chapter 4. Finally, in Chapter 5, four different types of DBR and DFB lasers are described individually with device structure and properties.

Chapter 2

Photorefractive Gratings: Theoretical Analysis

2.1 Introduction

Photorefractive gratings are generated inside electro-optic crystals upon the incidence of a periodic light pattern via a “photorefractive effect”. The photorefractive effect is an optical phenomenon for which the local index of refraction is changed by the spatial variation of the light intensity. The spatial index variation of the crystal leads to the distortion of the wavefront of propagating light. Therefore, the photorefractive effect is sometimes referred as “optical damage”. In fact, this photorefractive optical damage is a bottle-neck for some of the integrated optical device applications based on congruently grown LiNbO_3 crystal [40].

However, the photorefractive effect has shown to be very useful for high density optical data storage in LiNbO_3 [41, 42]. Utilizing a similar concept as for the case of optical data storage, integrated optical Bragg gratings have been fabricated in single-mode LiNbO_3 waveguides [20, 43]. They are proved to be useful in filtering/reflecting light of very narrow spectral linewidth. Therefore, these integrated optical Bragg gratings are fabricated and investigated (see Chapter 4) for developing different types of DBR and DFB lasers in LiNbO_3 channel waveguides (see Chapter 5). A theoretical discussion is given in this chapter for understanding the origin of the photorefractive effect in LiNbO_3 , the principle of Bragg grating formation, and its response properties.

2.2 Photorefractive Effect in Fe:LiNbO_3

Although, the photorefractive effect is a common property of all ferroelectric crystals, it was observed first in LiNbO_3 during the 1960s [44, 45]. Since that time this crystal is widely investigated to learn about the origin of its photorefractive effect. The mechanisms of this photorefraction in LiNbO_3 is also known for long time [46].

The origin of the photorefractive effect arises from the migration of optically generated charge carriers, if the crystal is exposed to a spatially varying pattern of illumination with photons having sufficient energy. The driving forces of the charge migration or transport are considered to be (i) photovoltaic effect, (ii) drift, and (iii) diffusion. The charge transport produces a space charge separation, which then gives rise to a strong space-charge field. Such a field induces a refractive index change via the electro-optic (Pockels) effect of the crystal.

It was Glass [46] in 1978, who argued first in details about the existence of a photovoltaic effect in bulk LiNbO_3 . Later on, it was verified experimentally and explained theoretically that this photovoltaic effect plays the dominant role for the photorefractive effect in LiNbO_3 . Kukhtarev et al [47, 48] in their two landmark papers studied the holographic storage exploiting this photorefractive effect using nominally pure LiNbO_3 crystal. They also formulated some basic equations and solved them under different conditions. Their model allows to understand the dynamics of the photorefractive effect in all electrooptic materials.

The presence of iron (Fe) impurities in the ppm (< 10 ppm) range in nominally pure LiNbO_3 crystals plays a key role for its photorefractive properties [49]. The photorefractive sensitivity can be enhanced and/or controlled by additional doping of Fe in LiNbO_3 (Fe: LiNbO_3). Besides Fe, other divalent transitional metals like Cu, Mn, Cr, etc., can also create the photorefractive centers when incorporated into LiNbO_3 . But, Fe: LiNbO_3 is found to be very attractive for its higher photorefractive sensitivity.

The photorefractive effect in Fe: LiNbO_3 is based on three distinguished processes: (i) photo-excitation of electrons from a deep donor to the conduction band (Nb^{5+}), (ii) their transport and (iii) subsequently trapping into another photorefractive center. Once we identify the photorefractive centers then it will be easy to concentrate on the charge transportation, which is mainly determined by the characteristic photovoltaic effect and the photoconductivity [50].

There are two valence states of iron, Fe^{2+} and Fe^{3+} , found to be the active photorefractive centers when the light intensities are not very high ($I < 10^6 \text{ W/m}^2$) and $2.6 < E < 3.1 \text{ eV}$. In this case, no light-induced absorption changes are observed.

For higher light intensities ($I > 10^6 \text{ W/m}^2$) and higher photon energies ($> 3.1 \text{ eV}$), Nb^{4+} and Nb^{5+} in Li^+ sites, respectively, are produced as additional photorefractive centers. As a result, light-induced absorption changes are observed [51]. In fact, $(\text{Nb}^{5+})_{\text{Li}}$ and $(\text{Nb}^{4+})_{\text{Li}}$ together form a bi-polaron and can be dissociated into small-polarons in presence of strong light intensities causing the light-induced absorption changes.

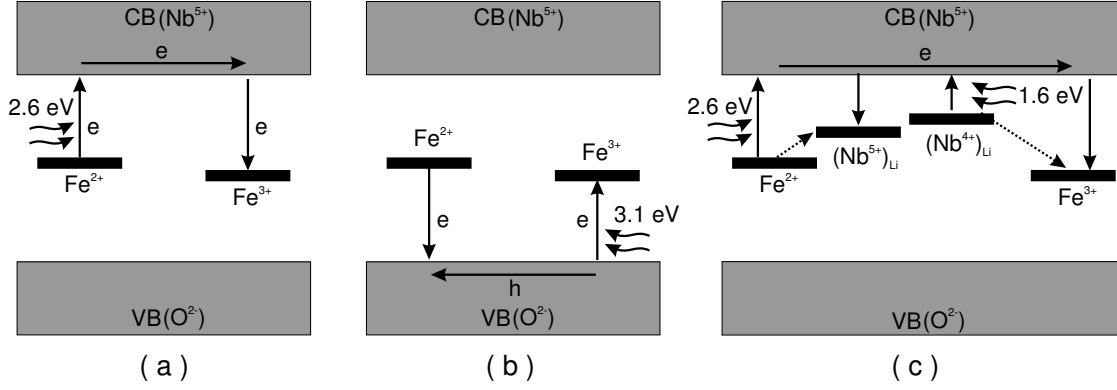


Fig. 2.1: Photorefractive centers in Fe:LiNbO₃. For the light intensity $I < 10^6$ W/m² (a) and (b). For the light intensities $I > 10^6$ W/m² (c). CB: conduction band, VB: valence band, e: electron, h: hole, $(Nb^{4+})_{Li}$: Nb⁴⁺ on Li⁺ sites, $(Nb^{5+})_{Li}$: Nb⁵⁺ on Li⁺ sites

Based on the two cases discussed above, the probable charge (electrons/holes) generation and their transport under the illumination of light with different photon energies are shown in Fig 2.1. Out of the three situations (a), (b), and (c) described in Fig. 2.1, (a) and (c) exhibit photorefractive effect and are supported by various reported experimental results. Only the situation of (a) has been considered for this thesis work because of its practical advantages.

As mentioned, the light-induced charge transport in doped LiNbO₃ is mainly determined by the photovoltaic effect [50]. Therefore, photo-illumination causes stationary currents without any external electric field. The photovoltaic current density \vec{j}^{pv} was found to be linear on light intensity I and hence bilinear in the polarization (unit) vector \vec{e} of the light, as pointed out by Belincher et al. [52]:

$$\vec{j}_i^{pv} = \beta_{ijk} I \vec{e}_j \vec{e}_k \quad (2.1)$$

The quantities β_{ijk} are components of the photovoltaic tensor. This tensor has four non-vanishing independent components in the case of LiNbO₃ which belongs to $3m$ point group:

$$\mathbf{j}_{pv} = \beta_{31}I(e_x^2 + e_y^2)z + \beta_{33}Ie_z^2z + \beta_{22}I[(e_y^2 - e_x^2)y - 2e_xe_yx] + 2\beta_{15}I(e_xe_zx + e_ye_zx) \quad (2.2)$$

The unit vectors e_x , e_y , and e_z describe the corresponding axes which are chosen in accordance with the standard of piezoelectric crystals [53]. However, the photovoltaic current density along the c -axis can be simplified for ordinary and extra-ordinarily polarized light:

$$\mathbf{j}_{pvo} = \beta_{31}I \quad \text{and} \quad \mathbf{j}_{pve} = \beta_{33}I \quad (2.3)$$

Here o and e refer to ordinary and extraordinary polarization, respectively.

The tensor description of the photovoltaic effects has been confirmed experimentally [54]. Though the largest current densities are obtained along the c -axis, the current perpendicular to c -axis, which is about an order of magnitude smaller, is also unambiguously identified by the dependence on the polarization angle. Only the tensor element β_{15} could not be obtained by these means because the corresponding current is modulated on account of birefringence effect. The values of β_{33} and β_{31} are almost comparable whereas the value of β_{22} is about one order of magnitude less in comparison. All the photovoltaic tensor elements are found to be linearly depend on the concentration of Fe^{2+} and with the photon energy when illuminated with photon energies between 2 eV ($\lambda \sim 620$ nm) - 3 eV ($\lambda \sim 412$ nm) [55].

A constant dc photocurrent as described by the equation (2.3) was measured along the c -axis of the crystal when it was uniformly illuminated [50]. This was the first experimental observation of the unidirectional charge transportation in LiNbO_3 . Accordingly, the open circuit photovoltage should be consistent with the following steady state equation (for ordinarily polarized light):

$$j = \beta_{31}I + \sigma_p E_{sat} = 0 \quad (2.4)$$

where σ_p measures the photoconductivity along the c -axis. The measured open circuit photovoltage:

$$E_{sat} = \beta_{31}I/\sigma_p \quad (2.5)$$

is just that required to account for the maximum index change in the same crystal. The photoconductivity σ_p is given by $\sigma_p = ne\mu_e$, where n is the electron density, e is the charge, and μ_e is the mobility of excited electrons in the conduction band. The density n can be derived from the rate equation and the equations for constant trap density assuming charge conservation [56]:

$$\frac{dA}{dt} = -rnA + (qsI + \beta_{th})D, \quad D + A = N, \quad A + n = N_c \quad (2.6)$$

Here A and D denote the concentrations of the empty ($c_{\text{Fe}^{3+}}$) and filled ($c_{\text{Fe}^{2+}}$) traps, r is the recombination coefficient, q is the quantum efficiency for generating a mobile electron upon absorption of a photon, s is the absorption cross section, β_{th} is the thermal generation rate, N is the total concentration of filled and empty traps and N_c is a constant concentration of compensation charge to maintain all over charge neutrality. If space-charge limiting effects and thermal excitations are neglected, we obtain in equilibrium: $n = (qsID)/(rA)$ and $\sigma_p \sim (ID)/A$, i.e., for $\text{Fe}:\text{LiNbO}_3$, $\sigma_p \sim c_{\text{Fe}^{2+}}/c_{\text{Fe}^{3+}}$.

2.3 Refractive Index Modulation by Two-Beam Interference

We have seen in the previous section that a photovoltage is generated under the illumination of light with suitable photon energy. This photovoltage causes refractive index change via the electrooptic effect. So, it is straightforward that a periodic refractive index modulation or an index grating (period = Λ) can be introduced by a spatially periodic illumination. Such a refractive index grating along the waveguide axis gives a narrow-band filter response around a Bragg wavelength (λ_B), similar to that of fiber Bragg gratings. The explicit expression for the Bragg wavelength can be derived easily. In fact, the grating vector ($|\vec{K}_G| = (2\pi)/\Lambda$) mediates matching between an input (\vec{K}_{in}) and an output (\vec{K}_{out}) wave:

$$\vec{K}_{in} - \vec{K}_{out} - \vec{K}_G = 0 \quad (2.7)$$

For the contradirectional Bragg reflection in a waveguide, we have: $|\vec{K}_{in}| = |\vec{K}_{out}| = (2\pi n_{eff})/\lambda_B$ and therefore,

$$\lambda_B = 2\Lambda n_{eff} \quad (2.8)$$

In LiNbO₃ waveguides, the Bragg response in the communication window ($\sim 1.55 \mu\text{m}$) can be achieved by a refractive index grating of periodicity $\Lambda \sim 350 \text{ nm}$. Such an intensity distribution of light along the surface of the waveguide can be made either using a phase mask or the two-beam interference method as shown in Fig. 2.2. We shall concentrate here only on two-beam interference method because of its practical flexibility in writing gratings of any specified periodicity (Λ), just by changing the angle (2θ) between the beams. The resulting period is given by:

$$\Lambda = \frac{\lambda_w}{2 \sin \theta} \quad (2.9)$$

where λ_w is the writing wavelength of the spatially periodic illumination.

Let us consider the simple situation of two coherent beams which are forming the interference fringes on the surface of a Ti-indiffused waveguide fabricated on a X-cut Fe:LiNbO₃ crystal (see Fig. 2.2). The interference fringes are made parallel to the Y-axis of the crystal whereas the waveguide propagation direction is parallel to the Z-axis. The sinusoidal intensity pattern along the waveguide (Z-axis) can be expressed as:

$$I(z) = I_0(1 + m \cos Kz) \quad (2.10)$$

where the spatial frequency $K = 2\pi/\Lambda$ and the modulation depth is $m(\leq 1)$. The dynamic grating formation can be modelled using the basic equations derived by Kukhtarev et al [47].

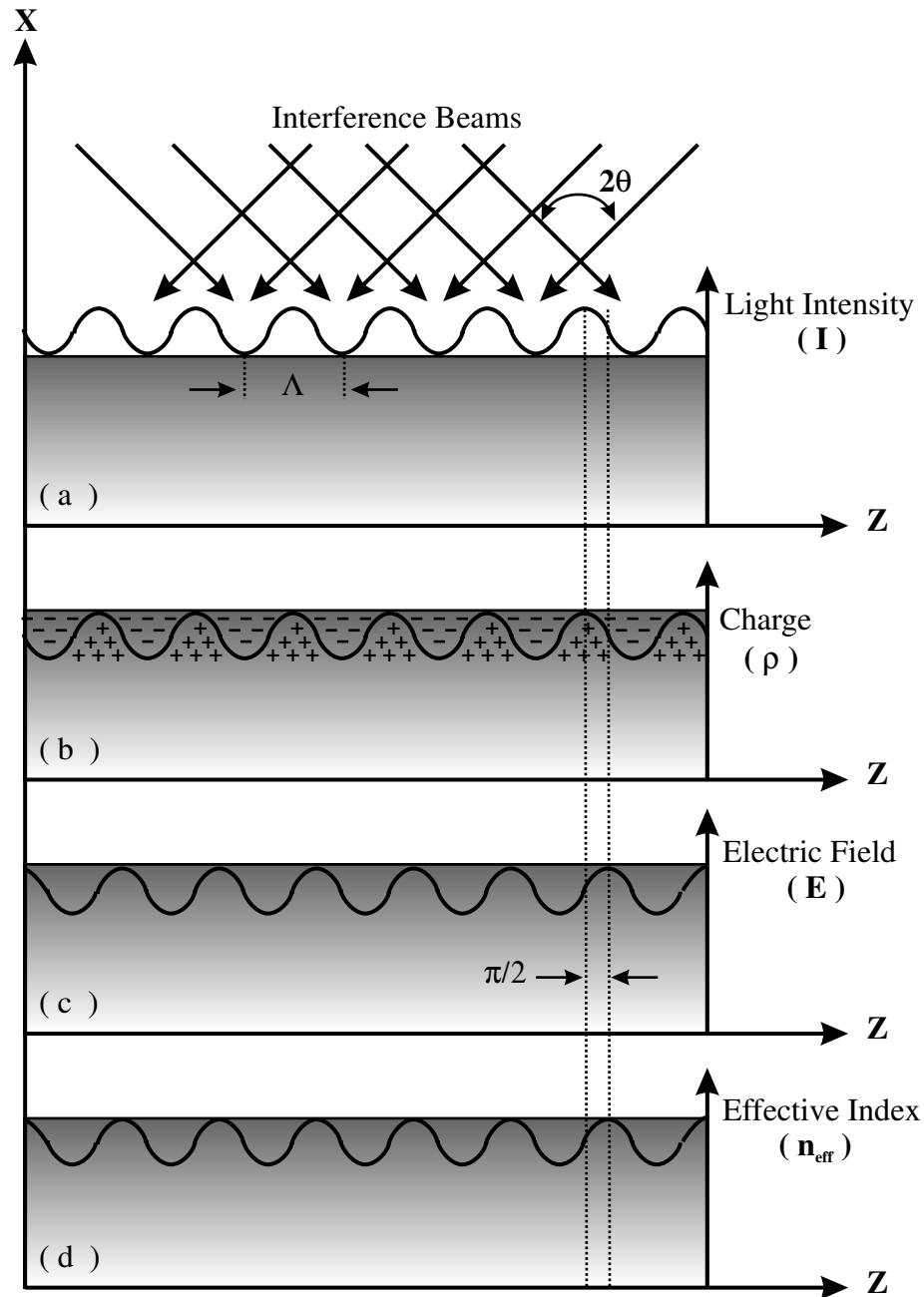


Fig. 2.2: Periodic refractive index modulation along the waveguide parallel to the Z-axis of the crystal by the surface illumination two-beam interference pattern; (a) sinusoidal spatial light intensity distribution, (b) resulting sinusoidal space-charge distribution, (c) sinusoidal spatial electric field and (d) sinusoidal refractive index modulation

According to the spatially periodic illumination, we can write down the z dependence of the evolved photoconductivity σ_p and of the free electron density n , respectively:

$$\sigma_p(z) = \sigma_{p0}(1 + m \cos Kz) \quad (2.11)$$

$$n(z) = n_0(1 + m \cos Kz) \quad (2.12)$$

where σ_{p0} and n_0 have constant values. If we define the space charge field generated by the photovoltaic effect as $E_{sc}(z, t)$, then the current density along the Z -axis obeys the following relation:

$$j_e(z, t) = eD_e \frac{\partial n(z)}{\partial z} + (\sigma_p + \sigma_d)E_{sc}(z, t) \quad (2.13)$$

Here, $D_e = (\mu_e k_B T)/e$ is the diffusion constant and σ_d the dark conductivity. The time dependence of $E_{sc}(z, t)$ is derived using the continuity and Poisson's equations, considering small diffusion length i.e $r_d \ll K^{-1}$ [55]:

$$E_{sc}(z, t) = \frac{k_B T m_0 K \sin Kz}{e(1 + m_0 \cos Kz)} \left[1 - \exp\left(-\frac{[\sigma_p(z) + \sigma_d]t}{\epsilon \epsilon_0}\right) \right] \quad (2.14)$$

where $m_0 = m/(1 + \sigma_d/\sigma_{p0})$, ϵ the static dielectric constant, k_B the Boltzman's constant, T the temperature. For a special case when $\sigma_d \ll \sigma_{p0}$, $m \ll 1$ and $t \rightarrow \infty$, equation (2.14) becomes:

$$E_{sc}(z, t) = \frac{k_B T}{e} m K \sin Kz \quad (2.15)$$

As a consequence of the periodic space charge field, the refractive index change for the ordinarily polarized light beams due to the Pockel's effect is:

$$\Delta n_o(z, t) = -\frac{1}{2} n_{effo}^3 r_{13} E_{sc}(z, t) \quad (2.16)$$

Here, n_{effo} is the ordinary effective refractive index of the waveguide and r_{13} the corresponding electrooptic coefficient. It is clear from equations (2.10) and (2.16) that the refractive index pattern is phase shifted by $\pi/2$ with respect to the light intensity distribution as shown in Fig. 2.2.

Sometimes, the light induced refractive index changes may be characterized by the saturation value, Δn_s , of the refractive index change and the sensitivity $S = d(\Delta n)/(d(I t))|_{t=0}$ at the beginning of illumination. These quantities are approximated by the following expressions [57]:

$$\Delta n_{so} = \frac{1}{2} \frac{n_{effo}^3 r_{13} m \beta_{31} I}{\sigma_p} \quad (2.17)$$

and

$$S = \frac{1}{2} \frac{n_{effo}^3 r_{13} m \beta_{31}}{\epsilon \epsilon_0} \quad (2.18)$$

2.4 Thermal Fixing and Developing

At room temperature a periodic illumination (along the waveguide) with light of a wavelength within the absorption band of Fe²⁺ ions ($\lambda_p = 470$ nm) modulates the concentration of Fe²⁺ (Fe³⁺) ions. This is possible by the transportation of excited free electrons from the brighter regions to the darker ones mainly due to the photovoltaic effect, which dominates along the optical-axis. In this way an index grating is induced by the periodic electronic charge distribution via the electrooptic effect. However, this type of index grating is volatile; it decays with time when the periodic illumination is removed. Therefore, holographic writing is normally done at elevated temperatures (~ 180 °C) to get a higher proton mobility leading to an ionic compensation of the original electronic space charge distribution. (H⁺ ions are usually induced in LiNbO₃ during crystal growth. However, its concentration can be enhanced by wet annealing of the crystal in a reducing ambient.) After fast cooling to room temperature, a uniform illumination helps to redistribute the electrons homogeneously. Consequently, an ionic grating remains inducing a phase-shifted replica of the index grating of the original electronic space charge. This type of refractive index grating is called a “fixed grating”. This thermal fixing technique was invented by Amodei et al in 1971 [41] and the role of H⁺ was confirmed by Vormann et al in 1981 [58]. In Fig. 2.3, the mechanisms of thermal fixing are shown schematically.

Now, we will analyze mathematically the thermal fixing mechanisms at the fixing temperature T_f under the periodic illumination as defined in Equn. (2.10) [59]. In this case we have to consider both types of charge transportation i.e., electrons and protons. The rate equations for the donors D (here Fe²⁺), the acceptors A (here Fe³⁺), the free electrons n and the protons H from equation (2.5):

$$-\frac{\partial D}{\partial t} = \frac{\partial A}{\partial t} = (\beta_{th} + qsI)D - rnA \quad (2.19)$$

$$\frac{\partial n}{\partial t} = (\beta_{th} + qsI)D - rnA + \frac{1}{e} \frac{\partial j_e}{\partial z} \quad (2.20)$$

$$-\frac{\partial H}{\partial t} = \frac{\partial j_h}{\partial z} \quad (2.21)$$

In the above equations the current densities j_e and j_h are given by:

$$j_e = e\mu_e nE + D_e e \frac{\partial n}{\partial z} - \beta_{31} ID \quad (2.22)$$

$$j_h = e\mu_h nE - D_h e \frac{\partial H}{\partial z} \quad (2.23)$$

where D_e and D_h are the diffusion constants electrons and protons, respectively. The steady distributions of donors, acceptors and protons can be written under the condition of $m \ll 1$ in Equn. (2.10):

$$D = D_0 + M_s \cos(Kz + \phi) \quad (2.24)$$

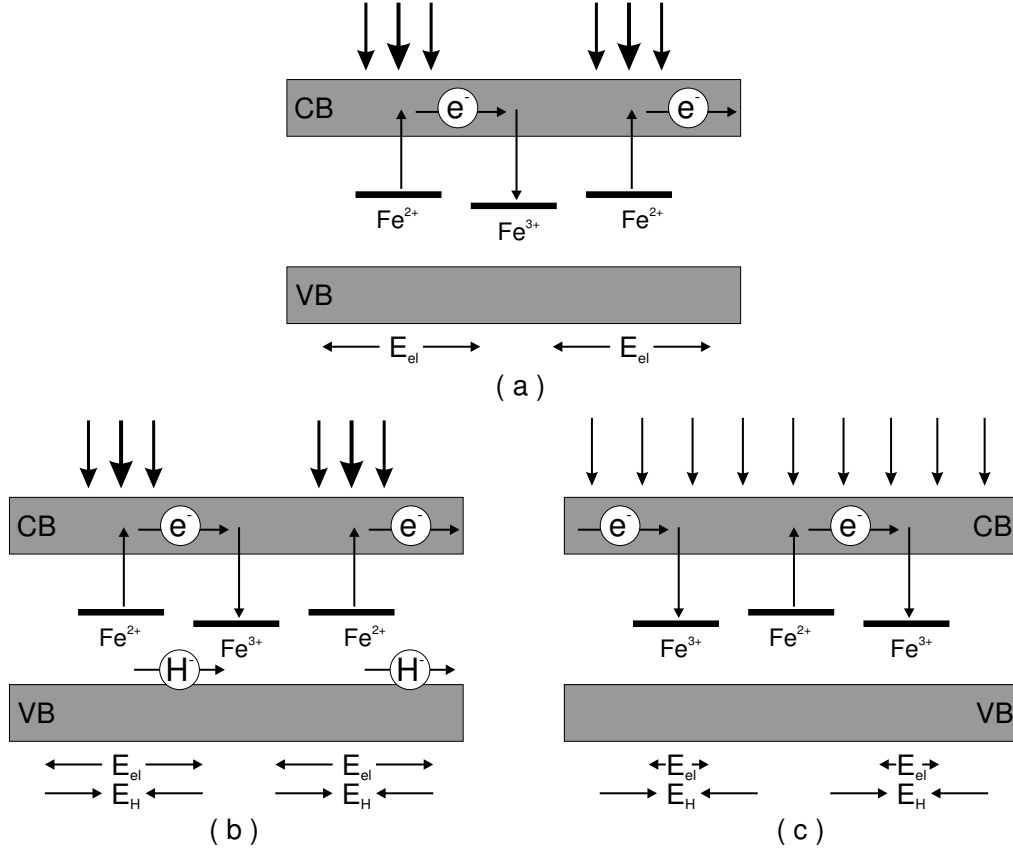


Fig. 2.3: Mechanisms of the photorefractive grating formation; (a) electronic grating at room temperature, (b) electronic and H^+ grating at fixing temperature (say, $\sim 180^\circ C$) and (c) development of fixed H^+ grating. E_{el} and E_{ion} are the electric fields generated by electronic and H^+ grating, respectively.

$$A = A_0 - M_s \cos(Kz + \phi) \quad (2.25)$$

$$H = H_0 - h_s \cos(Kz + \phi) \quad (2.26)$$

where D_0 , A_0 and H_0 are the initial concentrations of donor, acceptor and proton, respectively. Using three equations (2.24), (2.25) and (2.26) in the material equations for steady state (i.e., $\partial j_e / \partial z = 0$ and $\partial j_h / \partial z = 0$), the expressions for M_s and h_s are determined and they are related by:

$$h_s = \frac{M_s}{1 + (k_B T \epsilon / e^2)(K^2 / H_0)} \quad (2.27)$$

To develop the proton grating formed during the fixing process, the surface of the waveguide must be illuminated homogeneously at or near room temperature. The

final charge (proton) density amplitude after development is deduced as [59]:

$$\rho_d = \frac{h_s e}{1 + [e^2/(\epsilon\beta k_B T K^2)]} \quad (2.28)$$

with $\beta = 1/A_0 + 1/D_0$. Thus the amount of proton grating that is developed as charge grating depends on the donor and acceptor concentrations i.e., on β and the grating spacing $\Lambda = (2\pi)/K$. Accordingly, the amplitude of the sinusoidal refractive index modulation along z -coordinate is:

$$\Delta n_o = \frac{1}{2} n_{effo}^3 r_{13} \left[\frac{h_s e}{\epsilon K \{1 + e^2/(\epsilon\beta k_B T K^2)\}} \right] \quad (2.29)$$

It is to be noted that the refractive index modulation suffers a slow compensation due to the electronic dark conductivity (σ_d) in the absence of uniform illumination. However, continuous uniform illumination of lower intensity light ($I \sim 100$ mW/cm² and $\lambda \sim 470$ nm) can keep refreshing the proton grating for permanent device applications.

2.5 Grating Response: Coupled Mode Theory Analysis

Once the refractive index modulation is done along the surface of Ti-indiffused channel waveguide (see Fig. 2.4), coupled mode theory can be used to model the interactions between the grating structure and the guided modes [60]. From the theory, we learned that periodic refractive index perturbation causes the energy transfer among the modes. In particular, in a single-mode waveguide with a refractive index modulation discussed in the previous sections, the energy transfer happens between the forward- and backward propagating waves of identical polarization (TE \rightleftharpoons TE or TM \rightleftharpoons TM). In this case, energy can not be transferred between the modes of orthogonal polarizations (TE \nrightarrow TM), although, a single-mode waveguide is capable of guiding both the polarizations (TE and TM). So, it is sufficient to limit the discussion to one polarization (say, TE-polarization) for analyzing the grating properties.

The electric field of the forward- and backward propagating waves, $\vec{a}(x, y, z, t)$ and $\vec{b}(x, y, z, t)$, respectively, can be represented by:

$$\vec{a}(x, y, z, t) = A(z) \phi_a(x, y) e^{i(\omega t - \beta_a z)} \vec{e}_y \quad (2.30)$$

$$\vec{b}(x, y, z, t) = B(z) \phi_b(x, y) e^{i(\omega t + \beta_b z)} \vec{e}_y \quad (2.31)$$

Here, $A(z)$ and $B(z)$ are the z -dependent amplitudes of the forward- and backward propagating waves, respectively. $\phi_a(x, y) = \phi_b(x, y)$ represent the field amplitude distribution in the x - y plane and they can be derived from the intensity distribution

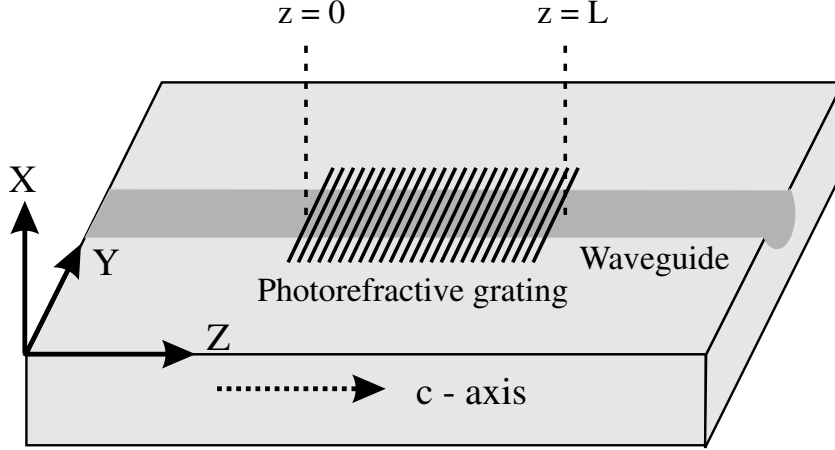


Fig. 2.4: Schematic structure of a Ti-indiffused optical waveguide with a photorefractive grating of length L on the surface of a X-cut LiNbO₃ crystal; the waveguide and the grating vector \vec{K} are parallel to the Z-axis (c-axis).

which is approximately Hermite-Gaussian along the x-axis and Gaussian along the y-axis according to the configuration sketched in Fig. 2.4 [61–65]. The magnitudes of the propagation constants are the same for the forward- and backward propagating waves, i.e., $|\beta_a| = |\beta_b| = \beta = (2\pi n_{effo})/\lambda$. Two counter propagating modes described by equations (2.30) and (2.31) are coupled via two differential equations [60]:

$$\frac{dA}{dz} = -i\kappa B e^{-i\Delta\beta z} \quad (2.32)$$

$$\frac{dB}{dz} = i\kappa A e^{i\Delta\beta z} \quad (2.33)$$

where the coupling coefficient κ is approximated by:

$$\kappa = \frac{\pi \Delta n_o}{\lambda} \quad (2.34)$$

and

$$\Delta\beta = 2\beta - \frac{2\pi}{\Lambda} \quad (2.35)$$

The solutions for $A(z)$ and $B(z)$ with the boundary condition $B(L) = 0$ are given by [60]:

$$A(z) = A(0) \left[\frac{s_\kappa \cosh\{s_\kappa(L-z)\} - i\frac{\Delta\beta}{2} \sinh\{s_\kappa(L-z)\}}{s_\kappa \cosh(s_\kappa L) - i\frac{\Delta\beta}{2} \sinh(s_\kappa L)} \right] e^{-i\frac{\Delta\beta}{2}z} \quad (2.36)$$

$$B(z) = A(0) \left[\frac{-i\kappa \sinh\{s_\kappa(L-z)\}}{s_\kappa \cosh(s_\kappa L) - i\frac{\Delta\beta}{2} \sinh(s_\kappa L)} \right] e^{i\frac{\Delta\beta}{2}z} \quad (2.37)$$

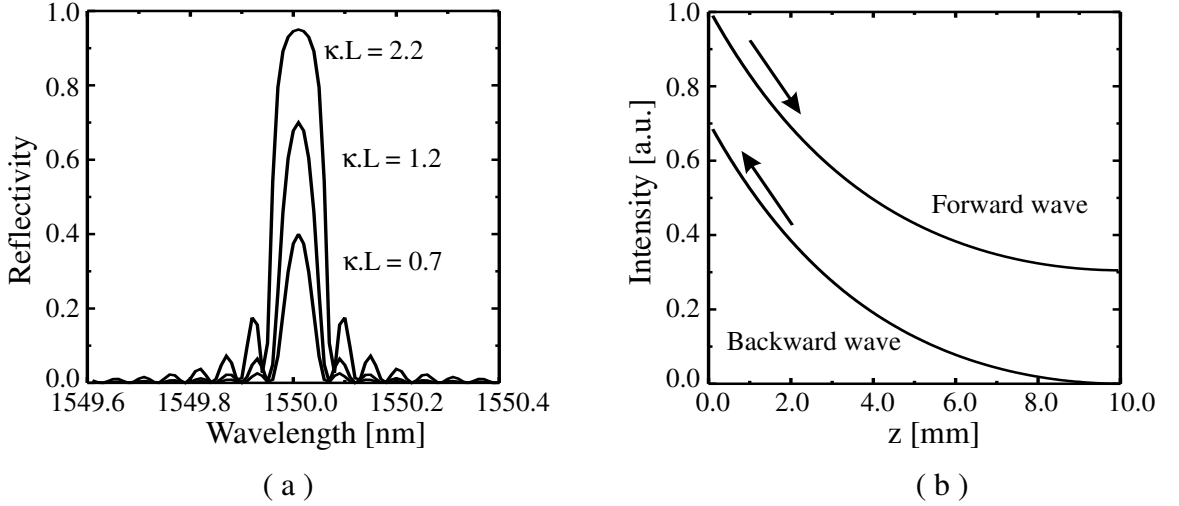


Fig. 2.5: Calculated grating response using coupled mode theory. (a) The reflectivity spectrum as a function of wavelength with κL as parameters and $\Lambda = 350$ nm. (b) The intensity evolutions of the forward- and backward propagating waves inside the grating section when $\Delta\beta = 0$. $\kappa : 1.2 \text{ cm}^{-1}$, $L: 1 \text{ cm}$.

with $s_\kappa^2 = \kappa^2 - (\Delta\beta/2)^2$. It is to be pointed out here that the above two equations are valid only in the waveguide region where the refractive index grating exists, i.e., $0 \leq z \leq L$. Hence, the expression of reflectivity is given by:

$$R = \left| \frac{B(0)}{A(0)} \right|^2 = \frac{\kappa^2 \sinh^2(s_\kappa L)}{s_\kappa^2 \cosh^2(s_\kappa L) + \left(\frac{\Delta\beta}{2}\right)^2 \sinh^2(s_\kappa L)} \quad (2.38)$$

From the above equation, it is evident that the reflectivity becomes maximum if $\Delta\beta = 0$ which is the condition of Bragg reflection and the corresponding Bragg wavelength λ_B can be deduced from the equation (2.35):

$$\lambda_B = 2\Lambda n_{effo} \quad (2.39)$$

The calculated reflectivity spectrum and intensity evolutions are plotted in Fig. 2.5. The results correspond to the effective refractive index $n_{effo} = 2.21$, a grating period $\Lambda = 350$ nm and κL as parameters. The reflectivity spectrum shows that there are some sidelobes around the actual Bragg response. The spectral spreading centered to the Bragg response is given by:

$$\delta\lambda_{Bragg} = \frac{2\lambda_{Bragg}\Lambda}{\pi} \sqrt{\left(\frac{\pi}{L}\right)^2 + \kappa^2} \quad (2.40)$$

In fact, by choosing appropriate values of the grating length L and the z-dependent functions $\Lambda = \Lambda(z)$ and $\kappa = \kappa(z)$, one can modify the Bragg response spectrum according to the requirements [66].

Up to now we have discussed the properties of the passive gratings fabricated in Ti:Fe:LiNbO₃ waveguides, i.e., without gain. We will see later on, these gratings have been used to develop the integrated optical DBR-lasers. But, the photorefractive gratings could be fabricated also in Ti:Fe:Er:LiNbO₃ waveguides. Presence of erbium atoms in the grating section is helpful to achieve distributed feedback gain. Therefore, DFB laser oscillation can also be demonstrated if sufficient gain and distributed feedback provided. In this case, the frequency dependent reflectivity of light R can be derived also using coupled mode theory [32]:

$$R(g, \nu) = \left| \frac{i\kappa \sinh(\gamma L)}{i\gamma \cosh(\gamma L) - \{\delta + i(g - \alpha)\} \sinh(\gamma L)} \right|^2 \quad (2.41)$$

where, $\gamma = \sqrt{\kappa^2 + \{(g - \alpha) - i\delta\}^2}$, $\delta = [2\pi n_{effo}(\nu - \nu_B)]/c$, ν the linear frequency, ν_B the frequency corresponding to the Bragg condition, α the scattering loss coefficient, and g the gain coefficient. From equation (1.39), we note that the oscillation frequencies of a DFB-laser are determined by the condition:

$$i\gamma \cosh(\gamma L) - \{\delta + i(g - \alpha)\} \sinh(\gamma L) \rightarrow 0 \quad (2.42)$$

For an example, the reflection contours of a DFB-structure of length $L = 1.8$ cm

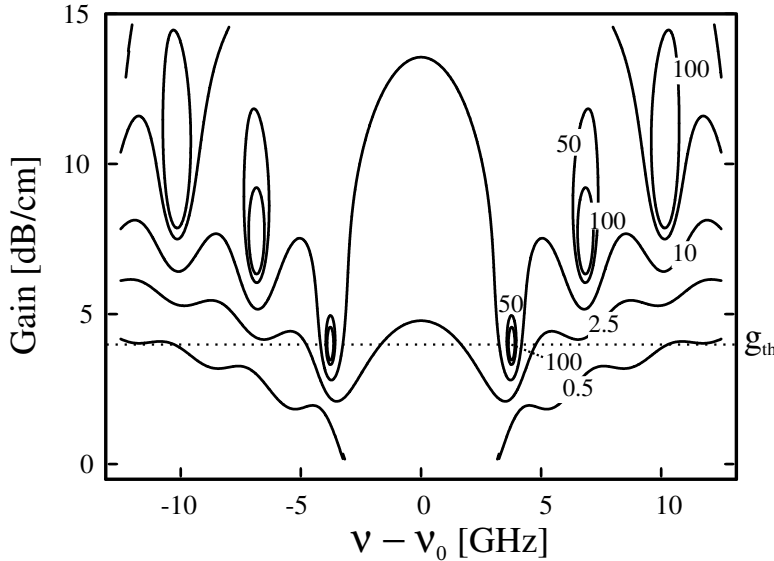


Fig. 2.6: Contours of constant reflectivity of a DFB laser structure, as a function of gain and frequency deviation from the Bragg condition. DFB-structure evaluated from coupled mode theory. For a length $L = 1.8$ cm and uniform coupling strength $\kappa = 0.85$ cm⁻¹, the threshold gain $g_{th} \approx 4$ dB/cm and $\Delta\nu \approx 8$ GHz for the two lowest order DFB-modes. Waveguide loss is assumed to be 0.2 dB/cm.

and uniform coupling coefficient $\kappa = 0.85$ cm⁻¹, have been plotted in the plane of

$\{g, (\nu - \nu_B)\}$ in Fig. 2.6. The threshold gain (g_{th}) and the frequency separation ($\Delta\nu$) of the two lowest order DFB-modes are estimated to be ~ 4 dB/cm and ~ 8 GHz, respectively.

2.6 Conclusions

In this chapter, the origin of the photorefractive effect, the principle of the Bragg grating formation, and their response properties (reflection and transmission) in both passive Ti:Fe:LiNbO₃ and laser-active Ti:Fe:Er:LiNbO₃ waveguides have been discussed theoretically.

The origin of the photorefractive effect in LiNbO₃ has been analyzed by considering only the Fe-impurities in the crystal. The principle of photorefractive Bragg grating formation in the waveguides by surface illumination with two beam interference pattern (holographic exposure) has been described.

As the photorefractive effect is a reversible phenomenon, i.e., the periodic (electron) space-charge field created during the illumination decays after the withdrawal of the illumination. This seems to be an issue for some practical applications. However, a spatially $\Lambda/2$ -shifted periodic (proton) space-charge field can be generated simultaneously by a thermal fixing method for permanent use of the grating structure. Therefore, the mechanisms of the thermal fixing process have also been described.

Finally, the coupled mode theory is outlined to analyze the grating properties. The reflection characteristics of a photorefractive Bragg grating in a passive Ti:Fe:LiNbO₃ waveguide have been obtained numerically. From the theoretical characteristics it is predictable that a photorefractive grating of length 1 cm could provide a peak reflectivity of $> 90\%$ and spectral bandwidth of < 80 pm if sufficient dose of a holographic exposure is given.

The reflection characteristics of a photorefractive grating in a laser-active Ti:Fe:Er:LiNbO₃ waveguide have also been investigated numerically. The results predict that an integrated optical DFB laser in Ti:Fe:Er:LiNbO₃ can be developed if sufficient gain is provided (~ 4 dB/cm).

Chapter 3

Doped Waveguides: Fabrication and Characterization

3.1 Introduction

In the previous chapter, we have seen from numerical simulations that distributed Bragg gratings can be realized in Fe-doped LiNbO₃ waveguides. Such a gratings in a passive Ti:Fe:LiNbO₃ waveguide section can be used either as narrowband wavelength filters or reflectors for integrated optical circuits. The presence of Er³⁺ in a Ti:Er:LiNbO₃ (or in a Ti:Fe:Er:LiNbO₃) waveguide can provide the optical gain in the emission band of $1.53 \mu\text{m} < \lambda < 1.62 \mu\text{m}$ [67–69].

Therefore, monolithic integration of a photorefractive Bragg grating in Fe-doped waveguide section and a laser-active Er-doped waveguide section has been investigated under the scope of this thesis work. Five different types of samples have been prepared, investigated (see Fig. 3.1), and later on they are used to develop different types of DBR and DFB lasers (see Chapter 4 and Chapter 5). In this chapter, we will concentrate on the sample preparation by diffusion doping of Er and Fe, waveguide fabrication by indiffusion of photolithographically defined Ti-strips and finally, the necessary characterizations.

3.2 Fabrication

Optical grade X-cut LiNbO₃ crystals of 1 mm thickness have been used for the fabrication of different types of doped waveguides. The waveguides have to be aligned parallel to the Z-axis to exploit the highest photovoltaic coefficients (β_{31} or β_{33}); that facilitates the fabrication of the photorefractive gratings with grating vectors along the same axis (Z).

For developing our four different types of DBR and DFB lasers (see Chapter 5),

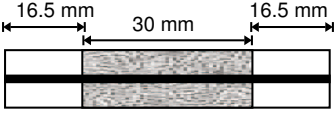
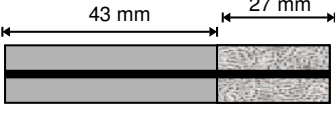
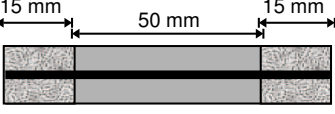
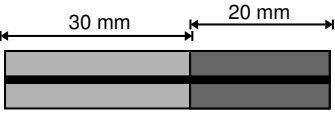
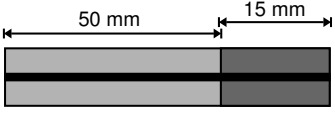
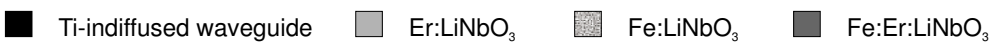
Sample	Er-diffusion	Fe-diffusion	Ti-diffusion
 <p>Pb66xz</p>	No erbium	Thickness: 40 nm $T_{diff.} : 1060 \text{ }^\circ\text{C}$ $t_{diff.} : 72 \text{ h}$	Thickness: 97 nm Width: 7 μm $T_{diff.} : 1060 \text{ }^\circ\text{C}$ $t_{diff.} : 7.5 \text{ h}$
 <p>Pb874xz</p>	Thickness: 15 nm $T_{diff.} : 1120 \text{ }^\circ\text{C}$ $t_{diff.} : 120 \text{ h}$	Thickness: 33 nm $T_{diff.} : 1060 \text{ }^\circ\text{C}$ $t_{diff.} : 72 \text{ h}$	Thickness: 97 nm Width: 8 μm $T_{diff.} : 1060 \text{ }^\circ\text{C}$ $t_{diff.} : 7.5 \text{ h}$
 <p>Pb106xz</p>	Thickness: 19 nm $T_{diff.} : 1130 \text{ }^\circ\text{C}$ $t_{diff.} : 120 \text{ h}$	Thickness: 41 nm $T_{diff.} : 1060 \text{ }^\circ\text{C}$ $t_{diff.} : 72 \text{ h}$	Thickness: 100 nm Width: 7 μm $T_{diff.} : 1060 \text{ }^\circ\text{C}$ $t_{diff.} : 7.5 \text{ h}$
 <p>Pb107xz</p>	Thickness: 19 nm $T_{diff.} : 1130 \text{ }^\circ\text{C}$ $t_{diff.} : 120 \text{ h}$	Thickness: 32 nm $T_{diff.} : 1060 \text{ }^\circ\text{C}$ $t_{diff.} : 72 \text{ h}$	Thickness: 100 nm Width: 7 μm $T_{diff.} : 1060 \text{ }^\circ\text{C}$ $t_{diff.} : 7.5 \text{ h}$
 <p>Pb145xz, Pb150xz</p>	Thickness: 20 nm $T_{diff.} : 1130 \text{ }^\circ\text{C}$ $t_{diff.} : 140 \text{ h}$	Thickness: 37 nm $T_{diff.} : 1060 \text{ }^\circ\text{C}$ $t_{diff.} : 72 \text{ h}$	Thickness: 100 nm Width: 7 μm $T_{diff.} : 1060 \text{ }^\circ\text{C}$ $t_{diff.} : 7.5 \text{ h}$
			

Fig. 3.1: Five different types of representative samples with their doping parameters.

a combination of any two types out of the three differently doped single-mode waveguides, i.e. Ti:Er:LiNbO₃, Ti:Fe:LiNbO₃, and Ti:Fe:Er:LiNbO₃ have been used. It will be evident afterwards that the Er is indiffused to create the laser-active medium, Fe to create photorefractive centers, and Ti to create guiding channels. That means, selective dopings of Er, Fe, and Ti (photolithographically defined) are prerequisites.

The easiest and most suitable way for selective doping of Er is thermal indiffusion [70]. Fe is also chosen for thermal indiffusion for its selective doping. For waveguide fabrication in LiNbO₃, two standard techniques are generally established; they are the proton exchange method and the method of Ti-indiffusion. Proton exchanged waveguides have a lower photorefractive sensitivity (because the electrooptic effect is reduced), higher scattering losses and can support only one polarization (extraordinary) of light. They are often used in nonlinear optical devices to take advantage of the lower photorefractive damage due to the second harmonics in the visible region. But, due

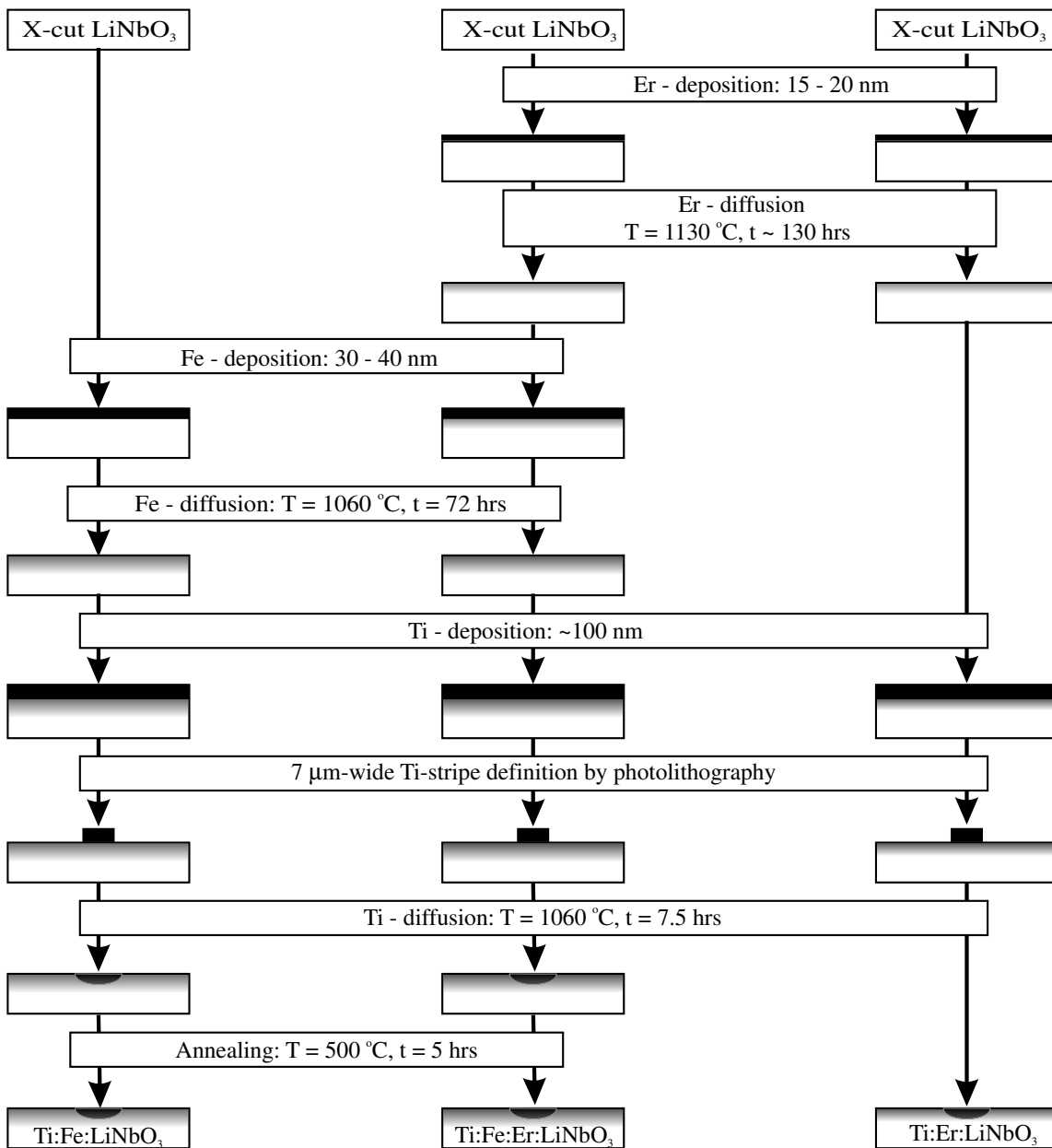


Fig. 3.2: Flow chart for the fabrication of the three different types of waveguides used for the laser development with fabrication parameters.

to higher scattering losses and guiding in only extraordinarily polarized light, these waveguides are disadvantageous for other integrated optic applications. Additionally, the proton-exchanged Er-doped LiNbO₃ waveguides are not suitable for lasers because there is an extreme reduction of the radiative lifetime of the ${}^4I_{13/2} \rightarrow {}^4I_{15/2}$ transition of Er³⁺. In comparison, Ti-indiffused waveguides have lower scattering losses (< 0.2 dB/cm), unchanged electrooptic properties, reasonably high radiative life-time of Er³⁺ (~ 2.6 ms for ${}^4I_{13/2} \rightarrow {}^4I_{15/2}$), and can support both polarizations of light. Therefore, Ti-indiffused waveguides are preferably used for this work.

All the dopants, Er, Fe, Ti are incorporated one after another by thermal indiffusion well below the Curie temperature of LiNbO₃ ($T_c \sim 1140$ °C) in the pre-defined locations of the sample surface. The diffusion depth and concentration profile of the individual dopants can be estimated from the diffusion theory of solids [71]. The theoretical depth concentration profile relevant to the parameters used for a specific dopant is given by:

$$c(x, t, D, d) = \frac{\rho N_A d}{m \sqrt{\pi D t}} e^{-\left(\frac{x}{2\sqrt{Dt}}\right)^2} \quad (3.1)$$

where ρ is the density of the deposited film, d thickness, m the molecular mass, N_A the Avogadro number and D the diffusion coefficient.

The above equation is valid for a diffusion time $t \gg t_d$, where t_d is the time by which the deposited film just exhausted and entered into the surface layer of the crystal during thermal indiffusion. As the diffusivity of Er is lowest, we have to indiffuse Er first, followed by Fe and Ti. In the following, the fabrication steps of differently doped waveguides are discussed in some more details (see Fig. 3.2).

3.2.1 Er-Diffusion Doping

To achieve a pre-defined Er-concentration profile, the knowledge of diffusion coefficients for the relevant temperatures is needed. Therefore, thin films of metallic Er were indiffused into the surface of X-cut LiNbO₃ crystals at different temperatures and for different durations [70]. The depth profiles of the Er-concentration were obtained either by secondary ion mass spectroscopy (SIMS) or by secondary neutral mass spectroscopy (SNMS) (see Fig. 3.3a). From these profiles the diffusion coefficients were determined and plotted versus the reciprocal diffusion temperature $1/T$ (Arrhenius plot, see Fig. 3.3b). From this plot an activation energy of 2.44 eV and a diffusion constant of 12×10^{-5} cm²/s were evaluated. All these results predict that the surface concentration of Er can be as high as 2.2×10^{20} cm⁻³ (limit of solid solubility), if the diffusion is carried out at 1130 °C.

The optimum diffusion parameters for developing our different types of DBR and DFB lasers have been deduced from the above results. Planar metallic film of Er of

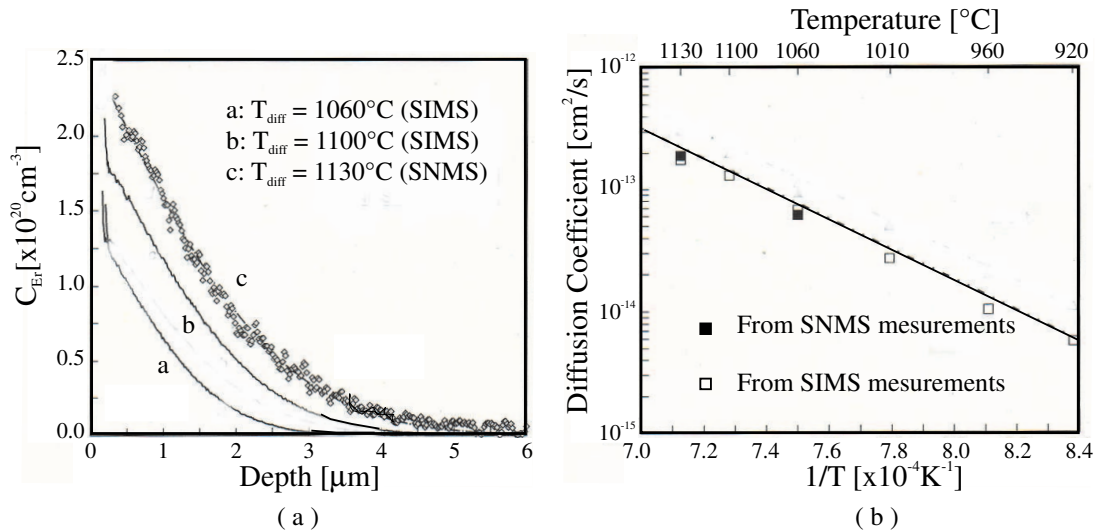


Fig. 3.3: (a) Erbium doping profiles by thermal indiffusion in X-cut LiNbO_3 crystals, and (b) Arrhenius plot of the diffusion coefficients of erbium perpendicular to the c-axis (along the X-axis) [70].

thickness $\sim 20 \text{ nm}$ is indiffused at 1130°C during $\sim 140 \text{ h}$ (depending on the corresponding thickness). This yields a nearly Gaussian concentration profile of $1/e$ depth of $\sim 4.5 \mu\text{m}$. The corresponding surface concentration of Er is $\sim 2.0 \times 10^{20} \text{ cm}^{-3}$. These results generate a good overlap of the Er-concentration profile with the Ti-indiffused waveguide to be fabricated later.

The standard deposition and diffusion processes developed earlier in our laboratory have been utilized. Metallic Er is e-beam evaporated at a rate of 0.1 nm/s and a pressure of $1.5 \times 10^{-7} \text{ mbar}$. After the deposition, thermal diffusion is carried out inside a quartz tube with flowing argon (1 litre/min), keeping the sample inside a platinum box. During the cooling down process, oxygen gas flows (1 litre/min) through the tube to compensate the oxygen deficiency underneath the sample surface which occurs during diffusion process.

3.2.2 Fe-Diffusion Doping

The Fe diffusion parameters were also measured in a similar experimental investigation as has been done for Er. The diffusion coefficient of Fe is determined by the indiffusion of metallic Fe layers into X-cut LiNbO_3 . Two different $\text{Fe}:\text{LiNbO}_3$ samples were prepared (with the collaboration of the group of Prof. E. Krätzig, University of Osnabrück, Germany), with different diffusion parameters (sample1 (X_{Fe1}): Fe-thickness - 171 nm , diff. temp. - 1060°C , diff. time - 3 h ; sample2 (X_{Fe2}): Fe-thickness - 30 nm , diff. temp. - 1060°C , diff. time - 3 h). For the sample1 the vacuum deposited metallic Fe-layer of a thickness of 171 nm represents a dopant source, which could

not be exhausted during the relatively short diffusion time of 3h. Therefore, an erfc-concentration profile is expected from diffusion theory. On the contrary, in case of sample2, the metallic Fe-layer of 30 nm thickness was completely indiffused into the crystal surface layer. Hence, a nearly Gaussian concentration profile was expected.

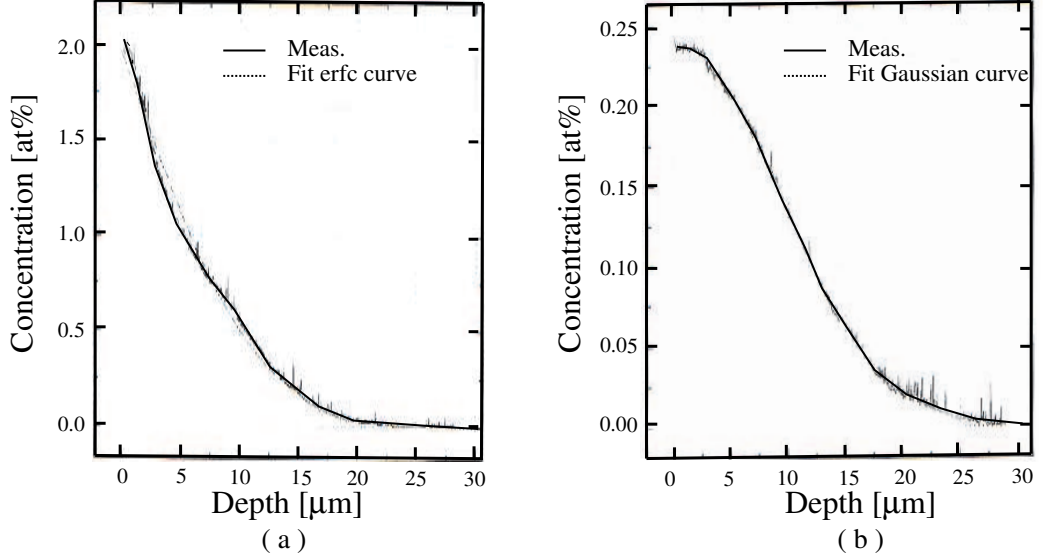


Fig. 3.4: The depth profiles of Fe atoms of the samples X_{Fe1} (a) and X_{Fe2} (b)

The Fe concentration profiles (depth) of both samples were measured using SNMS (measurements were performed in collaboration with the group of Prof. Müller, Soest); they are presented in Fig. 3.4 together with calculated results using the diffusion coefficient as fitting parameter. As expected an erfc-profile and a Gaussian distribution were obtained. From the comparison of the calculated and fitted results, a diffusion coefficient at 1060 °C of $3.85 \times 10^{-11} \text{ cm}^2/\text{s}$ was obtained.

Based on the above investigations, we have determined our optimum Fe-diffusion parameters suitable for both LiNbO_3 and Er:LiNbO_3 samples (assuming same diffusion coefficients in both cases). Usually, a vacuum-deposited planar metallic Fe film of thickness $\sim 35 \text{ nm}$ has been indiffused at 1060 °C during $\sim 75 \text{ h}$ (depending on the thickness). The resultant Fe-concentration has a Gaussian profile. The corresponding diffusion depth ($1/e$) and surface concentration are calculated to be $\sim 40 \text{ } \mu\text{m}$ and $\sim 6 \times 10^{19} \text{ cm}^{-3}$, respectively.

We have setup a special e-beam evaporation system and a diffusion furnace dedicated for preparing only the Fe-doped samples. First, the metallic Fe-layer is deposited on the sample surface at a rate of $\sim 0.5 \text{ nm/s}$ and at a pressure of $\sim 2.5 \times 10^{-6} \text{ mbar}$. Afterwards, the indiffusion is carried out in the furnace in flowing argon (1 litre/min), keeping the sample inside a platinum box. During the cooling down, oxygen gas flows

(1 litre/min) through the tube to compensate the oxygen deficiency underneath the sample surface which occurs during the diffusion process.

3.2.3 Fabrication of Ti-Indiffused Waveguides

Fabrication of a Ti-indiffused LiNbO₃ waveguide is a well established technique for a long time in our laboratory. The same Ti-indiffusion technology has been used for fabricating waveguides in Er:LiNbO₃, Fe:LiNbO₃, and Fe:Er:LiNbO₃. Same Ti indiffusion parameters can be used for all the three cases for single-mode waveguide fabrication.

First, a 100-nm-thick planar film of metallic Ti is vacuum deposited on the sample surface using an e-beam evaporation system at the rate of ~ 1 nm/s and at a pressure of $\sim 2.6 \times 10^{-7}$ mbar. Afterwards, about 1- μ m-thick positive photoresist was spin-coated uniformly over the Ti-film. The sample is then baked (pre-baking) at 90 °C for 30 min. After masking (parallel stripes of 7- μ m-width along Z-axis), a photolithographic exposure is given for 18 sec (UV-light $\lambda = 312$ nm). Post-baking is done at 120 °C for the duration of 45 min and then the sample is developed with a commercial developer (OPD5280) for 60 sec. The unwanted Ti-layer is etched by using EDTA (Ethylene Di-amino Tetra-acetic Acid) for the duration of 12 min at 30 °C. In this way, 7 μ m wide Ti-stripes parallel to the Z-axis are prepared. The residual photoresist on top of the Ti-stripe is removed with acetone followed by rinsing with deionized water. Finally, the thermal diffusion process is carried out at 1060 °C for 7.5 h, inside a furnace in argon flow (1 litre/min), keeping the sample in a platinum box. During cooling down of the furnace, oxygen gas flows as usual (1 litre/min) to compensate the oxygen deficiency underneath the sample surface which occurs during the indiffusion process.

3.2.4 Annealing

The photorefractive sensitivity of the sample is controlled by the subsequent annealing treatment in a proper ambient. This treatment helps to control the concentrations of Fe²⁺ ($c_{Fe^{2+}}$) and Fe³⁺ ($c_{Fe^{3+}}$). It is found from the theory that the ratio of ($c_{Fe^{2+}}/c_{Fe^{3+}}$) should be 0.1 or above to be able to fabricate a photorefractive Bragg grating efficiently [72].

We also observed in our experiments that annealing in a reducing atmosphere enhances the photorefractive sensitivity, because it increases $c_{Fe^{2+}}$. Therefore, an optimized annealing treatment of the sample is done in a reducing atmosphere (Ar, 1 litre/min) at 500 °C for the duration of $\sim 3 - 6$ h. Furthermore, the flowing argon is bubbled through water at 80 °C to increase the concentration of H⁺ in the sample, which is needed for the creation of a fixed grating [73].

The above annealing process does not influence the waveguide losses. This is confirmed experimentally by measuring the waveguide losses (see next section) before and after the annealing process.

3.3 Characterization

After the diffusion doping steps and the annealing process described in the previous section the optical properties such as waveguide losses, mode size, wavelength dependent absorption and gain, and the amplified spontaneous emission (ASE) are characterized.

3.3.1 Waveguide Loss and Mode-Size

The waveguide loss is measured by analyzing the low-finesse Fabry-Perot resonances as shown in Fig 3.5. The polished end faces of a passive waveguide i.e, either Ti:LiNbO₃ or Ti:Fe:LiNbO₃ forms a low-finesse Fabry-Perot cavity. The cavity is tuned by increasing the temperature of the sample as a function of time. A highly coherent single-frequency laser light at $\lambda \sim 1550$ nm (either from single-mode He-Ne laser or from an external cavity laser) is launched into the waveguide and the output is detected using an InGAs photodiode. The time-dependent output from the detector is recorded by a computer and the waveguide losses (mainly scattering loss) are easily evaluated from the data [74]. Typical waveguide losses of a Ti:Fe:LiNbO₃ waveguide are about 0.15 dB/cm (nearly polarization independent).

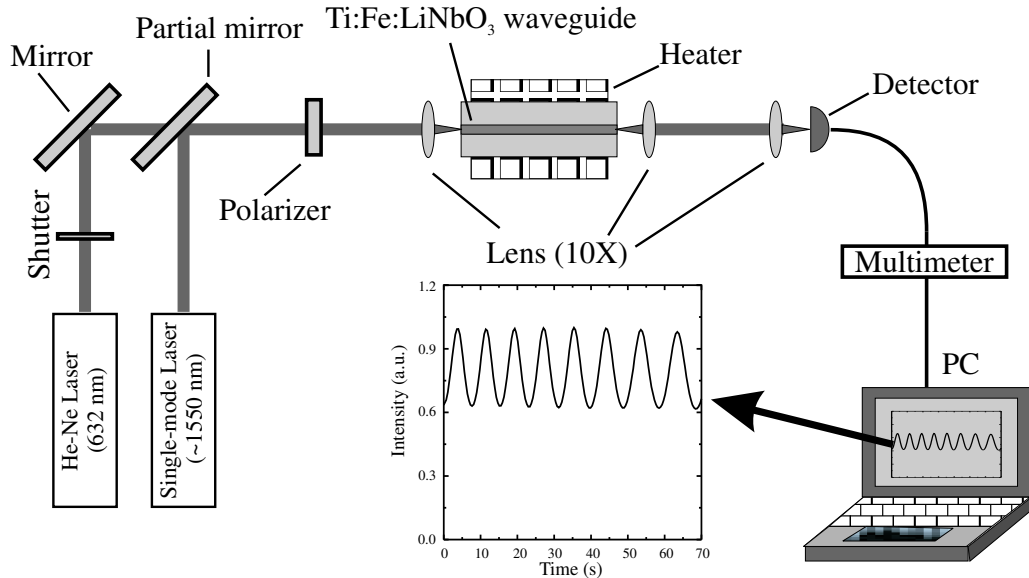


Fig. 3.5: Schematic diagram of the loss measurement setup utilizing the low-finesse Fabry-Perot contrast method.

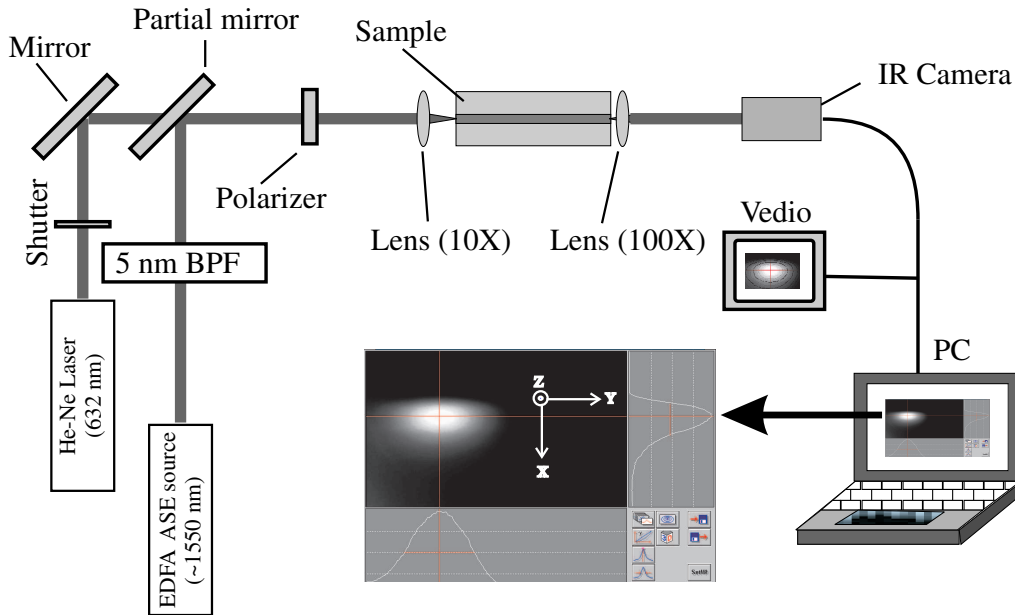


Fig. 3.6: Schematic diagram of the setup to measure the mode intensity profiles. BPF: band pass filter, IR: infrared, EDFA: erbium doped fiber amplifier, ASE: amplified spontaneous emission

The scattering loss of a Ti:Er:LiNbO₃ or Ti:Fe:Er:LiNbO₃ waveguide is estimated by subtracting the total losses (measured by the above mentioned method) and the absorption due to Er³⁺ (measurement to be discussed latter).

The mode-size of guided light is determined by measuring the near-field intensity distribution at the output end of the waveguide. In this case light from an incoherent amplified spontaneous emission (ASE) of an erbium doped fiber amplifier (EDFA) is filtered by a band pass filter (BPF) and launched into the waveguide. The purpose of using an incoherent light source is to avoid unwanted interferences. The output near-field pattern of the guided mode is magnified (100X) and imaged on to an infrared (IR) camera. The measured intensity profile confirms its single-mode properties. The typical polarization independent (nearly) mode-size (1/e full width) was measured to be $\sim 7.5 \mu\text{m}$ (along X-axis, Gaussian profile) $\times 4.5 \mu\text{m}$ (along Y-axis, Hermite-Gaussian profile) which is close to the mode-size of a standard single-mode fiber used in the communication systems (see Fig. 3.6).

3.3.2 Absorption and Gain

All optical transitions of Er³⁺ ions in an Er:LiNbO₃ crystal were experimentally observed long time ago (see Fig. 3.7) [75]. The most interesting transitions occur between the ground state ($^4I_{15/2}$) and the first excited manifold ($^4I_{13/2}$); the absorp-

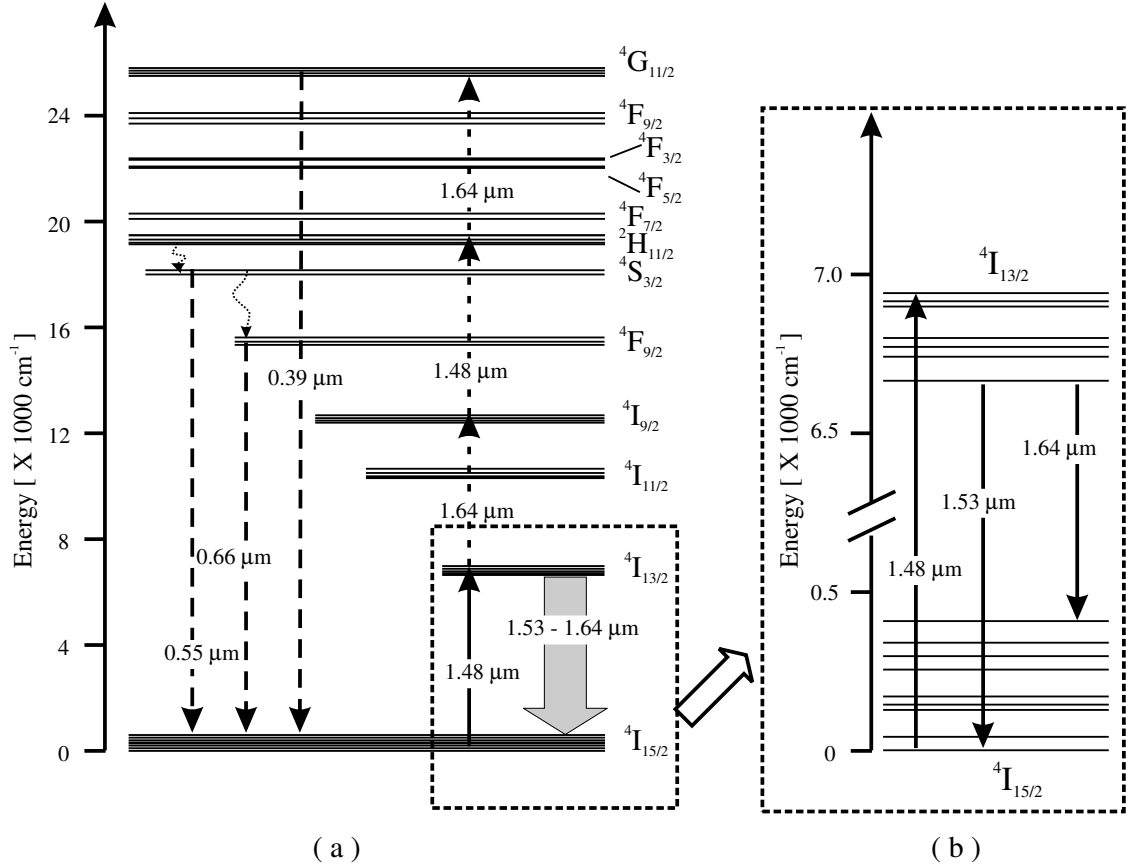


Fig. 3.7: (a) Erbium energy level diagram after Gabrielyan [75] with possible transitions if it is excited by $\lambda = 1.48 \mu\text{m}$ and (b) enlarged part of the diagram with the lower laser level ${}^4I_{15/2}$ and the upper laser level ${}^4I_{13/2}$. The energy scale is given in reciprocal wavelengths (cm^{-1}) as usual for spectroscopy.

tion/emission band ($1.42 \mu\text{m} < \lambda < 1.64 \mu\text{m}$) is well-matched to the communication wavelengths (centered at $\sim 1.55 \mu\text{m}$). The fluorescence lifetime of the ${}^4I_{13/2}$ -level was measured to be $\sim 2.6 \text{ ms}$ [76]. Due to the strong crystal field the (${}^4I_{15/2}$) and (${}^4I_{13/2}$) levels are splitted into manifolds with 8 and 7 closely spaced energy levels, respectively. At room temperatures these energy levels are occupied according to the Boltzman's distribution law. With a proper pumping a population inversion can be created between the levels (${}^4I_{15/2}$) and (${}^4I_{13/2}$) to exhibit a quasi two-level laser systems. However, if there is a population inversion between the levels (${}^4I_{15/2}$) and (${}^4I_{13/2}$), there are possibilities of excited state absorptions (see upwards pointing dashed arrows in Fig. 3.7). As a result, fluorescence can also be observed in the wavelength ranges $\sim 660 \text{ nm}$, $\sim 550 \text{ nm}$, and $\sim 390 \text{ nm}$ (see downwards pointing dashed arrows in Fig. 3.7).

The wavelength dependent absorption and emission cross-sections were measured

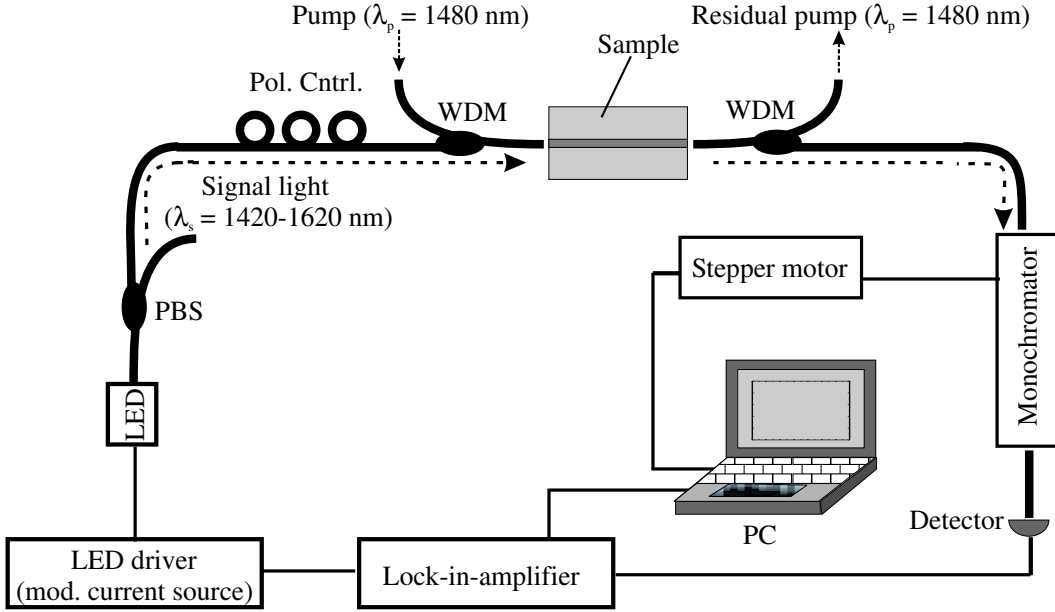


Fig. 3.8: Schematic diagram of the absorption/gain measurement setup. PBS: polarization beam splitter, Pol. Cntrl.: polarization controller, LED: light emitting diode, WDM: wavelength division multiplexer.

with α -polarized light ($\mathbf{E}, \mathbf{B} \perp c$ -axis and $\mathbf{k} \parallel c$ -axis) in a bulk Er-doped LiNbO₃ crystal [77]. The absorption cross-sections at $\lambda < 1.53 \mu\text{m}$ are clearly higher than the emission cross-section, whereas for $\lambda > 1.53 \mu\text{m}$ the situation is reversed. At $\lambda \sim 1.53 \mu\text{m}$, both the absorption and emission cross-sections are almost equal. Therefore, it is worth to mention here that optical gain can be easily achieved in the region of $1.53 \mu\text{m} < \lambda < 1.62 \mu\text{m}$ if an Er-doped waveguide is pumped at $\lambda = 1.48 \mu\text{m}$, where the absorption cross-section is relatively high. Absorption and gain of our Er-doped waveguides (either Ti:Er:LiNbO₃ or Ti:Fe:Er:LiNbO₃) have been investigated using the experimental setup schematically shown in Fig. 3.8.

The absorption was evaluated from the measured transmission of the waveguide. A low-power near-infrared light emitting diode (LED) has been used as a broadband light source. The input signal light was electronically modulated and the output from the waveguide was detected by a Lock-in-technique. Both the TE and TM polarization of lights showed similar characteristics due to Z-propagation (α - polarization) of the guided mode. Fig. 3.9a shows the absorption characteristics of a 5 cm long Ti:Er:LiNbO₃ waveguide for TE polarization (sample: Pb106xz). At $\lambda \sim 1480 \text{ nm}$ (used as pump for our laser operations), the absorption is -7 dB.

For gain measurements the pump light ($\lambda_p = 1480 \text{ nm}$) is coupled to the waveguide by using a wavelength division multiplexer (WDM) (see Fig. 3.8). Sufficient pump light creates a population inversion inside the waveguide and hence any sig-

nal light ($1.53 \mu\text{m} < \lambda < 1.62 \mu\text{m}$) can be amplified. The gain characteristics were measured in the same 5 cm long Ti:Er:LiNbO₃ waveguide (sample:Pb106xz). At 85 mW of coupled pump power, a peak gain of about 7 dB at 1531 nm (and ~ 3 dB at 1561 nm) wavelength was achieved (see Fig. 3.9b); both, pump and signal were TE-polarized. There were only small differences in the gain characteristics for other combinations of the polarization of pump and signal.

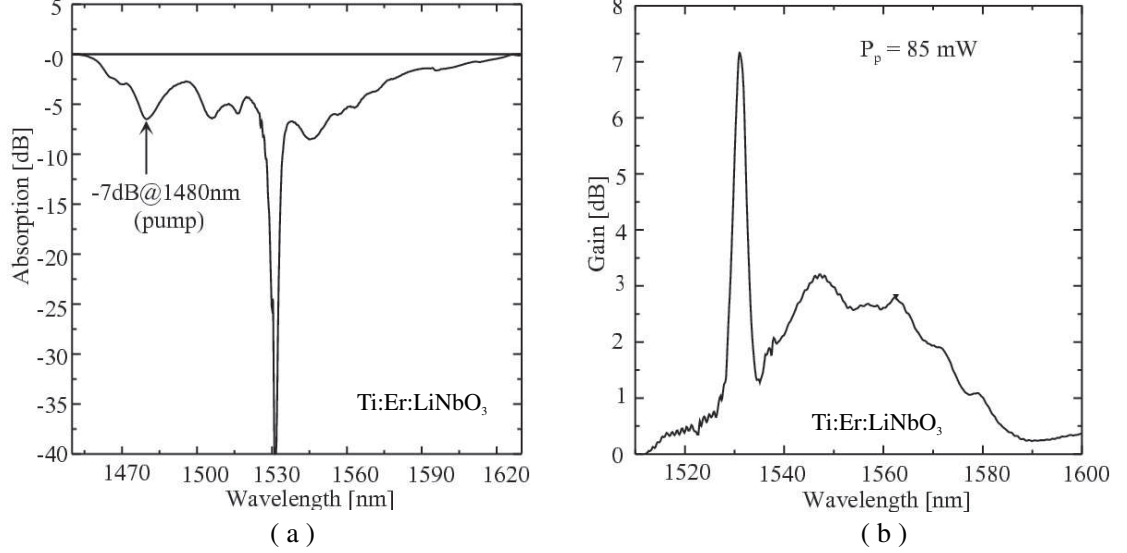


Fig. 3.9: (a) Absorption spectrum of a Ti:Er:LiNbO₃ waveguide and (b) gain spectrum for 85 mW coupled pump power ($\lambda_p = 1480 \text{ nm}$); waveguide length: 5 cm, pump: TE, signal: TE.

3.3.3 Amplified Spontaneous Emission (ASE)

ASE of an EDFA is well-known and usually used as a broadband (incoherent) light source ($1.53 \mu\text{m} < \lambda < 1.64 \mu\text{m}$). Similar to an EDFA, ASE is possible in Ti:Er:LiNbO₃ or in Ti:Fe:Er:LiNbO₃ waveguides if sufficient pump power is provided. Therefore, measuring the ASE spectra we can also perform a qualitative characterization of Er-doped waveguides.

The measured ASE spectrum for TE polarization is shown in Fig. 3.10 along with the schematic experimental setup. ASE spectra were obtained from a 5 cm long Er-doped waveguide (sample: Pb107xz), which was codoped with Fe in a 2 cm long section. It is evident that the ASE spectrum of an Er-doped waveguide with a Fe-codoped section has a similar shape as the gain spectrum obtained from a waveguide only Er-doped (see Fig. 3.9b). This also indicates that Fe-doping does not influence the Er-emission spectrum and the optical gain. In the next chapter we will see that the photorefractive grating fabricated in the Fe-doped section could also be characterized

by measuring the ASE spectrum of the waveguide in transmission through the grating. When the pump light ($\lambda_p = 1480$ nm) is launched to the waveguide amplifiers (Ti:Er:LiNbO₃ or Ti:Fe:Er:LiNbO₃), green fluorescence ($\lambda \sim 550$ nm) becomes visible along the waveguide surface. Very weak red fluorescence ($\lambda \sim 660$ nm) also becomes visible with higher pump power levels.

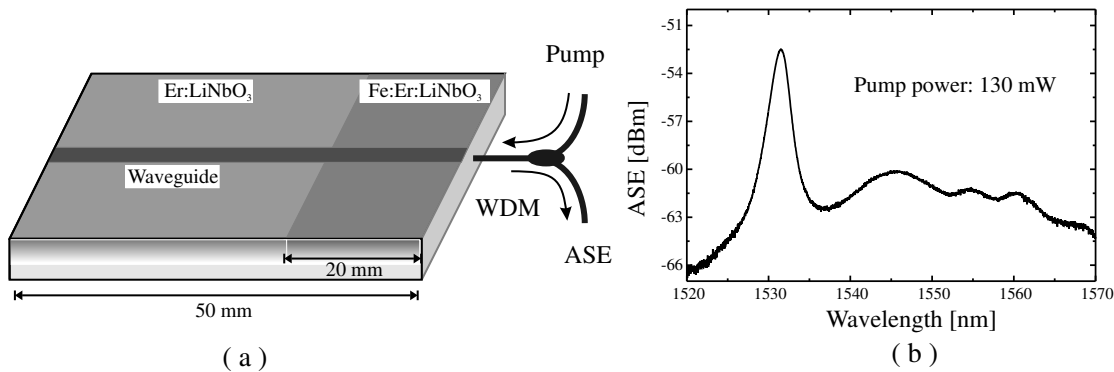


Fig. 3.10: (a) Experimental setup for the ASE measurement and (b) ASE spectrum for 130 mW coupled pump power; pump and ASE are TE-pol.

3.4 Conclusions

Fabrication and characterization of single-mode (at $\lambda \sim 1.55$ μm), laser-active and/or photorefractive, Ti-indiffused LiNbO₃ waveguides have been described in this chapter. Three different types of doped waveguides, i.e. Ti:Er:LiNbO₃ (only laser-active), Ti:Fe:LiNbO₃ (only photorefractive), and Ti:Fe:Er:LiNbO₃ (laser-active and photorefractive) have been investigated. Diffusion doping of Er and Fe, waveguide fabrication by Ti indiffusion, and the necessary annealing treatment have been discussed in details.

Ti:LiNbO₃ and Ti:Fe:LiNbO₃ waveguides have been characterized in terms of waveguide loss and mode-size, whereas, Ti:Er:LiNbO₃ and Ti:Fe:Er:LiNbO₃ waveguides are also characterized by the measurement of optical absorption and gain, and finally by ASE. The results prove that the waveguides are good enough for the development of integrated optical DBR- and DFB-lasers only if a photorefractive Bragg gratings can be realized in the Fe-doped waveguide sections. The next chapter is dedicated for the fabrication and characterization of the thermally fixed photorefractive gratings.

Chapter 4

Photorefractive Gratings: Fabrication and Characterization

4.1 Introduction

Fabrication and characterization of thermally fixed photorefractive Bragg gratings ($\lambda_B \sim 1.55 \mu\text{m}$) in Fe-doped LiNbO_3 waveguides are discussed in this chapter. In fact, the successful development of our different types of integrated optical DBR and DFB lasers using Er-doped LiNbO_3 waveguides has been possible only after the realization of thermally fixed photorefractive Bragg gratings. For the development of DBR lasers, gratings have been fabricated in the passive Ti:Fe:LiNbO_3 section(s), whereas for DFB lasers they have been fabricated in the laser-active Ti:Fe:Er:LiNbO_3 waveguide.

Thermally fixed photorefractive Bragg gratings were already fabricated holographically in the past (but only in Ti:Fe:LiNbO_3 waveguides) [20, 43]. The properties of these Bragg gratings were also found to be very attractive ($L = 1 \text{ cm}$, $R > 50\%$, $\text{FWHM} \sim 100 \text{ pm}$). However, because of the lack of parameter optimizations, it took a long holographic exposure time ($> 2 \text{ h}$) for grating fabrication. Therefore, a very higher degree of stability is needed for the experimental setup as well as the for the surrounding atmosphere.

Under the scope of this work a compact holographic setup has been developed and the fabrication parameters have been optimized. As a result it needs only a few minutes of holographic exposure for fabrication of an efficient grating. E.g, a 18-mm-long grating ($R > 95\%$, $\text{FWHM} \sim 60 \text{ pm}$) could be fabricated with a holographic exposure of only 5 min!

4.2 Fabrication

Thermally fixed photorefractive Bragg gratings were fabricated in Fe-doped waveguide sections with the grating vectors parallel to the waveguide axis (Z-axis). The fabrication technology has been developed on the basis of the theoretical discussion given in Chapter 2. The compact experimental setup (see Fig. 4.1) has allowed to perform the grating definition (holographically), online characterization, thermal fixing, and development of the fixed grating in step by step.

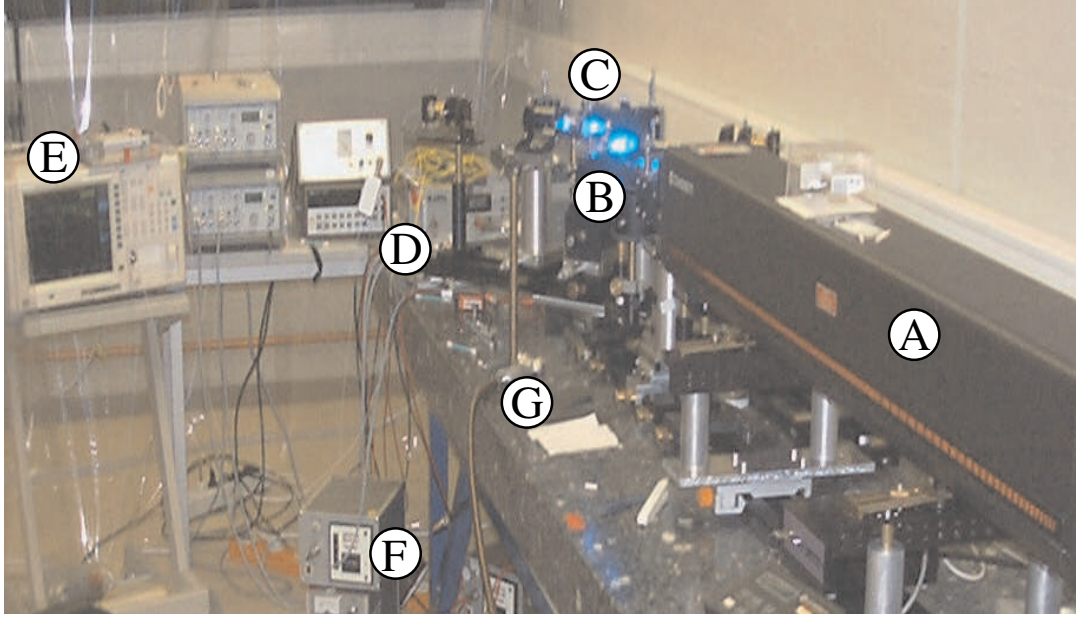


Fig. 4.1: The experimental setup developed for grating fabrication. A: argon laser ($\lambda = 488 \text{ nm}$, $P = 1 \text{ W}$), B: optics for wavefront shaping, C: sample held by a goniometric stage, D: EDFA, E: optical spectrum analyzer, F: temperature controller of the sample, G: cooling air gun.

4.2.1 Grating Definition

The gratings were fabricated by the illumination of an interference pattern of light along the waveguide axis. Therefore, the reflections from the back surface of the sample could cause of a reduction of the contrast of the interference pattern. We prevented these reflections by depositing an antireflection (AR) coating (alternating layers of SiO_2 and TiO_2) on the back surface of the sample. In addition, an AR coating ($\lambda \sim 1.55 \mu\text{m}$ for 90° incidence angle) at the end-faces of the waveguides also helped to characterize the gratings more precisely by mode transmission and reflection experiments.

An argon laser ($\lambda = 488 \text{ nm}$, $P = 1 \text{ W}$) has been used in the holographic setup for grating definition (see Fig. 4.1). There are three main sections of the whole setup: (i) optics for proper wavefront shaping, (ii) the holographic setup, and (iii) the equipment for online grating characterization.

Wavefront Shaping:

The interference fringe pattern required for grating fabrication has been generated

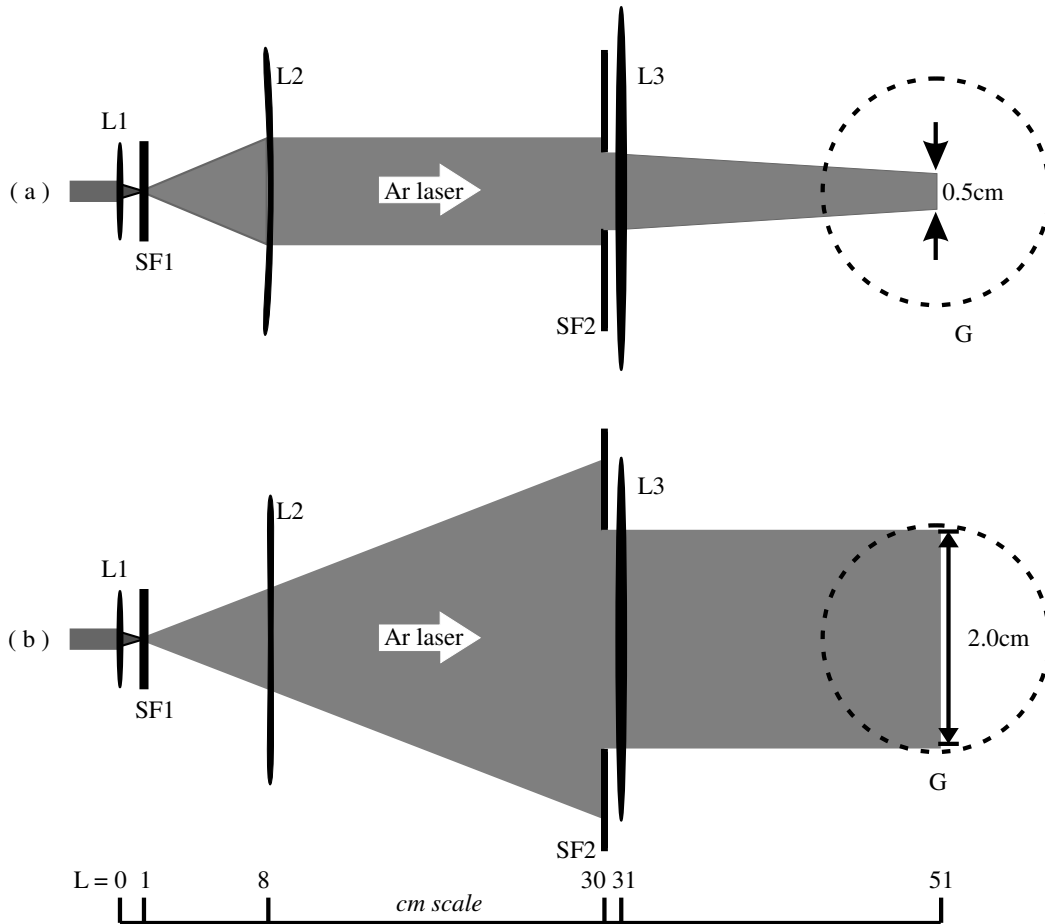


Fig. 4.2: Schematic structure for $20 \text{ mm} \times 5 \text{ mm}$ wavefront shaping from an argon laser beam of $1/e$ diameter $\sim 1.3 \text{ mm}$: (a) along vertical direction and (b) along horizontal direction. L1: focussing lens ($f_1 = 1 \text{ cm}$), L2: collimating cylindrical lens ($f_2 = 8 \text{ cm}$), L3: collimating spherical lens ($f_3 = 30 \text{ cm}$), SF1: pinhole spatial filter ($\phi = 10 \mu\text{m}$), SF2: spatial filter ($20 \text{ mm} \times 5 \text{ mm}$), G: position of the goniometric stage on which the Lloyd setup is to be placed.

by folding the laser wavefront in a Lloyd-type interferometer. Therefore, generation of a good quality wavefront is crucial for a good fringe pattern. Uniformity and high degree of contrast of the interference pattern along the waveguide surface has to be

ensured. Moreover, the intensity itself should be as high as possible to reduce the exposure time for grating fabrication. The shorter the exposure time the better is the stability of the interference pattern with respect to the environmental perturbations (vibration, convection, etc.).

Keeping all the above in mind a cylindrical wavefront of the argon laser beam has been generated as shown in Fig. 4.2. The fundamental TEM_{00} mode of the argon laser ($1/e^2$ beam-waist ~ 1.3 mm) polarized along the vertical direction was focussed by a lens (L1) of focal length $f_1 = 1$ cm. The focussed beam is spatially filtered by a pinhole (SF1) of diameter $10 \mu\text{m}$. The beam is then collimated along the vertical direction by a cylindrical lens, L2 ($f_2 = 8$ cm). Afterwards, the beam passes through a rectangular aperture (SF2) of size $20 \text{ mm} \times 10 \text{ mm}$. Behind the exit of SF2, it is collimated along the horizontal direction and focussed along the vertical direction by the lens L3 ($f_3 = 30$ cm). Finally, passing another 20 cm from L3, it reaches the center of the Lloyd setup placed on a goniometric stage (G). In this way, it was possible to achieve a rectangular beam (dimension: $\sim 20 \text{ mm} \times 5 \text{ mm}$, average light intensity: $\sim 500 \text{ mW/cm}^2$) in the vertical plane at the center of the Lloyd setup.

Holographic Setup:

A schematic diagram of the Lloyd setup along with a zoomed photograph of the holo-

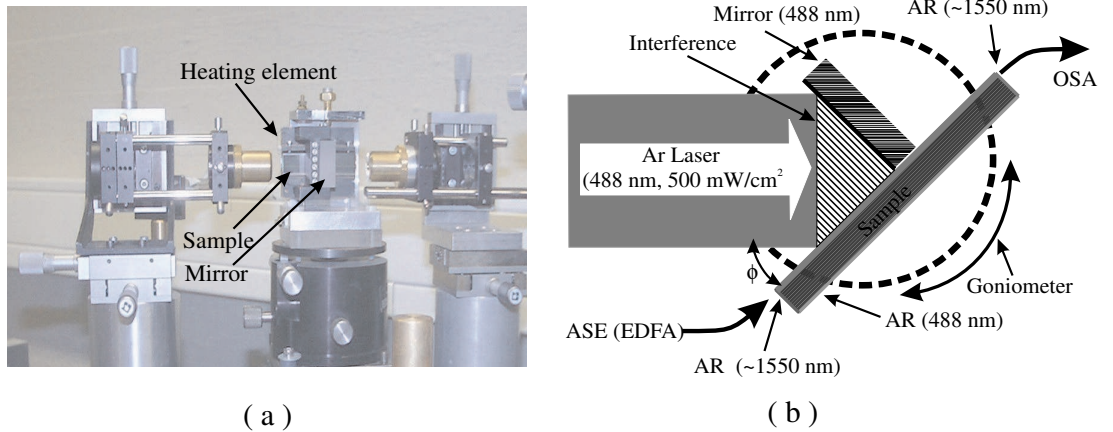


Fig. 4.3: Lloyd setup used for photorefractive grating fabrication: (a) photograph of the Lloyd-type arrangement taken from the experimental setup and (b) schematic diagram showing interference fringe generation along the waveguide. AR: antireflection coatings, OSA: optical spectrum analyzer, ASE (EDFA): amplified spontaneous emission from an erbium doped fiber amplifier, ϕ : glancing angle of wavefront on the surface of the sample.

graphic setup is shown in Fig. 4.3. In a special copper holder (designed by Dr. H. Suche, Dept. Applied Physics, University of Paderborn, Germany), a square mirror ($2.5 \text{ cm} \times 2.5 \text{ cm}$, Thickness: 1.0 cm) and the sample (Length: 5-9 cm, Width: 1.2

cm, Thickness: 1 mm) are placed in such a way that the waveguides are perpendicular to the reflecting surface of the mirror. The mirror has an effective reflecting area of $2.4 \text{ cm} \times 2.4 \text{ cm}$ with surface flatness $\sim \lambda/20$ and reflectivity 99% at $\lambda = 488 \text{ nm}$. Nearly half of the incoming wavefront is reflected from the mirror and superimposed on the other half to produce the periodic interference pattern along the waveguide axis. The required periodicity of the interference pattern is achieved by adjusting the glancing angle ϕ . For the adjustments of this angle we use a goniometric stage (see also the *Setup Calibration and Thermal Fixing* part of this section).

The sample could be uniformly heated up to $250 \text{ }^\circ\text{C}$ with an electronic control (proportional integral derivative) loop arrangement, although for thermal fixing process it needs only $180 \text{ }^\circ\text{C}$. A heating wire made of Ni-Cr passing through a number of ceramic tubes has been used as the heating element. The ceramic tubes are carefully inserted inside the copper holder so that the sample could be heated uniformly. To achieve a good thermal conduction from copper holder to sample the holder was black-painted (camera-black). This camera-black also helps to avoid stray light during the holographic exposures. The holder is mounted on the goniometric stage by means of three needle-edged metallic supports for thermal isolation.

Online Characterization of the Electronic Grating:

At room temperatures, when the holographic exposure starts, the refractive index grating starts forming. The growth of gratings can be monitored online by measuring the transmission at the output of the waveguides after launching incoherent broadband light into the input. In this case, ASE from an EDFA is used. The ASE source has about 35 mW power distributed in the emission band of $1.52 \text{ } \mu\text{m} < \lambda < 1.62 \text{ } \mu\text{m}$. An optical spectrum analyzer (OSA) of spectral resolution $\sim 10 \text{ pm}$ is used for the transmission measurements.

E.g. the growth and decay dynamics of two photorefractive gratings of 15 mm length, each written in Ti:Fe:LiNbO₃ and Ti:Fe:Er:LiNbO₃ waveguides, respectively, fabricated on the same substrate (Pb107xz) separated by $\sim 1.5 \text{ mm}$, are shown in Fig. 4.4a. The reflectivity shown in Fig. 4.4a is deduced from the transmission characteristics shown in Fig. 4.4b. The efficiencies of both the gratings saturate in less than 5 min of holographic exposure.

When the holographic exposure is switched off, initially, both gratings decay very fast for few minutes. During this stage, the grating in Ti:Fe:LiNbO₃ decays faster than the grating in Ti:Fe:Er:LiNbO₃. However, after a few minutes, both gratings decay with decay constants of almost equal magnitudes.

In transmission characteristics, the polarization dependent Bragg responses and their slightly different efficiencies in both types of waveguides are observed. Although, in X-cut and Z-propagating LiNbO₃ waveguides, both TM- and TE-modes are α -polarized

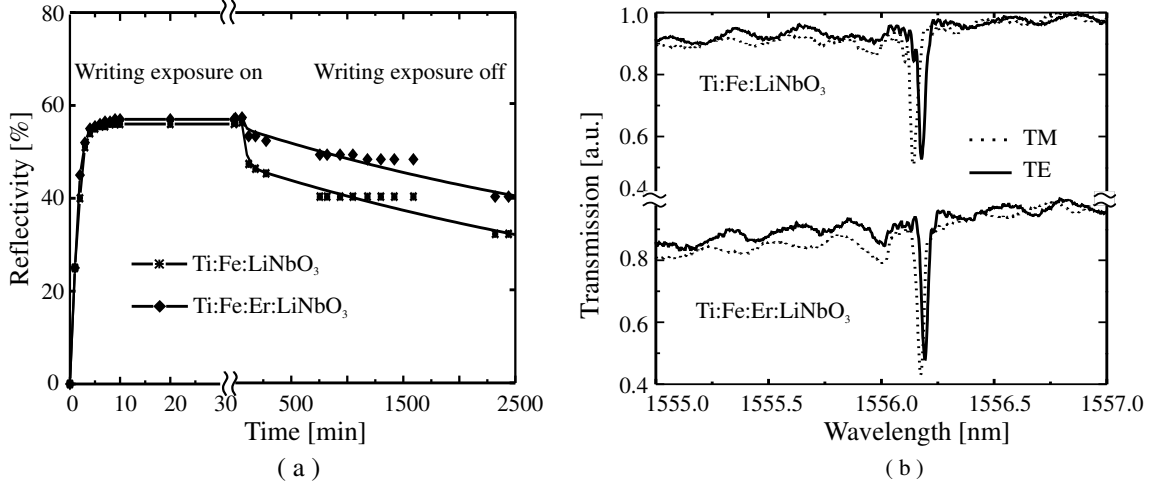


Fig. 4.4: Online characterization of the photorefractive gratings written in Ti:Fe:LiNbO₃ and Ti:Fe:Er:LiNbO₃ at room temperature (Pb107xz): (a) growth and decay dynamics of the grating responses for the TE-mode, (b) grating transmission for TE- and TM-polarized light, respectively.

($\vec{E}, \vec{B} \perp c$ -axis and $\vec{k} \parallel c$ -axis), the different boundary conditions of the guiding layer result in slightly different Bragg responses. However, the polarization independent linewidth of the Bragg response is measured to be ~ 60 pm, the same for both waveguides.

The measured results confirms that both the Ti:Fe:LiNbO₃ and Ti:Fe:Er:LiNbO₃ waveguides have almost equal photorefractive sensitivity. That means, incorporation of erbium does not change significantly the photorefractive sensitivity of the crystal.

Setup Calibration:

The Bragg wavelength λ_B is defined as a function of glancing angle, ϕ_B :

$$\lambda_B = \frac{n_{eff}(\lambda_B) \cdot \lambda_w}{\cos \phi_B} \quad (4.1)$$

Therefore, one can calculate the value of λ_B at a specific glancing angle ϕ_B only, if the effective refractive index, n_{eff} , of the guided mode is known. But the calculated Bragg wavelength using $n_{eff} = 2.21$, estimated by standard methods (effective index or variational method) using the Ti-indiffusion parameters, slightly differs with our experimental results. This is because the refractive index change due to Fe (Er-incorporation does not change the refractive index) incorporation could not be included in the calculations because of the lack of experimental results.

However, we obtained the $(\phi_B - \lambda_B)$ calibration curve as shown in Fig. 4.5 for the setup. The shift of $\Delta\lambda_B \approx 5$ nm of the Bragg response from the theoretical results is

due to the error in effective refractive index and the mechanical errors in the Lloyd setup configuration.

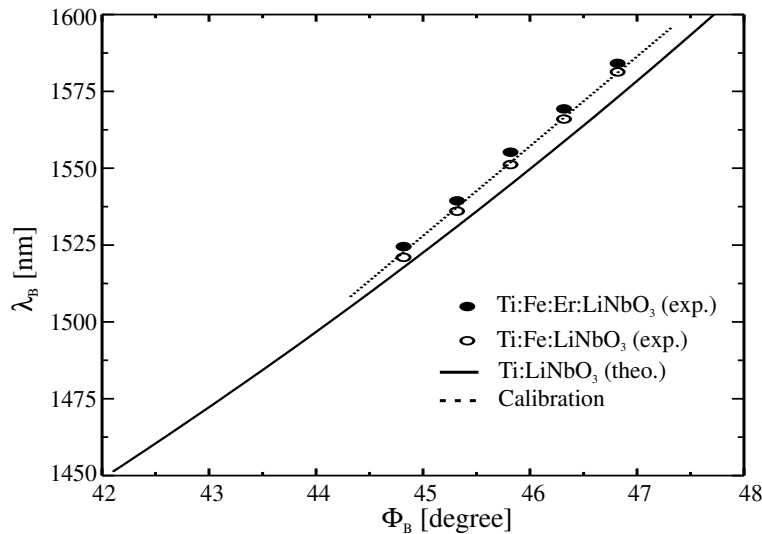


Fig. 4.5: The Bragg wavelength (λ_B) as a function of glancing angle (ϕ_B) for waveguides with different dopants.

4.2.2 Thermal Fixing and Development of Ionic Gratings

The refractive index gratings written at room temperatures are volatile; they can not be used for permanent applications. Therefore, the ionic (H^+) gratings have been fabricated using the thermal fixing method. For thermal fixing, the holographic exposure is done at an elevated sample temperature (150-200 °C), so that thermally activated protons can move to compensate the electronic grating. We found the best results when the temperature of the sample holder was kept at 180 °C.

Two types of sample holders were built up: the first type can heat the whole sample whereas the second type can heat the specific sample area alone where the grating is to be fabricated. The steady state surface temperature profile (measured by touching the sample with a flat-surface platinum resistance thermometer) along the length of the sample for both cases are shown in Fig. 4.6. Using the second type (see Fig. 4.6b), we were able to fabricate two different fixed gratings at two different positions in the same waveguide to develop the single-frequency laser to be discussed in the next chapter.

In general, ≤ 10 min of holographic exposure is used for thermal fixing. When the exposure stops, the sample is cooled down very fast to room temperature to freeze the proton distribution. Cooling the sample takes less than 4 min using a fan cooler. During thermal fixing, it is not possible to monitor online the grating response because the

electronic gratings formed by the holographic exposure are completely compensated by the H^+ gratings. For fixing a grating at a specific Bragg wavelength one has to correct the room temperature calibration curve ($\phi_B - \lambda_B$) shown in Fig. 4.5 for thermal fixing temperatures. For a defined glancing angle ϕ_B , a shift of $\Delta\lambda_B \approx -0.5$ nm is observed in Bragg wavelength λ_B , compared to the room temperature environment.

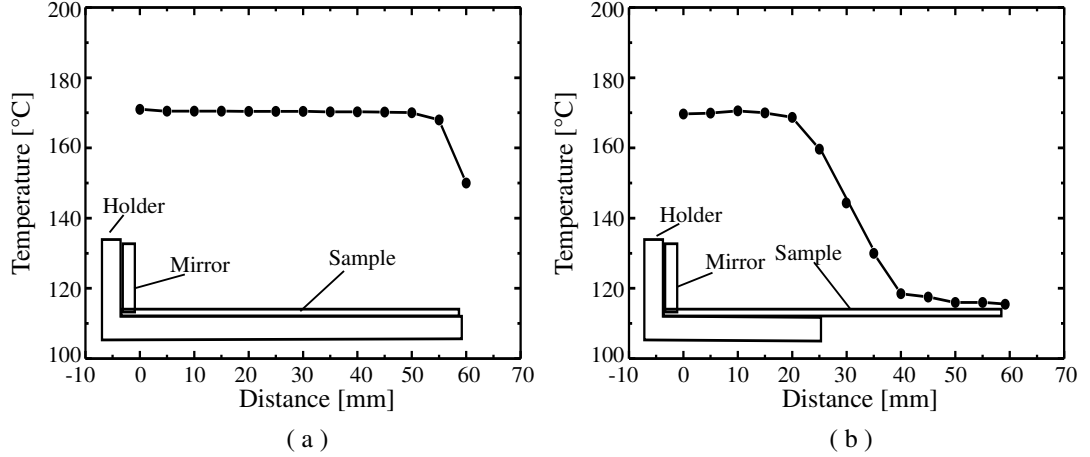


Fig. 4.6: Surface temperature profile along the sample length when the sample holder kept at 180 °C temperature: (a) heating the whole sample (b) heating limited to a defined section of the sample.

At the end of the thermal fixing procedure, the index grating is developed by a homogeneous illumination with blue light either using the expanded beam of an argon laser ($\lambda = 488$ nm) or an array of GaN LEDs ($\lambda_{peak} = 470$ nm). E.g., the developing of a fixed grating of a length of 13 mm in a Ti:Fe:LiNbO₃ waveguide (Pb66xz), fabricated by a holographic exposure of 10 min is given in Fig. 4.7a. In this case, it was developed by the illumination from LEDs ($I \approx 25$ mW/cm² at the sample surface). In Fig. 4.7b, the corresponding grating transmission characteristics for TM-polarization is shown; it has been measured after the development exposure of 1 h. The reflectivity at the Bragg wavelength $\lambda_B \approx 1552.5$ nm is 70%.

It is clear from the developing dynamics that the developing speed of the fixed grating decays exponentially with an intensity dependent time constant. However, use of very high intensity light for fast development should be avoided because unwanted uniform refractive index change throughout the illuminated area may appear as an “optical damage” of the guided mode.

4.3 Properties of Fixed Gratings

Some important properties of thermally fixed photorefractive gratings studied experimentally are discussed in this section. As it was possible to fabricate fixed gratings in

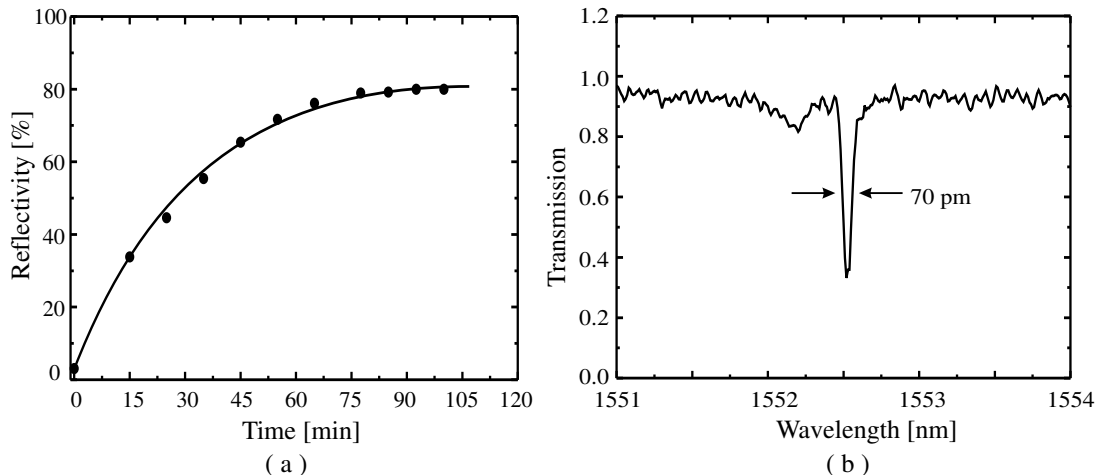


Fig. 4.7: Thermally fixed photorefractive grating in a Ti:Fe:LiNbO₃ waveguide (sample: Pb66xz): (a) development of peak reflectivity vs. time by homogeneous illumination with an array of GaN LEDs and (b) transmission characteristics for the TM-polarized light after the development exposure of 1 h.

both Ti:Fe:LiNbO₃ and Ti:Fe:Er:LiNbO₃ waveguides, it is interesting to see what are the differences of their properties. In general, the gratings in both types of waveguides show almost similar photorefractive sensitivity. But, in presence of green fluorescence (when Er³⁺ ions are excited by pump laser light at $\lambda_p = 1.48 \mu\text{m}$) in Ti:Fe:Er:LiNbO₃ waveguides, the grating dynamics is influenced significantly.

Dark Decay:

After the fabrication a thermally fixed photorefractive grating needs a homogeneous illumination of blue light to exhibit the fixed ionic (H⁺) grating. As mentioned earlier while thermal fixing process, the ionic grating is formed as a result to compensate the electronic grating generated by the holographic exposure. During development exposure, the electrons are redistributed and subsequently the H⁺ grating builds up. However, withdrawal of uniform developing exposure can reverse electron motion due to the dark conductivity and starts compensating the so called fixed H⁺ grating. This compensation causes a decay in reflectivity/efficiency with time as shown in Fig. 4.8. The similar behavior of the decay of the grating in both types of waveguide confirms again that erbium has no influence on the photorefractive sensitivity.

Refreshing:

Due to the dark conductivity of electrons, a fixed ionic grating decays with time as we have seen in our previous experiments. However, the ionic grating can be refreshed with uniform illumination of light of appropriate wavelength and intensity. By controlling this refreshing light intensity level one can achieve any desired reflectivity/efficiency (below the saturation efficiency) of a fixed grating. This argument is clearly demonstrated by an experimentally observed dynamical behavior of a ther-

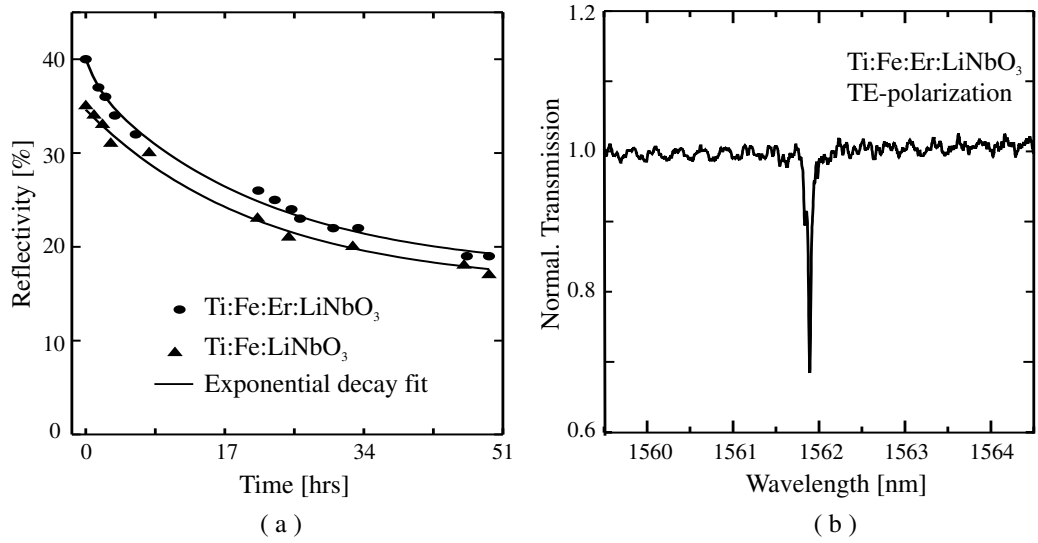


Fig. 4.8: (a) Electronic compensation of two thermally fixed ionic gratings of 10 mm length each in the dark, in Ti:Fe:LiNbO₃ and Ti:Fe:Er:LiNbO₃ waveguides, respectively, fabricated on the same substrate (Pb107xz) with the same holographic exposure of 4 min. (b) The transmission characteristics of one of the fixed gratings (just after developing) for TE-polarization.

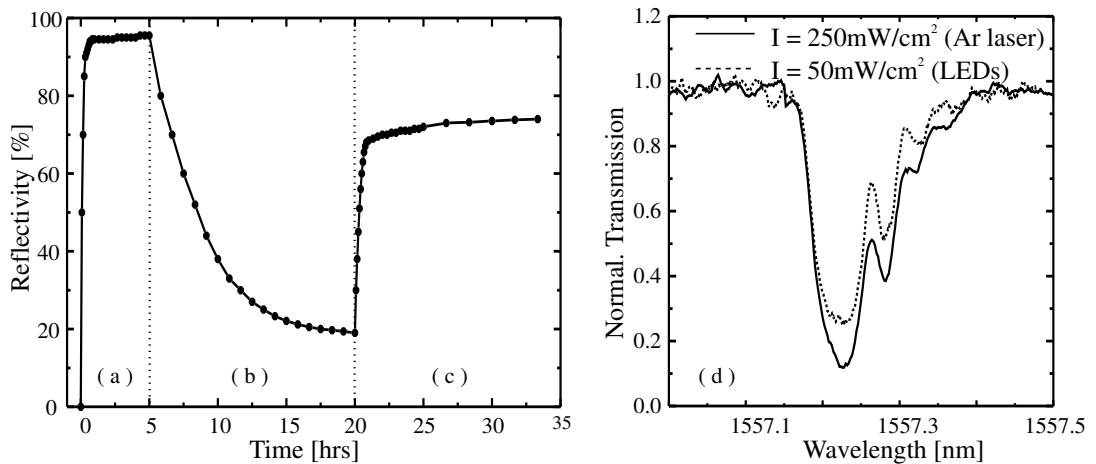


Fig. 4.9: Dynamical behavior of a thermally fixed photorefractive grating fabricated by a holographic exposure of 5 min in a Ti:Fe:Er:LiNbO₃ waveguide (Pb150xz): (a) development by a uniform Ar laser beam ($I = 250 \text{ mW/cm}^2$, $\lambda = 488 \text{ nm}$), (b) the fixed grating reflectivity decays in absence of developing exposure, (c) refreshment by an array of 8 GaN LEDs ($I \approx 50 \text{ mW/cm}^2$, $\lambda_{peak} = 470 \text{ nm}$), and (d) the grating transmission characteristics of the TE-mode for both types of illumination.

mally fixed photorefractive grating fabricated in a Ti:Fe:Er:LiNbO₃ waveguide (see Fig. 4.9).

Amplified Grating Response in Ti:Fe:Er:LiNbO₃:

The presence of Er³⁺ in a Ti:Fe:Er:LiNbO₃ waveguide can provide an amplified grating response in the wavelength region, $1.53 \mu\text{m} < \lambda < 1.64 \mu\text{m}$, when it is excited by diode laser light of $1.48 \mu\text{m}$ (or $0.98 \mu\text{m}$) wavelength (see also Fig. 3.10). The internal ASE itself is used to characterize the grating response both in transmission and reflection.

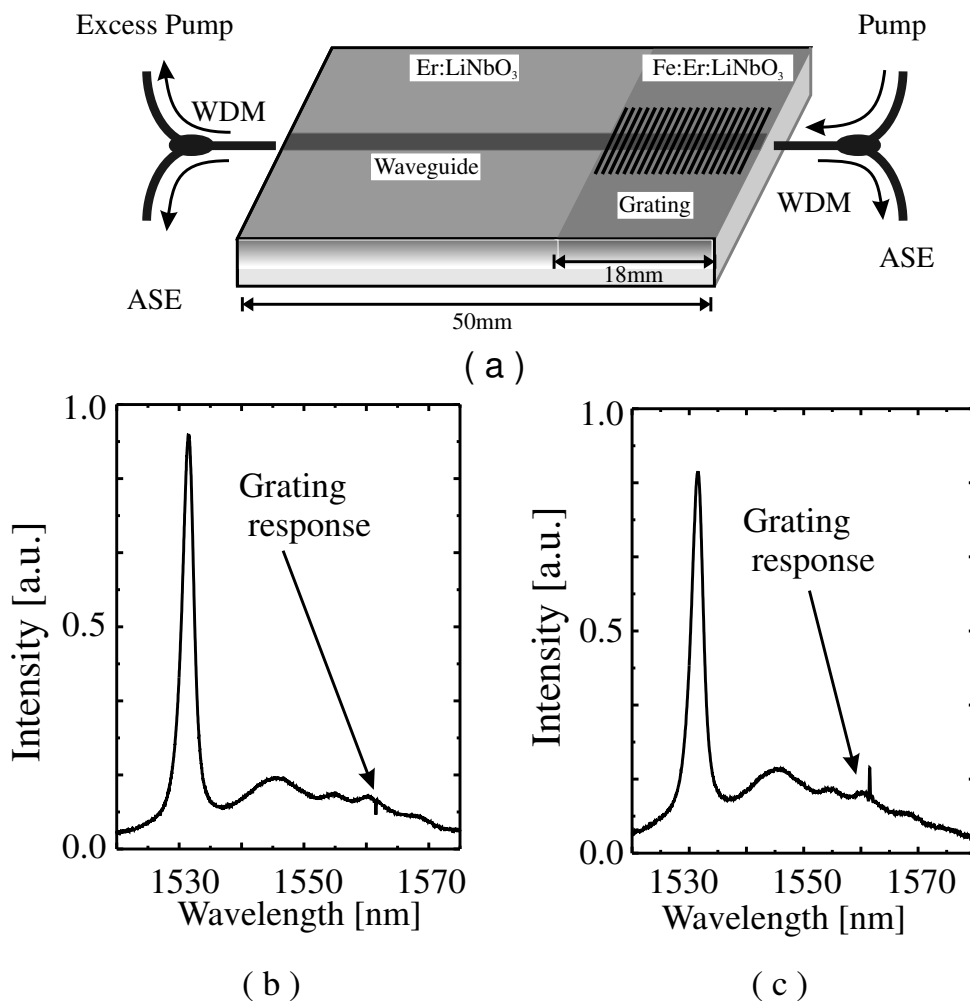


Fig. 4.10: Amplified grating response in a Ti:Fe:Er:LiNbO₃ waveguide (sample: Pb107xz) for TE-polarized light measured with OSA resolution of 0.1 nm: (a) schematic structure of the experimental setup, (b) grating response along with ASE (measured at the right output) and (c) grating transmission response along with ASE (measured at the left output). WDM: wavelength division (de-)multiplex, Pump: 100 mW power at $1.48 \mu\text{m}$ wavelength.

The experimental setup shown in Fig. 4.10a was used for studying a fixed grating using internal ASE. In fact, for our study, a 18-mm-long grating ($\lambda_B \sim 1562$ nm and $R > 80$ %) was thermally fixed in a Ti:Fe:Er:LiNbO₃ waveguide, which is combined with another 32-mm-long Ti:Er:LiNbO₃ waveguide section. The pump light ($\lambda_p = 1480$ nm, $P = 100$ mW) was launched to the waveguide from the grating side and the ASE spectra from both sides were separated by two wavelength division (de-)multiplexers (WDMs). As expected, the ASE spectrum travelling to the right, reveals approximately the transmission characteristics of the grating (Fig. 4.10b). On the other hand, from the amplifier side, the ASE spectrum travelling to the left reveals the reflected part of the right-travelling ASE (Fig. 4.10c).

Grating Stabilization by Green Fluorescence:

Along with the ASE, there is a green up-conversion fluorescence ($\lambda = 550$ nm, (${}^4S_{3/2} \rightarrow {}^4I_{15/2}$)) in Ti:Fe:Er:LiNbO₃ waveguides in presence of pump light at $\lambda_p = 1.48$ μm (or 0.98 μm). Our interest was to utilize this green fluorescence for the compensation of the decay of a fixed grating as an alternative to the refreshing exposure with a separate source. The experimental observation is very promising as shown in Fig. 4.11.

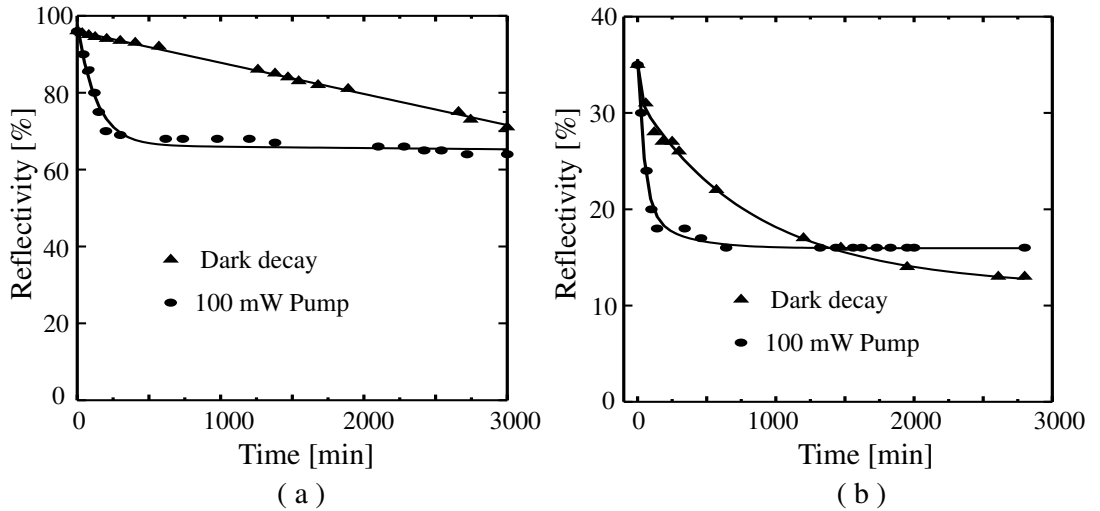


Fig. 4.11: Stabilization of the reflectivity of thermally fixed photorefractive gratings fabricated in a Ti:Fe:Er:LiNbO₃ waveguide (Pb107xz) by pumping with 1.48 μm light (100 mW); reflection versus time: (a) initial grating reflectivity $\sim 95\%$ and (b) initial grating reflectivity $\sim 35\%$. The results are taken for TE-polarized light.

For the study we used the same experimental arrangement as shown in Fig. 4.10a. The gratings of initial reflectivities of $\sim 95\%$ and $\sim 35\%$, respectively, are stabilizing at reflectivities of $\sim 70\%$ and $\sim 16\%$, respectively, when they are pumped with 100

mW. The cause of the initial rapid decay is not known yet. However, one can speculate with the erbium fluorescence at $\lambda \sim 388$ nm (${}^4G_{11/2} \rightarrow {}^4I_{15/2}$) which can generate holes in the valence band of LiNbO_3 (see also Chapter 2, Fig. 2.1b and Chapter 3, Fig. 3.7) and with the fluorescence at $\lambda \sim 660$ nm (${}^4F_{9/2} \rightarrow {}^4I_{15/2}$) which can produce small polarons (see also Chapter 2, Fig. 2.1c and Chapter 3, Fig. 3.7).

In other experiments, we have also observed that a fixed grating response could decay to almost zero efficiency, if the pump laser is switched on and off, respectively, for a few times. Afterwards, it needs another refreshing exposure by external blue illumination to refresh the H^+ grating to its initial strength. Although, the presence of green fluorescence can reduce the grating decay significantly, the refreshment of a decayed grating by the up-conversion fluorescence is not that much promising as hoped. Only up to 10% of the grating efficiency could be refreshed by the green fluorescence.

Temperature Tuning:

Changing the temperature of the sample produces two main effects influencing the

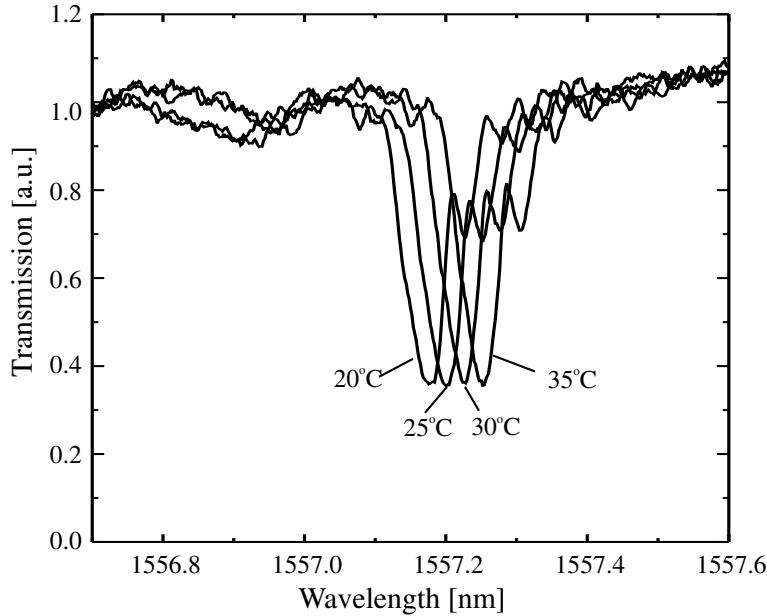


Fig. 4.12: Temperature tuning of a thermally fixed grating in a Ti:Fe:Er:LiNbO_3 waveguide (sample: Pb150xz). The observed tuning slope is ≈ 5 pm/ $^\circ\text{C}$.

Bragg grating filter. The effective refractive index, n_{eff} , increases by increasing the temperature according to the Sellmeier's equation [6] and the grating period, Λ , increases as a consequence of the thermal expansion. So, the change of the Bragg response is expressed as [78]:

$$\frac{\Delta\lambda_B}{\lambda_B} = \frac{\Delta n_{eff}}{n_{eff}} + \frac{\Delta\Lambda}{\Lambda} \quad (4.2)$$

where

$$\frac{\Delta\lambda}{\lambda} = \alpha_{33}\Delta T \quad \text{and} \quad \frac{\Delta n_{eff}}{n_{eff}} = \beta_0\Delta T \quad (4.3)$$

Here, $\alpha_{33} \approx 5.6 \times 10^{-6}\text{K}^{-1}$ and $\beta_0 \approx 5.9 \times 10^{-6}\text{K}^{-1}$ are the appropriate coefficients for linear thermal expansion along the c -axis and ordinary refractive index change, respectively. The corresponding theoretical temperature tuning $\Delta\lambda_B/\Delta T \approx 6 \text{ pmK}^{-1}$. The temperature tuning slope observed in our experiment is $\approx 5 \text{ pmK}^{-1}$ (see Fig. 4.12) which is close to the theoretical predictions.

Electrooptic Tuning:

The Bragg response can also be tuned by exploiting the electrooptic effect of LiNbO_3 .

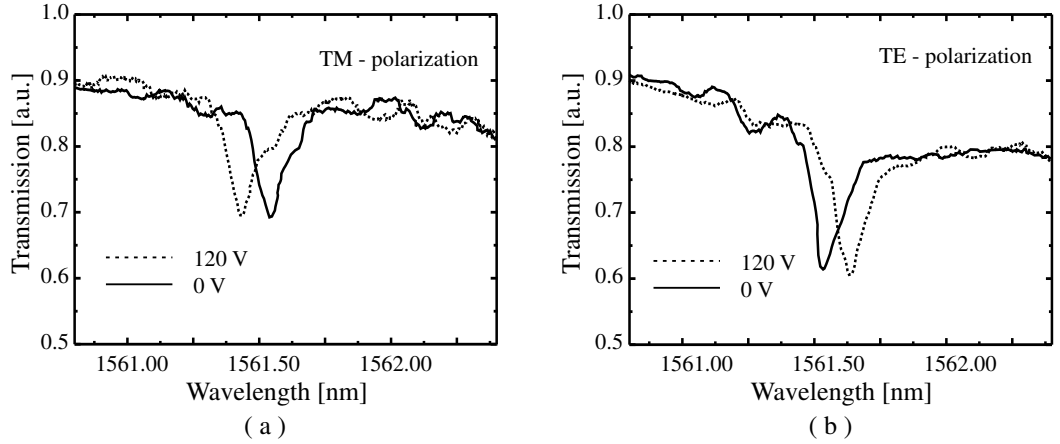


Fig. 4.13: Electrooptic tuning of a thermally fixed grating in a Ti:Fe:Er:LiNbO_3 waveguide (sample: Pb145xz) for both TM- (a) and TE-polarizations (b). The observed tuning slope is $\approx 0.75 \text{ pm/V}$. The transmission spectrum was observed with 50 pm resolution of the OSA.

When an external electric field (\vec{E}) is applied across the grating by fabricating two electrodes on both sides of the waveguide, there is a change of the index of refraction given by:

$$\Delta n_{eff} = -\frac{1}{2}n_{eff}^3 r E \Gamma \quad (4.4)$$

where the electrooptic coefficient $r = r_{22}$ for TE-polarization and $r = -r_{22}$ for TM-polarization, Γ is the overlap integral of guided optical mode and applied electric field distribution.

To observe the electrooptic tuning of a grating, two parallel gold electrodes separated by $15 \mu\text{m}$ were fabricated on both sides of the Ti:Fe:Er:LiNbO_3 waveguide (Pb145xz). Afterwards, a thermally fixed grating ($L = 15 \text{ mm}$, $R = 30\%$, $\text{FWHM} = 50 \text{ pm}$) was fabricated with a holographic exposure of 5 min. The Bragg responses of the grating for both TM- and TE-polarizations were measured for 120 V and 0

V, applied to the electrodes (see Fig. 4.13). As expected from the equation (4.4), the Bragg wavelengths for TM- and TE-polarizations are tuned in opposite directions and the average tuning slope is found to be about ± 0.75 pm/V. Using this opposite tuning slope, a polarization independent grating response could also be obtained.

4.4 Conclusions

Fabrication and characterization of thermally fixed photorefractive Bragg gratings in both passive Ti:Fe:LiNbO₃ and laser-active Ti:Fe:Er:LiNbO₃ waveguides have been performed. A compact holographic setup (Lloyd configuration) was developed for grating fabrication. With this setup, up to 18-mm-long gratings ($R > 95\%$ and FWHM < 60 pm) have been fabricated with a very short holographic exposure (≤ 10 min). Although the results are quite reproducible, sometimes the air turbulence due to thermal convection induces some problems during the thermal fixing process. It could be avoided completely if the whole setup is placed in a vacuum chamber. Experimental results of the grating development, decay in the dark, refreshing, stabilization of the grating response, thermal tuning and electrooptic tuning are presented. All these properties have been determined by measuring the transmission characteristics.

To use a phase mask is an alternative method of writing photorefractive Bragg gratings, which requires no sensitive holographic set up. The Bragg response is defined by the periodicity of the phase mask. Therefore, to write gratings of different periods several phase masks are needed, which is not only inconvenient but also expensive. For that reason we used the holographic method only.

Chapter 5

Lasers with Photorefractive Gratings

5.1 Introduction

The excellent properties of the photorefractive gratings and their integrability with gain sections as discussed in the previous chapter stimulated our development of integrated, Er-doped, optically pumped lasers in LiNbO₃ [17,18]. Besides cw Fabry-Perot lasers of high efficiency ($\sim 40\%$) and output power (~ 60 mW), Q-switched lasers (~ 4 ns long pulses of up to 2 kW peak power with ~ 1 kHz repetition rate) and actively mode-locked lasers (~ 4 ps pulses of 10 GHz repetition rate; ~ 6 mW average power) another variety of attractive narrow-linewidth, fixed frequency and fully integrable lasers can now be developed taking advantage of photorefractive gratings as narrow-band reflectors.

Photorefractive Bragg gratings can favorably replace the surface relief gratings of DBR-lasers developed earlier [19,31]. Moreover, DBR-lasers with two gratings, DFB-lasers and DFB-DBR coupled cavity lasers have been developed. In the following sections these new devices are discussed; device description, operation and typical results are presented.

5.2 Basic Theory of Ti:Er:LiNbO₃ Waveguide Lasers

The general theory of Ti:Er:LiNbO₃ waveguide lasers was already developed [79,80]. The basic structure of these lasers is shown in Fig. 5.1. A Ti-indiffused optical strip waveguide is embedded in (locally) Er-diffusion doped LiNbO₃. Optical gain ($\lambda_s \sim 1.5 \mu\text{m}$) is achieved by the optical excitation of Er³⁺ ions by coupling external radiation (say, $\lambda_p = 1480$ nm) directly into the waveguide (longitudinal pumping). The wavelength dependent feedback elements are the two mirrors R₁ and R₂, respectively, forming in this way a longitudinal resonator.

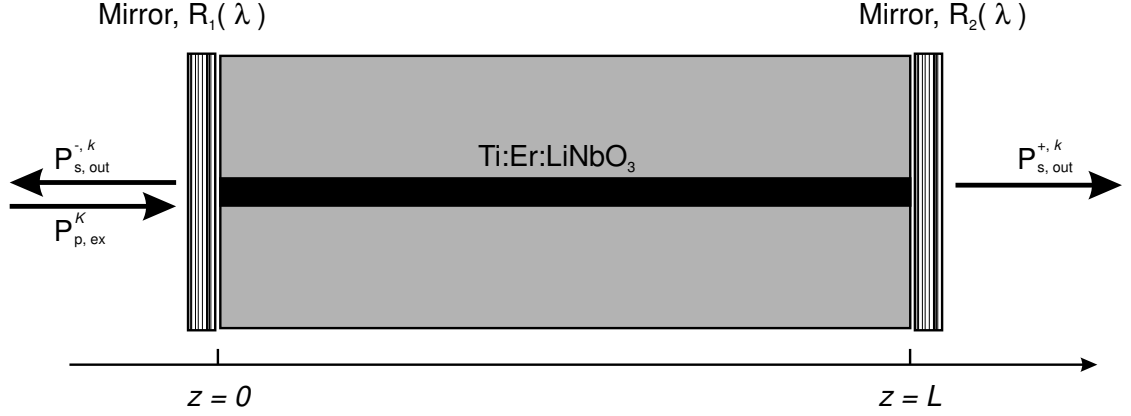


Fig. 5.1: Schematic diagram of an erbium-doped integrated optical waveguide laser with amplifying length of L . $P_{p,ex}^k$: k -polarized ($k = \pi, \sigma$) external pump power, $P_{s,out}^{\pm,k}$: signal output power in forward (+) and backward (-) directions.

We restrict our theoretical discussion to the $1.48 \mu\text{m}$ pump-band as preferred absorption band in LiNbO_3 with negligible excited state absorption, and hence negligible photorefractive damage. Furthermore, monomode waveguides for both pump and signal, both having a good overlap with the erbium diffusion profile - a quasi-two-level-model can be used to model the optical amplification in the wavelength range $\lambda_s \sim 1.5 \mu\text{m}$ [81]. The energy splitting of the $^4I_{15/2}$ ground state (level-1) and the first excited state $^4I_{13/2}$ (level-2) (see Fig. 3.7) due to the Stark-effect is taken into account with the wavelength dependent absorption and emission cross sections, σ_{12} and σ_{21} , respectively. In addition, $A_{21} = 1/\tau$ describes the spontaneous transition from the excited state to the ground state; τ is the fluorescence lifetime. If in the presence of pump and signal light, $N_1(x, y, z, t)$ and $N_2(x, y, z, t)$ are the population densities of Er^{3+} ions of the ground- and excited-state, respectively, they can be deduced from the steady state rate equation:

$$N_1 = \frac{w_{21} + A_{21}}{w_{12} + w_{21} + A_{21}} N_o \quad (5.1)$$

$$N_2 = \frac{w_{12}}{w_{12} + w_{21} + A_{21}} N_o \quad (5.2)$$

Here, the Er^{3+} -concentration $N_o(x, y) = N_1(x, y, z, t) + N_2(x, y, z, t)$ is independent of the coordinate z and time t . The rate of stimulated absorption (emission) is defined by w_{12} (w_{21}):

$$w_{mn} = \sum_{j=p,s} \left(\frac{1}{hc} \sum_{k=\pi,\sigma} \int_0^\infty \lambda_j \sigma_{mn,j}^k i_j^k(x, y, z, \lambda_j) d\lambda_j \right) \quad (5.3)$$

where h is the Planck's constant, c is the vacuum velocity of light, j stands either for pump (p) or for signal (s) light. $i_j^k(x, y, z, \lambda_j)$ are the spectral density profiles. It can be

expressed in terms of transverse mode intensity profiles, $j_0^k(x, y, \lambda_j)$ (normalized over cross-section of the waveguide) and z dependent evolutions in forward and backward directions, $(j^{\pm,k}(z))$:

$$i_j^k(x, y, z, \lambda_j) = P_j^{0,k} j_0^k(x, y, \lambda_j) (j^{+,k}(z) + j^{-,k}(z)) f_j^k(\lambda_j) \quad (5.4)$$

The term $f_s^k(\lambda_s)$ takes the possible longitudinal mode spectrum into account. The amplitudes of the different modes (with a mode spacing $\Delta\lambda_s = \lambda_{s,i+1} - \lambda_{s,i} = \lambda_{s,i}^2 / (2n_{eff}(\lambda_{s,i})L)$ between two neighboring modes) are proportional to the gain spectrum, which is represented by \tilde{f}_s^k :

$$f_s^k(\lambda_s) = \tilde{f}_s^k \sum_i^{N_s} \delta(\lambda_s - \lambda_{s,i}) \quad (5.5)$$

The functions f_j^k are normalized according to $\int_0^\infty f_j^k(\lambda_j) d\lambda_j = 1$.

The evolution of the pump and signal intensity amplitudes $(j^{\pm,k}(z, t))$ along the propagation direction z can be deduced from the equation of continuity for a gain medium [81]:

$$\frac{dj^{\pm,k}(z)}{dz} = \pm \gamma_j^k(z, \lambda_j) j^{\pm,k}(z) \quad (5.6)$$

with

$$\gamma_j^k(z, \lambda_j) = -\tilde{\alpha}_j^k + \int \int (\sigma_{21,j}^k N_2 - \sigma_{12,j}^k N_1) j_0^k dx dy \quad (5.7)$$

The term $\tilde{\alpha}_j^k$ describes the waveguide scattering losses, $\sigma_{21,j}^k N_2$ losses by absorption, and $\sigma_{12,j}^k N_1$ winnings by stimulated emission. The integration has to be carried out over the waveguide cross section taking into account the overlap of the normalized transversal intensity distributions $j_0^k(x, y, \lambda_j)$ with the space dependent population densities N_1 and N_2 , which are themselves proportional to the erbium concentration profile $N_o(x, y)$.

For a given coupled pump power $P_{p,coup}^k$, the signal (pump) power $P_s^{0,k}$ ($P_c^{0,k}$) and its z -dependent intensity amplitude, $s^{\pm,k}(z)(p^{\pm,k}(z))$ described in equation (5.4), can be calculated after solving the equations (5.6) with the proper boundary conditions of the resonator [79, 80]. The forward and backward signal output power can be written as:

$$P_{s,out}^{+,k} = (1 - R_2^s) s^{+,k}(L) P_s^{0,k} = \frac{1 - R_2^s}{\sqrt{R_1^s R_2^s}} P_s^{0,k} \quad (5.8)$$

$$P_{s,out}^{-,k} = (1 - R_1^s) s^{-,k}(0) P_s^{0,k} = \frac{1 - R_1^s}{R_1^s} P_s^{0,k} \quad (5.9)$$

A Fabry-Perot type Ti:Er:LiNbO₃ waveguide laser is easily fabricated by depositing 14 alternating layers of SiO₂ and TiO₂ (thickness of each layer is $\lambda_p/4$) on to the

polished end faces. Usually, the reflectivity spectrum of such a dielectric mirror has a broad wavelength response centering at λ_p . Therefore, the laser oscillation takes place with a number of longitudinal modes (spaced by $\Delta\lambda = \lambda^2/(2n_{eff}L)$). (However, single longitudinal mode of oscillation is obvious for an ideal case: homogeneously broadened medium without hole-burning effects). For a wavelength selective laser oscillation, for example in a DBR laser, at least one of the cavity mirror is replaced by a Bragg grating (either surface relief or photorefractive). In this case, the reflectivity ($R_s(\lambda)$) as a function of wavelength can be calculated by coupled mode theory (see section 2.5) and can be used in equations (5.8) and (5.9). Again, if the grating itself is fabricated in the gain medium, a wavelength selective laser oscillation (DFB laser) is possible even in the absence of additional feedback mirrors. The principle of a DFB laser can be completely understood by analyzing coupled mode theory (see Fig. 2.6) [32, 82]. However, if a waveguide laser is made by combining a DFB-structure, amplifier and/or a dielectric mirror, etc., the laser emission can be understood by the superpositions of different effective Bloch waves or the method of multiple reflections [83, 84].

5.3 DBR-Laser with One Grating

The first DBR-laser with one photorefractive grating was already developed in our group by Christian Becker during his Diploma (Master) thesis work [77]. This laser was reinvestigated during the present thesis work. It is found to be equally efficient even 2 year after its fabrication. No observable degradation of the efficiency of the fixed photorefractive grating is observed. For the consistence and completeness of this thesis, the description and the performance of this laser are presented here once again.

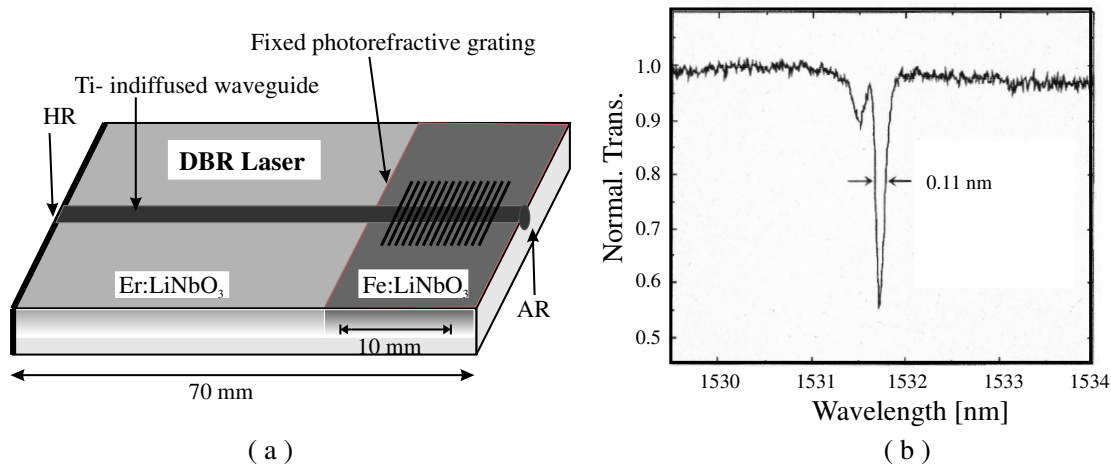


Fig. 5.2: (a) Schematic structure of the DBR-laser with one photorefractive grating and (b) normalized transmission characteristics of the grating in TE-polarization (sample: Pb874xz).

Device Description:

A schematic diagram of the DBR-laser fabricated with one thermally fixed photorefractive grating is presented in Fig. 5.2a. The laser was fabricated in a 70 mm long X-cut LiNbO₃ substrate that had been Er-doped over 43 mm by indiffusion and the remaining surface was Fe-diffusion doped (sample: Pb874xz). A 8 μm wide, 97 nm thick photolithographically defined Ti-stripe parallel to the c-axis was indiffused, forming the optical channel guide. The sample was then annealed at 500 $^{\circ}\text{C}$ during 3 hrs in flowing Ar (0.5 litre/min) to enhance the necessary photorefractive sensitivity.

The laser resonator consists of a broadband dielectric high reflector on the polished waveguide end face of the Er-doped section and of a narrowband grating reflector in the Fe-doped section. In addition, the polished end face of the waveguide near the grating was antireflection coated for fiber butt coupling. A 10 mm long photorefractive Bragg grating ($\Lambda \sim 346$ nm) was thermally fixed (at 170 $^{\circ}\text{C}$) in the Fe-doped waveguide section with a holographic exposure of 2 hrs. The reflectivity of the fixed

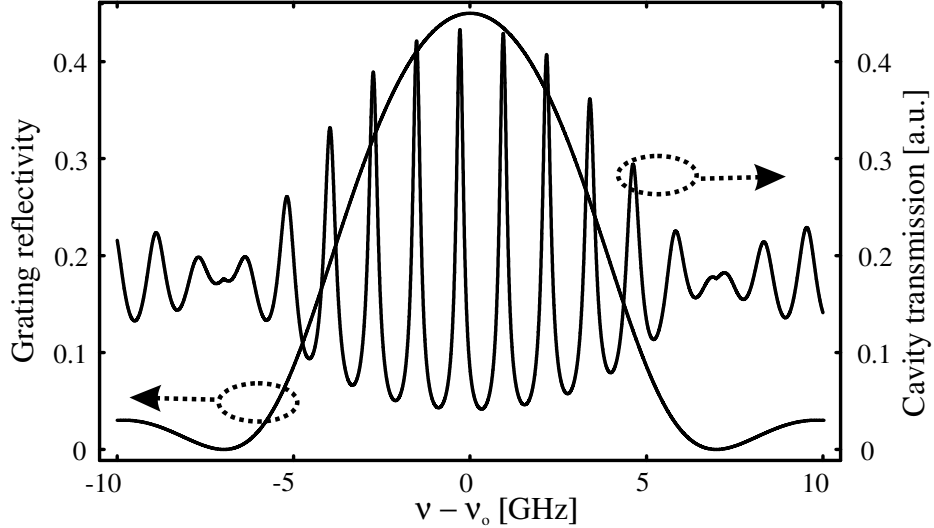


Fig. 5.3: Calculated grating response and transmission of a passive DBR-cavity (equivalent to the DBR-laser comprised of one grating, Fig. 5.2a) as a function of frequency deviation from the Bragg frequency of the grating.

grating was measured to be $> 40\%$ at $\lambda = 1531.7$ nm (see Fig 5.2b). The spectral linewidth of the grating was 0.11 nm (~ 14 GHz) measured with an OSA of 0.1 nm resolution bandwidth. The calculated grating reflectivity response and the passive longitudinal cavity resonances are shown in Fig. 5.3. It is evident from this figure that more than one longitudinal laser mode can oscillate simultaneously in a DBR-laser with one grating.

Operation and Properties:

To operate the laser a fiber-pigtailed diode laser ($\lambda_p = 1480$ nm) was used for pumping. The pump radiation was coupled to the DBR laser through the photorefractive grating and double-pass pumping could be achieved because of the broadband dielectric mirror on the other side. (Whereas in case of a DBR-laser with a surface relief Bragg grating the pump radiation could not be coupled through the grating because of substrate mode excitation in the grating section [19]).

A fiber-optic wavelength division de-multiplexer (WDM) was used to launch the pump power and to extract the laser output (see Fig. 5.4a). An in-line fiber-optic isolator was also used in the signal branch to avoid the back-reflections from other optical components used to characterize the laser. Laser emission could be achieved in both TE and TM polarization. The actual polarization was determined by the location of the actual eigen-modes with respect to the peak reflectivity of the Bragg reflector. By thermal drift, alternating TE and TM emission could be observed. However, TE polarization for both pump and emission yielded the maximum output power, as the smaller TE modes resulted in a better overlap with the Er concentration profile. To

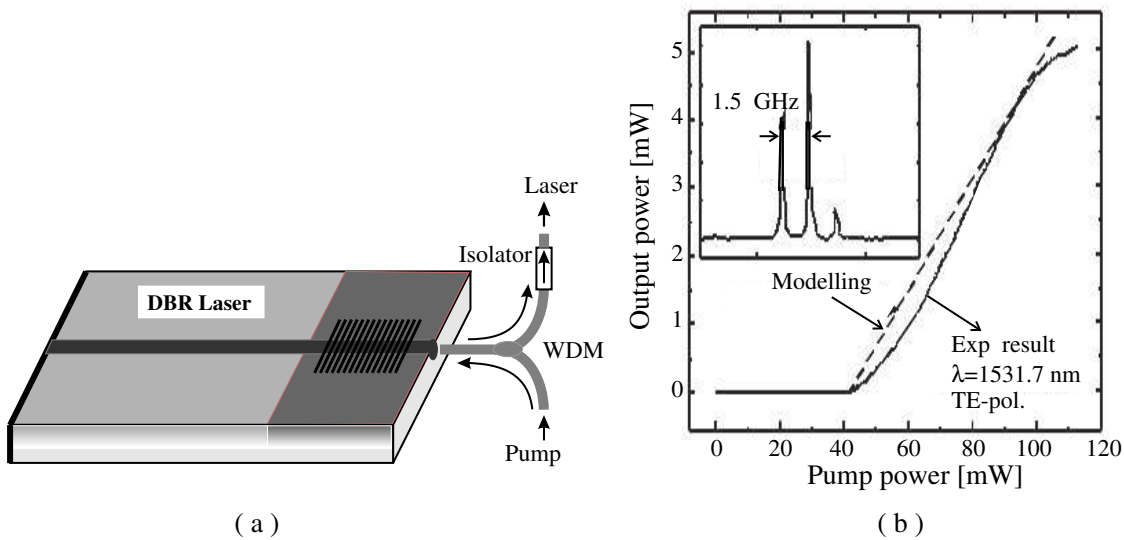


Fig. 5.4: (a) Operation scheme of the DBR-laser with one photorefractive grating. (b) The power characteristics. Inset: Scanning Fabry-Perot spectrum with three longitudinal modes of laser oscillation, Pump: TE, Laser: TE.

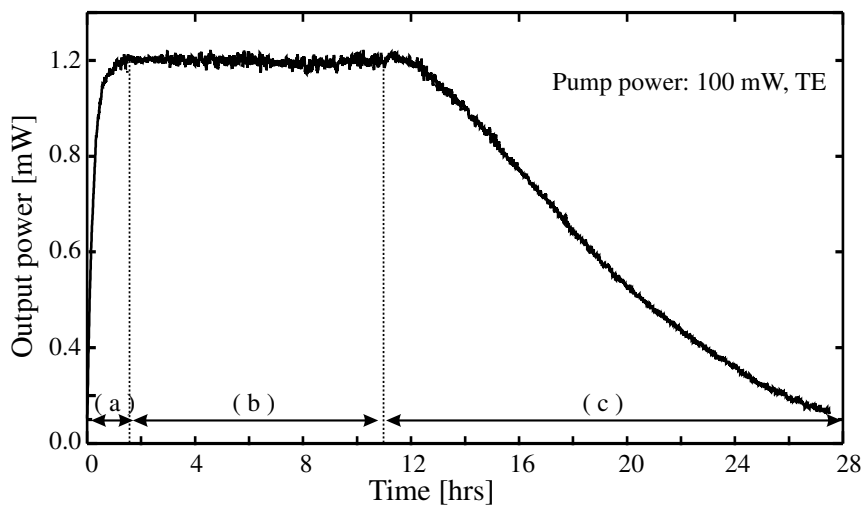


Fig. 5.5: The performance of the packaged DBR-laser with one photorefractive grating as a function of operating time obtained 2 years after its fabrication (sample: Pb874xz) (a) grating is illuminated by an array of blue LEDs; the output power becomes maximum as the grating is refreshed to maximum reflectivity, (b) laser output power remains constant as long as the grating is illuminated and (c) the laser output starts decaying after the illumination is switched off. Pump: TE, Laser: TE.

suppress the TM emission completely a stripe of silver paste was deposited across the waveguide close to the high reflector operating as a TE-pass polarizer. From the power characteristics of the laser shown in Fig. 5.4b it is evident that lasing sets in at about 40 mW of launched pump power. The maximum output power of 5 mW was measured for a pump power level of 110 mW. The emission wavelength of the laser was at 1531.7 nm clearly determined by the grating response shown in Fig. 5.2b.

After the laser characterization, a single-mode standard telecommunication fiber was glued to the antireflection coated waveguide end face (pigtailling); finally, the sample was packaged in a temperature stabilized aluminum box. After packaging of the sample, the laser was characterized once again. In comparison with the results presented in Fig 5.4b, the maximum output power was slightly reduced due to non-ideal fiber pigtailling.

During laser operation because of the electronic compensation, the fixed ionic grating response dies out and the laser performance degrades with time. Therefore, each time before laser operation the grating requires a refreshing exposure (as described in Chapter 4). The grating response could be even kept constant during laser operation by continuously illuminating with light from an array of blue LEDs. The performance of the packaged DBR-laser as a function of time was characterized two years after its fabrication and the corresponding results are given in Fig. 5.5.

5.4 DBR Laser with Two Gratings

The DBR-laser with one grating was not capable to run on a single longitudinal mode as we have seen in the last section. True single frequency emission could be achieved by replacing the broadband dielectric mirror of the DBR-laser by another narrow-linewidth photorefractive grating [34,35]. The laser is now fully integrable, i.e., it can be placed anywhere (aligned parallel to the Z-axis) on a substrate of an integrated photonic circuit.

Device Description:

The structure of the DBR-laser with two photorefractive gratings is shown in Fig. 5.6a. It was also fabricated in the surface of a X-cut LiNbO₃ crystal (sample: Pb106xz) with a 80 mm long Z-propagating single-mode waveguide. The middle section of 50 mm length was Er-doped and the two remaining sections on both sides of 15 mm length were Fe-doped. In these sections two thermally fixed photorefractive gratings R₁ and R₂ were fabricated, respectively.

Both gratings have the same period ($\Lambda \sim 352$ nm) and were fixed at 180 °C, but had to be fabricated one after another because only one grating can be fabricated at a time using our holographic setup. The grating R₁ was fabricated first with a holographic exposure of 8 min. Afterwards, R₂ was fabricated with a holographic exposure of 6 min. During the fixing process of R₂ at 180 °C, the sample was placed in a specially designed oven so that the temperature of the other grating section (R₁) was maintained around room temperatures. This was necessary because a fixed “ionic” grating can be erased easily at elevated temperatures (> 80 °C).

The transmission characteristics of the individual gratings are shown in Fig. 5.6b with nearly identical Bragg wavelengths near $\lambda_B = 1561.1$ nm. The reflectivity and linewidth of grating (R₁) are 90% and 200 pm (24 GHz), respectively, whereas the corresponding figures of the grating (R₂), which serves as output coupler, are 60% and 60 pm (7 GHz), respectively. These properties were observed when the gratings were homogeneously illuminated with light of an Ar laser ($\lambda = 488$ nm, $I = 100$ mW/cm²); the transmission characteristics was monitored by an OSA of resolution bandwidth of 10 pm. When the light was switched off, the grating efficiencies decayed with time in about 120 min (20 min) for R₁ (R₂) to half of its maximum response due to electronic compensation by the dark conductivity. However, it took only 20 min to refresh the gratings; they continued to keep their maximum efficiencies as long as they were illuminated as usual (see Fig. 5.6c). These gratings could be kept refreshed for a long duration by an array of blue LEDs without any additional photorefractive damage.

The calculated longitudinal modes of the DBR-cavity comprised of both gratings R₁ and R₂ are shown in Fig. 5.7 along with the calculated grating response equivalent to R₂. It is evident from the result that the longitudinal mode nearer to the

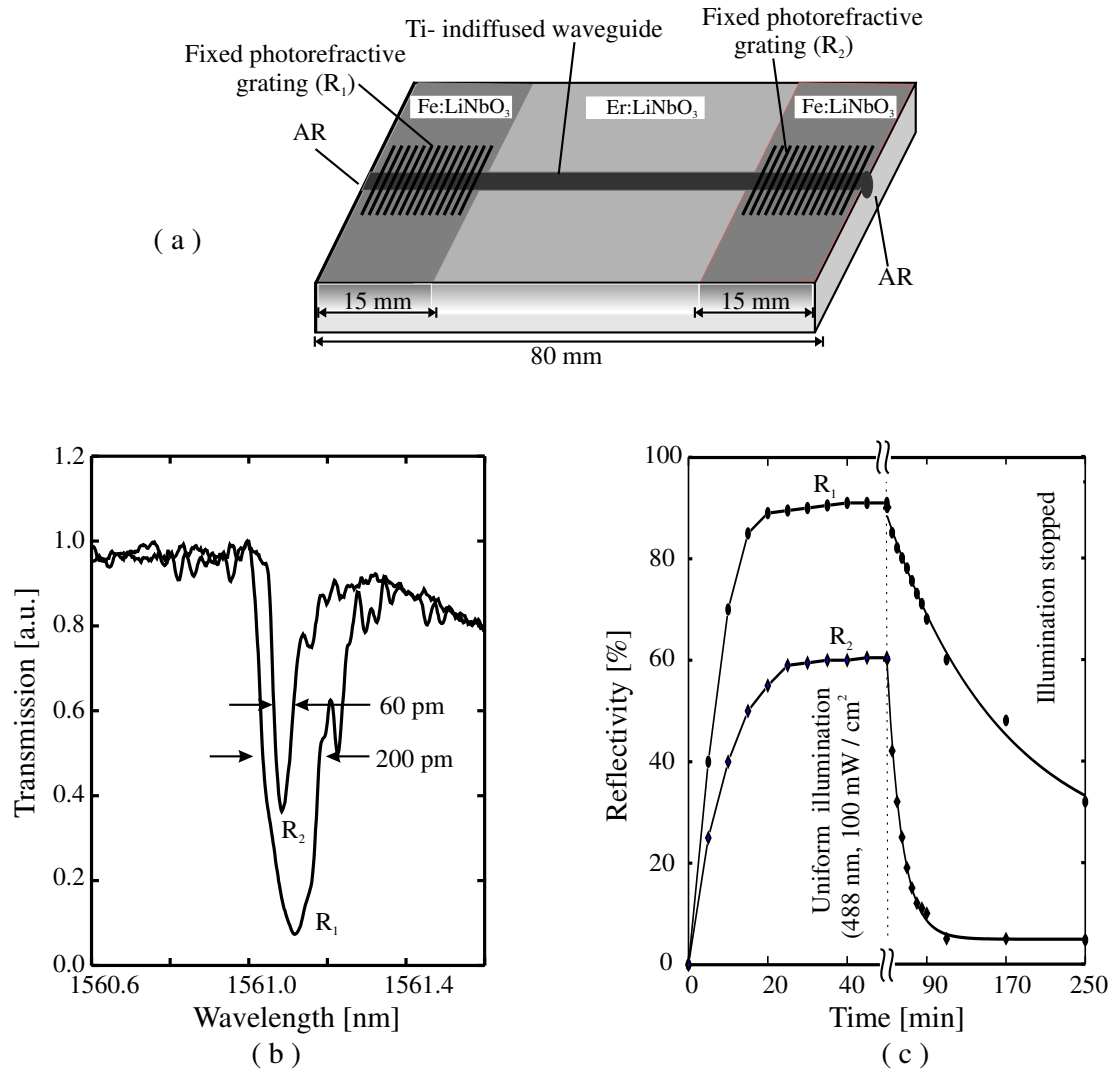


Fig. 5.6: (a) Schematic structure of the DBR-laser with two fixed photorefractive gratings (sample: Pb106xz), (b) transmission characteristics of the gratings in TE-polarization and (c) development of the gratings by uniform illumination and decay after stopping the illumination.

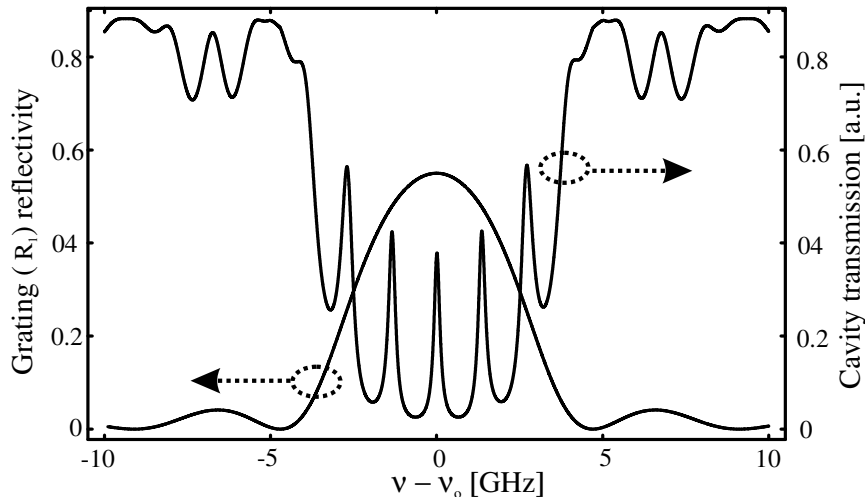


Fig. 5.7: Calculated grating response (R_2) and transmission of a passive DBR-cavity (equivalent to the DBR-laser comprised of two gratings (R_1, R_2), Fig. 5.6a) as a function of frequency deviation from the Bragg frequency of the grating.

Bragg response has reasonably high degree of resonance compare to its neighboring two modes. Therefore, a single-frequency laser operation is likely.

Operation and Properties:

The DBR-laser was pumped using a fiber-pigtailed diode laser with an emission spectrum centered at ~ 1480 nm wavelength, the optimum pump wavelength for α -polarization in the Ti:Er:LiNbO₃ waveguide. The pump light was fed into the laser resonator through the output coupler grating R_2 via the common branch of a WDM (see Fig. 5.8a). The laser output was extracted through the second branch of the WDM and guided through an inline fiber-optic isolator to protect the DBR-laser from optical feedback. During operation the two photorefractive gratings of the laser cavity were continuously illuminated by a uniform low intensity of Ar laser light ($\lambda = 488$ nm, $I = 100$ mW/cm²).

The power characteristics of the laser is shown in Fig. 5.8b. Lasing sets in at about 70 mW of incident pump power measured at the output of the common branch of the WDM; the emission wavelength was 1561.1 nm. The laser was always running in TE-polarization independent on the pump polarization (TE/TM). This might be due to a slightly lower waveguide loss for the TE-mode compared to TM-mode. With 120 mW of incident pump power (P_p) an output power (P_{out}) of 1.1 mW was achieved, measured behind the isolator; the corresponding slope efficiency (dP_p/dP_{out}) is about 2 %.

Using a high resolution OSA we could clearly identify that the DBR-laser runs in a single longitudinal mode of the cavity in TE-polarization (see Fig. 5.9a). It was running half an hour without any observable wavelength fluctuations. The observed

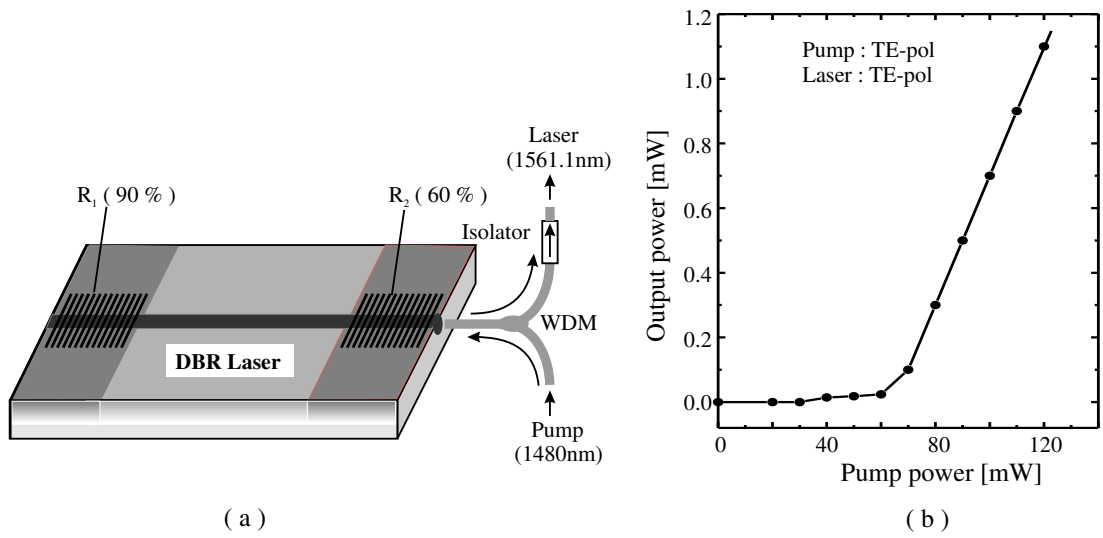


Fig. 5.8: (a) Operation scheme of the DBR-laser with two photorefractive gratings (b) The power characteristics as output power versus coupled pump power.

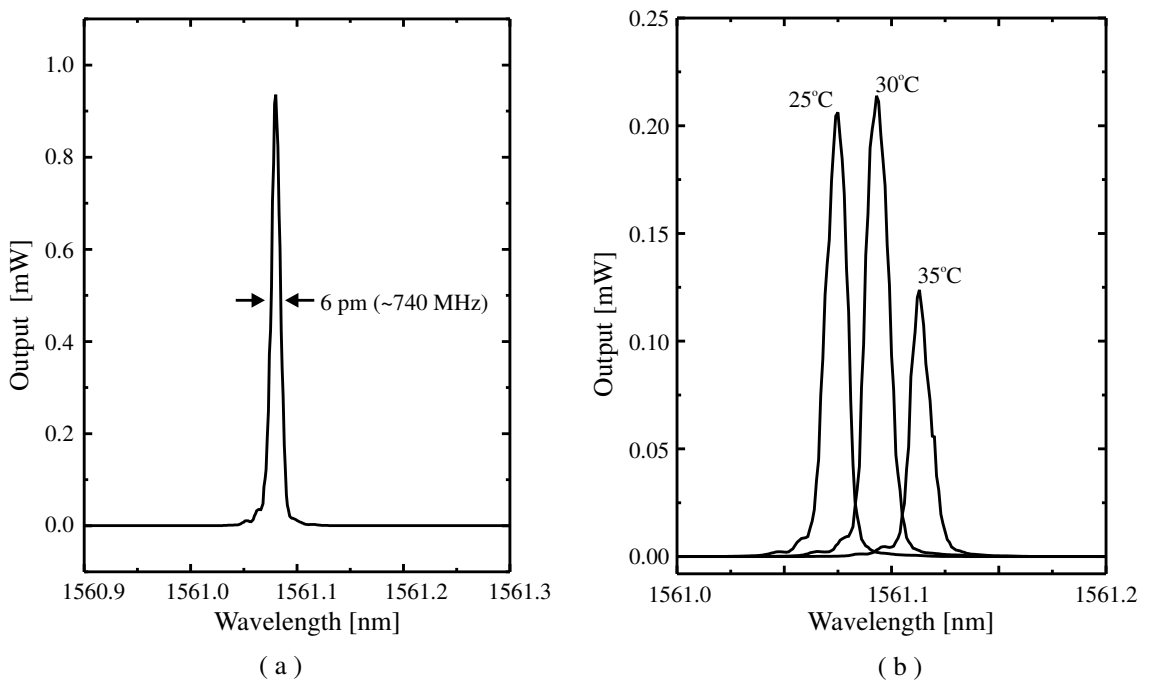


Fig. 5.9: (a) Spectral characteristics (TE) of the DBR-laser. (b) Tuning characteristics of the DBR-laser; the high reflector grating R_2 was kept at room temperature, while the output coupler grating R_1 was temperature tuned.

linewidth of ~ 0.75 GHz is clearly limited by the resolution of the OSA. A much better resolution (scanning Fabry-Perot or delayed self-heterodyne technique) is required to resolve the true laser linewidth of estimated < 10 kHz as observed with a surface etched device [17].

As the linewidth of the high reflector grating is broader (200 pm) than that of the output coupler grating (60 pm), thermal tuning of the lasing wavelength was possible via the temperature of the output coupler alone (see Fig. 4.8b). We achieved a mode-hop free tuning range of about 80 pm (~ 10 GHz) with a slope of 8 pm/K (~ 1 GHz/K). A wider tuning range can be obtained by an additional temperature shift of the high reflector grating.

5.5 DFB Laser/Amplifier

By writing the holographic grating in a Ti:Fe:Er:LiNbO₃ waveguide section even a fully integrable DFB-laser can be realized [36, 37]. In this work basically we have investigated an integrated optical DFB-laser/amplifier combination has been developed.

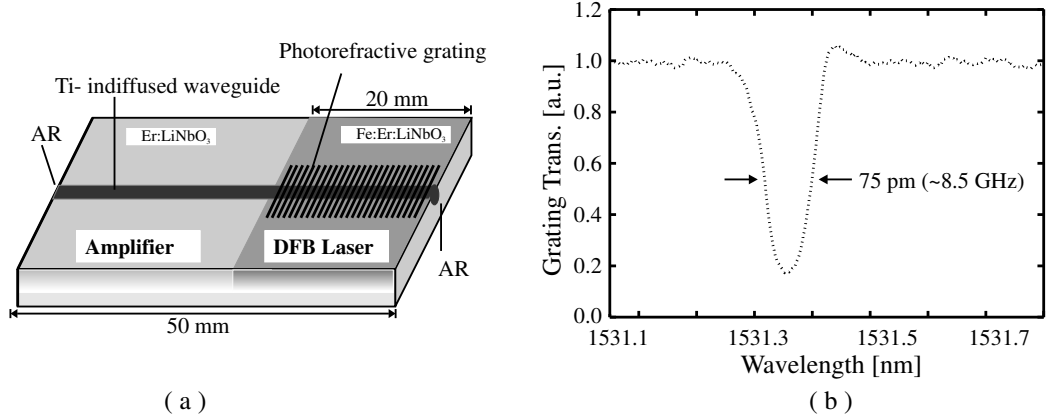


Fig. 5.10: (a) Schematic structure of the DFB-laser/amplifier with a fixed photorefractive grating (sample: Pb107xz), (b) transmission characteristics of the grating in TE-polarization.

Device Description:

The laser was fabricated in the surface of a 50 mm long, 12 mm wide and 1 mm thick optical grade X-cut LiNbO₃ crystal (sample: Pb107xz) with the optical- (Z-) axis aligned parallel to the direction of the optical waveguide (see Fig. 5.10a). The whole surface of the sample is Er-doped whereas a section of 20 mm width was Fe-doped as well. Therefore, a single-mode ($1470 \text{ nm} < \lambda < 1580 \text{ nm}$) waveguide parallel to the Z-axis has a 30 mm long Er-doped section and a 20 mm long Er/Fe codoped section. Both polished end faces were antireflection- (AR-) coated for $\lambda \sim 1550 \text{ nm}$.

From DFB-laser modelling we learned that both, the optical gain and the feedback in the amplifying grating structure should be as high as possible to get an acceptable laser threshold. We therefore decided to write the active DFB-grating ($\Lambda \sim 346 \text{ nm}$) for 1531 nm wavelength, where the optical gain in the Er-doped waveguide can even exceed 1.5 dB/cm sufficient pump power provided. Using our standard holographic setup, an exposure time of only 2 min was sufficient to get a grating peak reflectivity exceeding 80%. The spectral linewidth measured in transmission was $\sim 75 \text{ pm}$ ($\sim 8.5 \text{ GHz}$) (see Fig. 5.10b). As a reflectivity $\sim 90\%$ was necessary to achieve lasing, fixed (ionic) photorefractive gratings could not be used; their maximum reflectivity did not exceed 80%.

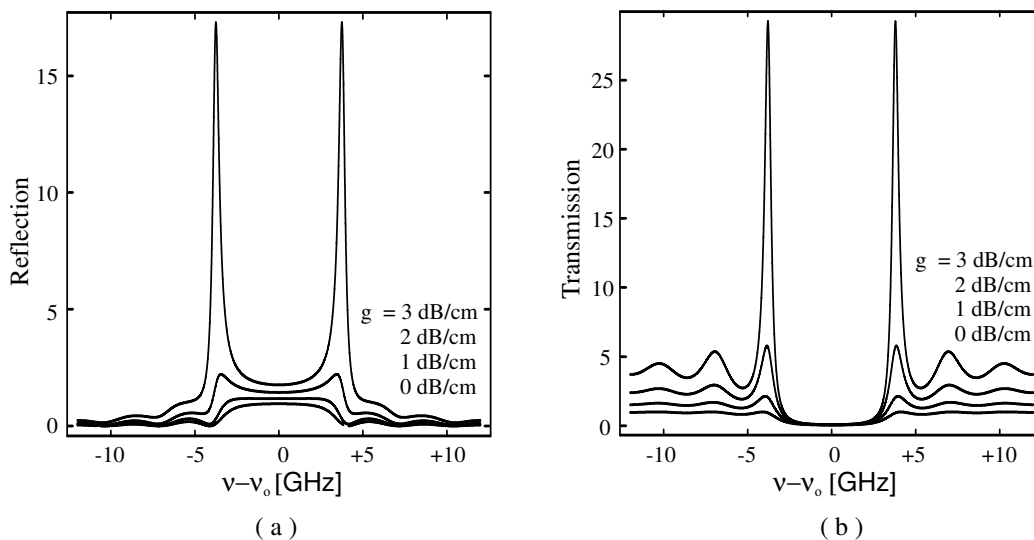


Fig. 5.11: (a) Calculated reflection and (b) transmission of a 20 mm long DFB-laser structure at different gain levels: the passive grating reflectivity is taken as 95%.

The reflection and transmission spectra for the 2 cm long DFB-laser structure with different gain levels have been calculated using coupled mode theory (see Fig. 5.11). It is evident from both spectra that two peaks just outside the stop band of Bragg grating start arising as the gain level approaches to a certain threshold. These peaks finally appears as the two lowest order DFB-laser modes (theoretically infinite reflection) just above the threshold gain.

In contrast to the DFB-laser discussed above, if a DFB-laser structure is integrated with an amplifier section as shown in Fig. 5.10a, the result is somewhat different. In this case there are also have two symmetric peaks in both reflection and transmission spectra but they appear within the stop band of the grating response [84]. Therefore, in this case the threshold gain is reduced reasonably as the two lasing-modes are within the Bragg response of the grating.

Operation and Properties:

The pump light ($\lambda_p = 1480$ nm) of two laser diodes was coupled from the right- and from the left-hand side into the waveguide structure (see Fig. 5.12a) during holographic exposure for grating definition. Fiber-optic wavelength- (de-) multiplexers allowed extracting the laser emission, which sets in at a launched pump power level of about 175 mW. The maximum of the output power emitted to the right was ~ 95 μ W at about 240 mW total launched pump power. At the same pump power level 1.12 mW was emitted to the left, thanks to the optical gain of more than 10 dB in the 30 mm long Er-doped waveguide amplifier on the left of the DFB-structure. Fig. 5.12b gives the power characteristics of the laser. The emission wavelength of the laser was ~ 1531.4 nm, clearly determined by the grating characteristics. The two distinguished

DFB-laser/amplifier modes in the emission spectrum could already be resolved with an optical spectrum analyzer of 10 pm resolution; their wavelength separation is ~ 27 pm.

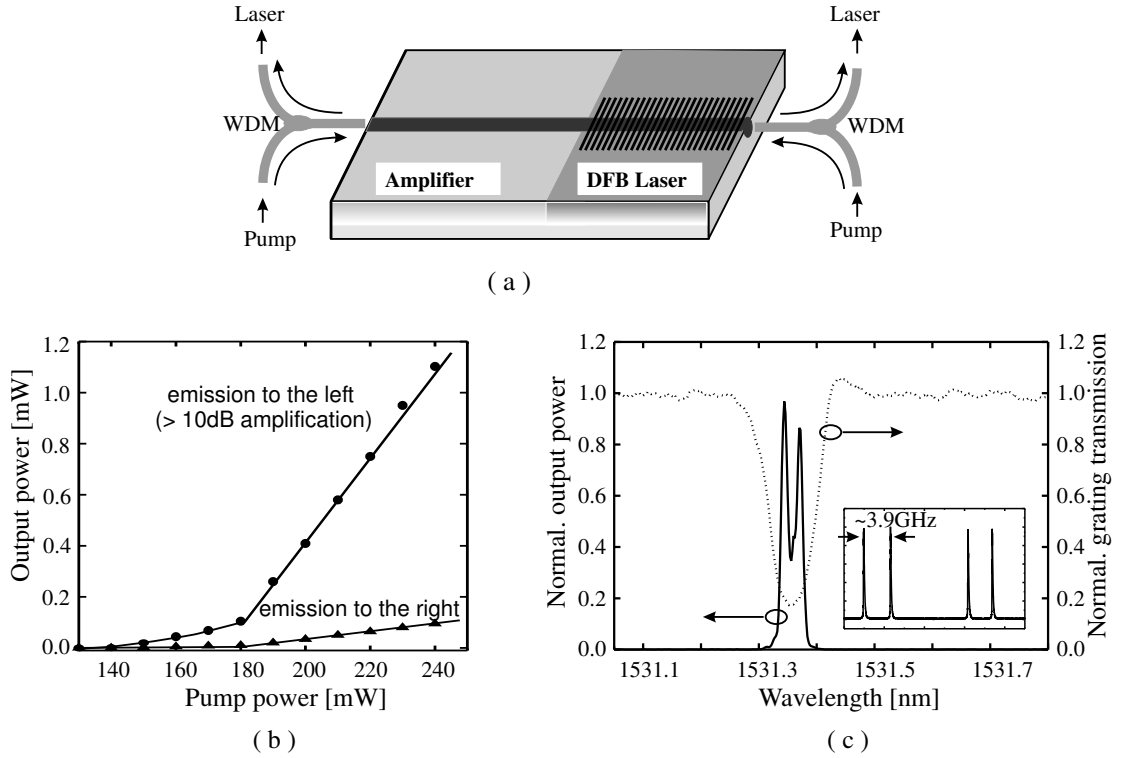


Fig. 5.12: (a) Operation scheme of the DFB-laser/amplifier, (b) laser output vs. launched pump power and (c) laser emission spectrum consists of two peaks. Inset: two lasing modes are better resolved by a scanning Fabry-Perot spectrum analyzer of 15 GHz free spectral range.

The emission spectrum is shown in Fig. 5.12c together with the grating response. It is evident that the emission lines arise symmetrically on both sides of the peak reflectivity in accordance with theory. The separation of the two emission frequencies was even better resolved with a scanning Fabry-Perot spectrum analyzer; a figure of 3.9 GHz was measured. Besides emission of both modes in TE-polarization, also emission in TM-polarization was sometimes observed. The cause of the polarization flipping is not yet known.

5.6 DFB-DBR Coupled Cavity Laser

With a little modification of the DFB-laser/amplifier described above an attractive DFB-DBR coupled cavity laser was developed [38, 39]. Single-frequency emission could also be achieved with this laser configuration. It has a low threshold pump power level and a higher slope efficiency.

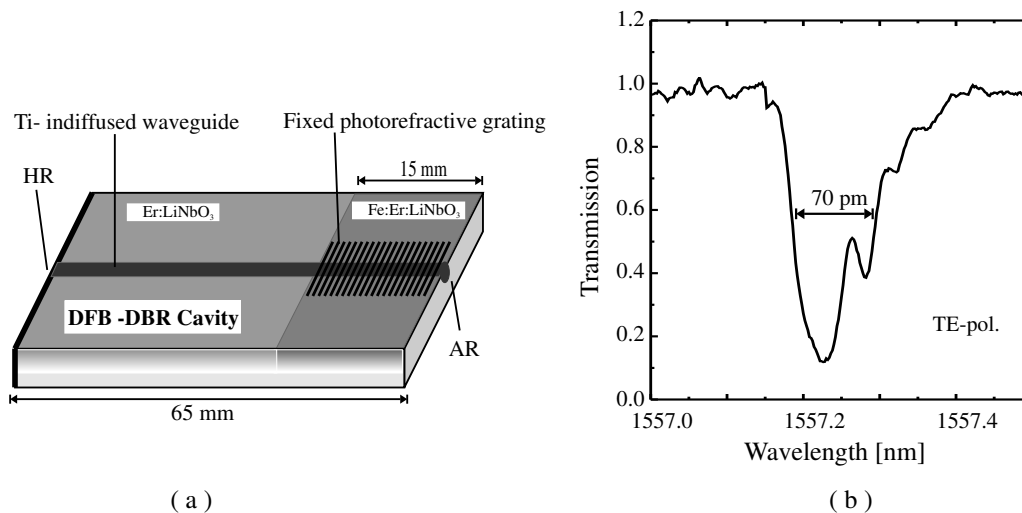


Fig. 5.13: (a) Schematic diagram of the DFB-DBR coupled cavity laser (sample: Pb150xz). (b) The transmission characteristics of the fixed grating fabricated in Ti:Fe:Er:LiNbO₃ waveguide section and refreshed by Ar laser light ($\lambda = 488$ nm, $I = 250$ mW/cm²).

Device Description:

As usual the laser was fabricated in the surface of a 65 mm long, 12 mm wide and 1 mm thick optical grade X-cut LiNbO₃ crystal (sample: Pb150xz). A 7 μ m wide Ti-indiffused waveguide aligned parallel to the Z-(optical-) axis, has a 50 mm long Er-doped section and 15-mm-long Er/Fe codoped section (see Fig. 5.13a). The polished end face on the Fe-doped side was AR- (antireflection-) coated whereas the other polished end face was HR- (high reflection) coated.

Finally, a 14 mm long photorefractive Bragg grating was written in the Fe-doped waveguide section using our standard holographic setup using an argon-ion laser ($\lambda = 488$ nm, $P = 1$ W). It was fixed at 180 °C by a holographic exposure of 4 min, followed by a rapid cooling of the sample down to room temperature to get a fixed ionic (protonic) grating of 352 nm periodicity. It was developed by a uniform illumination with blue light either from an Ar laser or an array of blue LEDs.

The transmission characteristics of the grating was measured with an OSA of 10 pm resolution by monitoring the transmitted amplified spontaneous emission of an

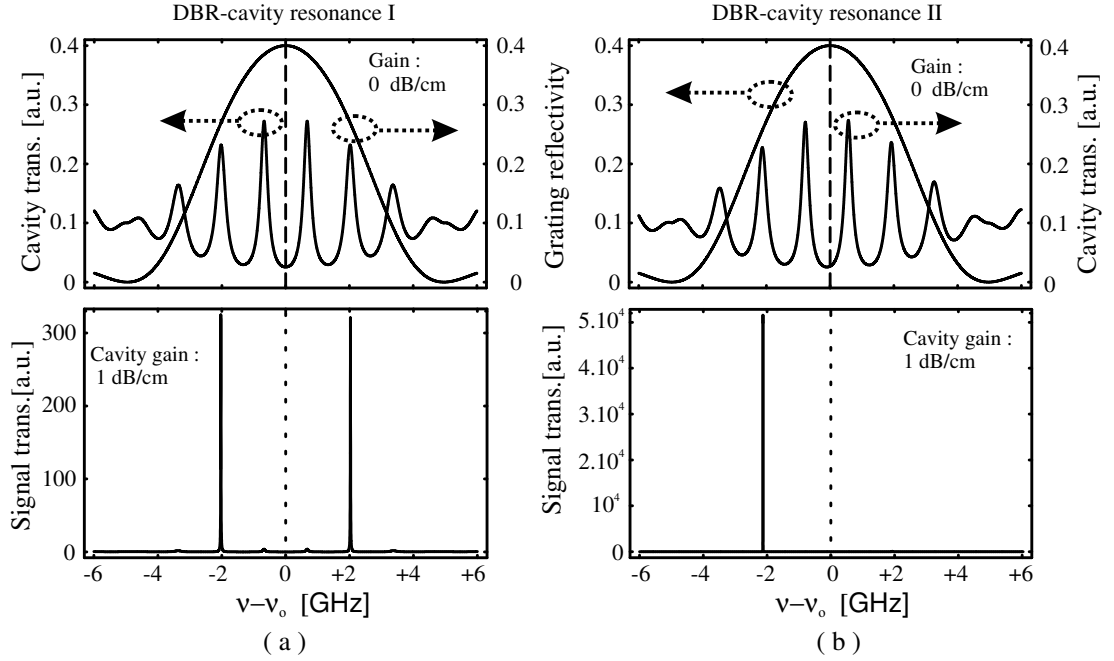


Fig. 5.14: Theoretical demonstration of the two extreme situations of the DFB-DBR coupled mode of laser oscillations (a) Two DBR-cavity modes are symmetrical to the two lowest order “lasing-modes” of the DFB-laser/amplifier combination; their frequencies do not coincide. (b) One DBR-cavity mode is exactly resonant to one of the two lowest order “lasing-modes” of the DFB-laser/amplifier combination; their frequencies do coincide.

EDFA through the grating. Up to 90% peak reflectivity (deduced from the transmission spectrum) could be achieved if the Ar laser ($\lambda = 488$ nm, $I = 250$ mW/cm², 20 min exposure time) was used to develop the ionic grating. After the development the grating slowly decays due to the electronic dark conductivity. It can be refreshed again up to 75% peak reflectivity by an array of 8 blue LEDs within 30 min. The spectral half-width of the polarization independent grating response is 70 pm (~ 8.5 GHz). However, the laser is operated with the grating of reflectivity $\sim 40\%$. Moreover, during laser operation it could be observed that the grating becomes almost stabilized as function of time at about 30% reflectivity without any additional blue illumination from outside. This favorable self-stabilization is probably due to the green up-conversion light produced in the Er-doped grating itself (details are given in Chapter 4).

For a theoretical investigation we assumed that the device consists of two laser-active cavities: the 14 mm long grating section alone is a DFB-laser cavity; the high reflector (HR) together with the grating forms a DBR-cavity with a 50 mm long waveguide section. Therefore, the two lowest order “lasing-modes” of the DFB-laser/amplifier combination can easily resonant with the DBR-cavity modes. Using coupled mode

theory, the above hybrid cavity is analyzed. Fig. 5.14 shows the two extreme laser oscillation situations corresponding to two DBR-cavity resonances. Single-frequency laser oscillation is expected if one of the DBR-cavity modes coincides with one of the two lowest order “lasing-modes” of the DFB-laser/amplifier combination (as shown in Fig. 5.14b).

Operation and Properties:

For laser operation the pump light ($\lambda = 1480$ nm) is fed into the laser resonator through the grating via the common branch of a fibre-optic WDM. The laser output is extracted through the second branch of the WDM and isolated to protect the laser from optical feedback (see Fig 5.15a). In our experiment we observed at low pump power levels laser operation is determined essentially by the DBR-cavity. Single-frequency emission at 1557.2 nm wavelength with a linewidth <185 MHz could be observed by a Fabry-Perot spectrum analyzer. The exact frequency of the laser emission is determined by the frequency of that DBR-cavity mode ($\Delta\nu_{DBR} \sim 1.4$ GHz) closest to the reflectivity maximum of the grating. The threshold of this mode is achieved at about 100 mW incident pump power corresponding to ~ 80 mW launched power. However, slightly above the threshold pump power the laser tends to oscillate in more than one DBR-mode.

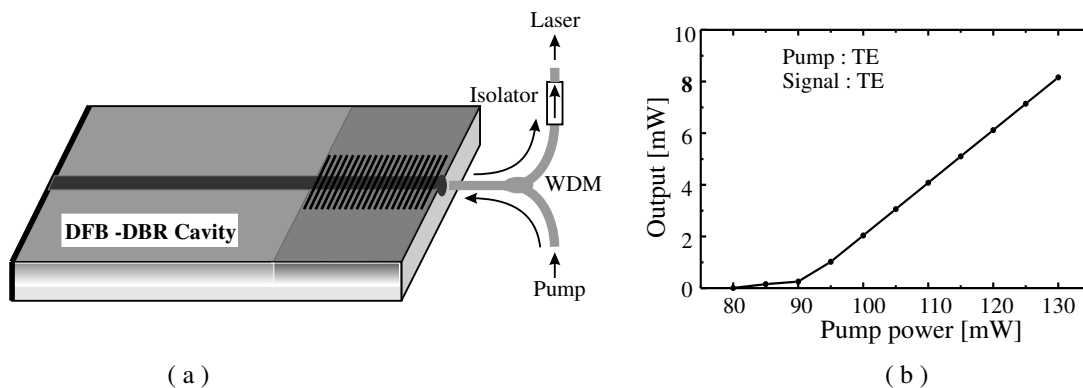


Fig. 5.15: (a) Operation scheme of the DFB-DBR coupled cavity laser and (b) Laser output versus launched pump power: laser emission at ~ 1557.2 nm.

At higher pump power level (> 90 mW) a DFB-DBR coupled mode of laser oscillation sets in. In this regime, a maximum output power of 8 mW is obtained at 130 mW pump power. This corresponds to a slope efficiency of about 22% (see Fig. 5.15b). In contrast to the DBR-mode of operation, now simultaneous emission at two frequencies can be observed frequently, separated by ~ 3.8 GHz (see Fig 5.16a). Both, the threshold pump power and the observed frequency spacing of the two lasing modes, are smaller than the theoretical results of a pure DFB-laser, clearly indicating the influence of the integrated amplifier section and the cavity formed by the high-reflector dielectric mirror. The coupled-mode of laser operation is determined by the amplified

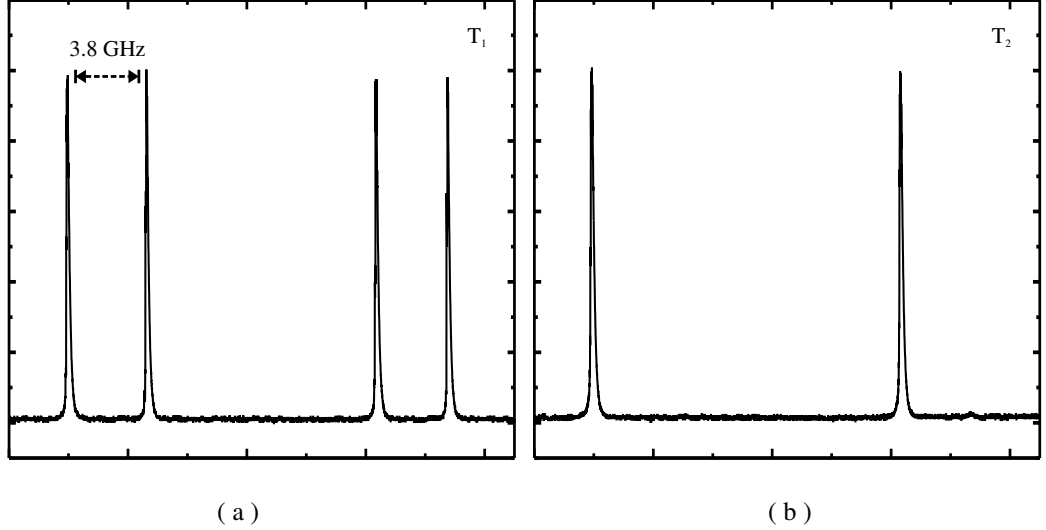


Fig. 5.16: Scanning Fabry-Perot spectra of the DFB-DBR coupled cavity laser obtained at two different temperatures; (a) two modes at temperature T_1 and (b) single-frequency laser emission at temperature T_2 . $T_1 - T_2 \sim 1$ °C. (See also Fig. 5.14 for an explanation).

spontaneous emission at the two distinguished frequencies of the DFB-laser/amplifier combination in the wings of the reflectivity spectrum of the 14 mm long amplifying grating. They determine the laser oscillation frequencies in the longer DBR cavity, if two DBR-modes are resonant or (symmetrically) close to resonance with the two DFB-laser/amplifier modes. However, the DBR-cavity modes can shift as function of temperature ($\Delta\nu_{DBR}/\Delta T \sim 700$ MHz/°C), electric field ($\Delta\nu_{DBR}/\Delta V \sim 92$ MHz/V) etc., leading to a resonance of one frequency with one DBR-cavity mode only at appropriate temperatures. As a result single-frequency emission can be achieved (see Fig. 5.16b).

Dynamics of the Laser Output Power:

The DFB-DBR coupled cavity laser is characterized in terms of the output power as a function of time with different operating conditions (see Fig. 5.17). In the first experiment the pump laser and the grating refreshing LEDs were switched on together. After a few minutes, the laser emission started and reached maximum output power within 20 min. An almost constant output power was recorded for 3 hrs as the refreshing light switched on. The almost same output power was recorded for another 4 hrs. even after switching off the grating refreshing light. At the end, after complete 7 hrs of laser operation the grating reflectivity was measured to be 30%. During the whole experiment polarization flippings were observed from time to time but not frequently.

For the second experiment, the grating was initially refreshed to a peak reflectivities of 70% and 40%, respectively. Then the laser was pumped (130 mW, TE-polarized)

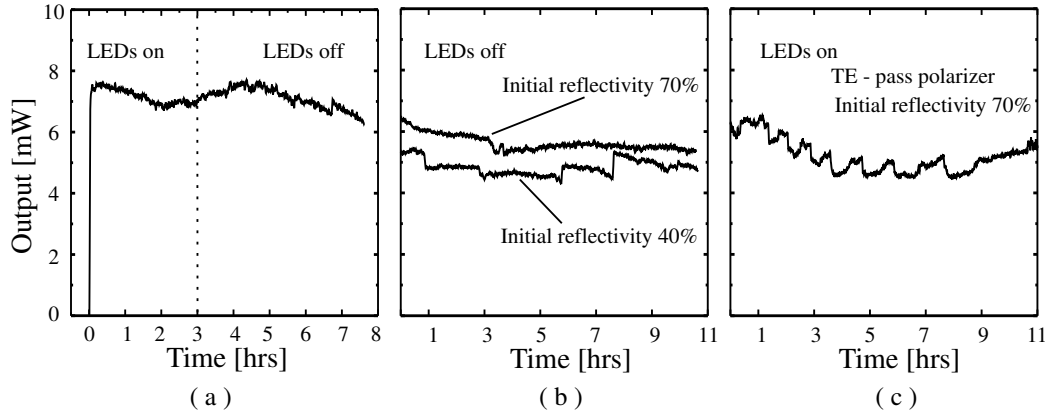


Fig. 5.17: Different dynamical behavior of the pumped DFB-DBR coupled cavity laser; (a) first few hours grating was kept refreshed by the illumination of an array of LEDs and then no illumination, (b) laser started running with refreshing illumination of the grating but with a initial refreshment of the grating, and (c) TE-passed polarized laser started running with a initially refreshed grating. Pump power: 130 mW, TE-polarized

without any grating refreshment exposure and the output was recorded for more than 10 h. It was found that for 70% (initial) grating reflectivity, the laser output continued to decrease during the first few minutes and later on almost stabilized. But for the 40% (initial) grating reflectivity, a nearly stabilized output power was recorded as function of time. The step-like jumps observed in the laser output power were due to polarization flippings. At the end of laser operation with 70% and 40% initial grating reflectivity, the grating reflectivities were measured again; they had reached $\sim 30\%$.

Finally, for the third experiment a TE-pass polarizer (Ag paste) was deposited close to the high reflector. The laser output was recorded as a function of time using 130 mW of TE-polarized pump power and grating refreshment LEDs were switched on. In this case, although TE-polarized laser output was always maintained, flipping between the two “DFB-lasing-modes” of 3.8 GHz separation could be observed with regular interval of time. After 11 hours of laser operation the grating reflectivity once again was measured to be about 30%.

In conclusion, after the above three experiments one can assume that the green fluorescence (due to up-conversion of the excited Er^{3+} ions) nearly stabilize the fixed grating response, which usually experiences a decay due to a residual conductivity. The polarization flipping could be suppressed completely by integrating a TE-pass polarizer at the proper position. Flipping between the “lasing-modes” can be suppressed with a better temperature control and/or electrooptic control.

Wavelength Tuning:

The emission wavelength of a DFB-DBR coupled cavity laser can be tuned by tuning

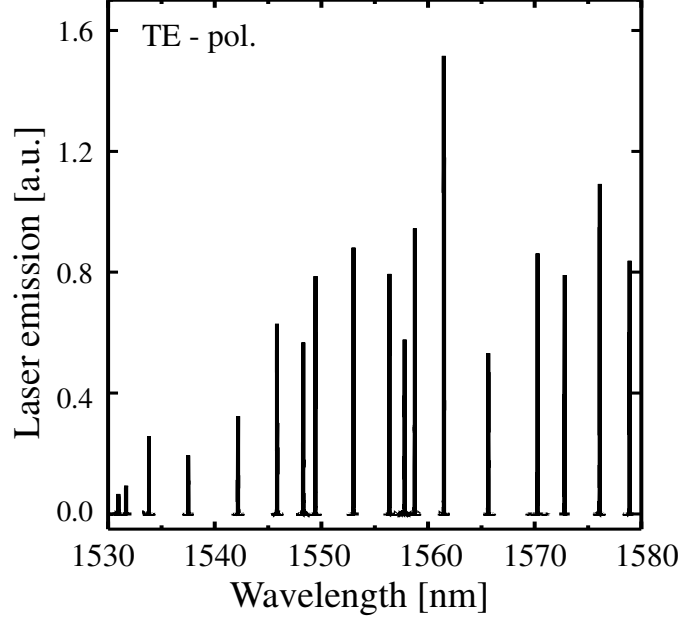


Fig. 5.18: Wavelength tuning of DFB-DBR coupled cavity laser with different grating periodicity (sample: Pb150xz); (a) laser emission in TE-polarization. Pump power: 130 mW, TE-polarized, grating reflectivities were $> 80\%$

the Bragg wavelength of the grating response. This is possible either by tuning the grating periodicity Λ and/or by tuning the effective refractive index n_{eff} of the guided mode. At room temperature the photorefractive Bragg gratings could be written for different wavelengths by simply tuning the angle (2θ) between the writing beams. In this way we could tune the emission wavelength in the wide range from $1.53 \mu\text{m} < \lambda < 1.64 \mu\text{m}$. Some results are given in Fig 5.18.

Electro-optically tunable DFB-DBR coupled cavity laser emission was also observed as an external electric field can change the effective refractive index of a guided mode. We have investigated a 64 mm long Er-doped waveguide laser structure as shown in Fig 5.19a (sample: Pb145xz). A 10 mm long photorefractive grating was thermally fixed ($\lambda_B = 1561.5 \text{ nm}$ and $R = 30 \%$) within the 14 mm long Er,Fe-codoped waveguide section. Two gold stripes separated by $15 \mu\text{m}$ were deposited parallel to the waveguide. A dc voltage could be applied to the gold electrodes for electro-optic tuning. A tuning slope of about 0.5 pm/V ($\sim 64 \text{ MHz/V}$) was obtained (see Fig. 5.19b). Obviously, for the electro-optic tuning we could not utilize the highest electro-optic coefficient r_{33} ($30.8 \times 10^{-12} \text{ m/V}$) because of our X-cut and Z-propagating waveguide configuration. Instead, we utilized the r_{22} coefficient ($3.4 \times 10^{-12} \text{ m/V}$), which is almost one order of magnitude smaller than r_{33} . Although the electro-optic wavelength tuning range was not very large, stable single-frequency laser emission could be observed for several hours. Moreover, for further improvements the electro-optic tuning might be utilized for a fast feedback-controlled wavelength stabilization.

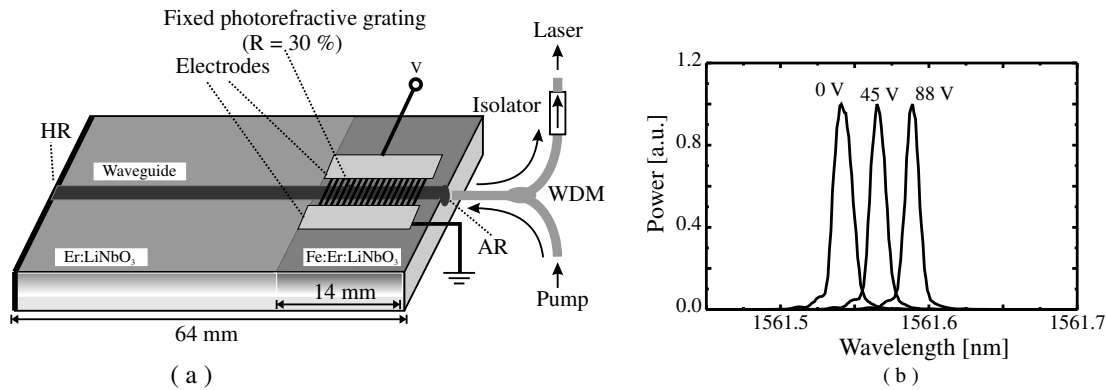


Fig. 5.19: Electro-optic wavelength tuning of a DFB-DBR coupled cavity laser (sample: Pb145xz): (a) schematic structure and (b) TE-polarized laser emission spectra corresponding to three different applied voltages. Pump power: 130 mW, TE-polarized.

Finally, temperature tuning of the emission wavelength of a DFB-DBR coupled cavity laser was also investigated. A change of the temperature of the whole device causes three different effects: (i) thermal expansion of the whole device (cavity) length, (ii) change of the refractive indices, and (iii) change of the grating periodicity due to thermal stretching (see also equation 4.2). Therefore, during temperature tuning switching between the two “DFB-lasing-modes” was frequently observed. However, most of the time single-frequency laser emission is favored: either right to the Bragg wavelength or left, as observed by an optical spectrum analyzer. With a careful observation of a particular “DFB-lasing-mode”, the thermal tuning experiment was performed. The observed tuning slope was ~ 5 pm/ $^{\circ}$ C when the whole device temperature was tuned from 15 to 70 $^{\circ}$ C. The device was not heated beyond 70 $^{\circ}$ C because the fixed photorefractive grating starts erasing slowly at temperatures > 80 $^{\circ}$ C.

5.7 Conclusions

Different types of integrated optical narrow linewidth DBR- and DFB-lasers ($1530 \text{ nm} < \lambda < 1575 \text{ nm}$) are demonstrated with Ti-indiffused Er-doped LiNbO_3 channel waveguides using thermally fixed photorefractive gratings. The general fabrication procedures of the three main building blocks of these devices e.g., gain section, single-mode waveguide, and thermally fixed photorefractive gratings are described along with their experimental characterization. The performance of the different laser configurations, i.e, DBR-laser with one grating, DBR-laser with two cavity gratings, DFB-laser/amplifier combination, and finally the DFB-DBR coupled cavity laser is presented in detail.

Single-frequency laser operation was obtained from the DBR-laser with two cavity gratings as well as from the DFB-DBR coupled cavity laser. Therefore, these lasers have applications in the field of interferometric sensing, e.g, the acousto-optic heterodyne interferometer [85] and in fiber-optic ultra-dense wavelength division multiplexed systems.

The stability of the emission wavelength and the output power of a laser are highly governed by the grating stability. An attractive way to stabilize the grating response is to utilize the green fluorescence in the Er-doped waveguides. Some results have also been obtained in this work. However, further investigations are required for its better utilizations.

Chapter 6

Summary and Conclusions

In this work different types of integrated optical DBR and DFB lasers ($1530 \text{ nm} < \lambda < 1575 \text{ nm}$) have been demonstrated in LiNbO_3 , using thermally fixed photorefractive Bragg gratings. They are fabricated on the surface of 1-mm-thick X-cut LiNbO_3 crystals with Ti-indiffused Z-propagating waveguides. Prior to a waveguide fabrication, the surface of the crystal is prepared with a laser-active section by Er-diffusion doping and a photorefractively sensitized section by Fe-diffusion doping. The photorefractive Bragg gratings could only be fabricated in the Fe-doped sections. Therefore, a combination of two types out of three differently doped single-mode waveguides, i.e, Ti:Er:LiNbO_3 (laser-active), Ti:Fe:LiNbO_3 (photorefractive-sensitive), and Ti:Fe:Er:LiNbO_3 (laser-active and photorefractive-sensitive) have been used for developing our different configurations of DBR and DFB lasers.

The origin of photorefractive effect, the principle of grating formation, and their thermal fixing mechanisms in Fe:LiNbO_3 have been discussed with theoretical illustrations. The coupled mode theory allows us to analyze the properties (transmission, reflections, FWHM, etc) of a photorefractive grating with gain (fabricated in Ti:Fe:LiNbO_3) or without gain (fabricated in Ti:Fe:Er:LiNbO_3). Theoretical calculations predict that a grating fabricated within the gain region ($\sim 4 \text{ dB/cm}$) could be operated as a DFB laser.

All the three types of waveguides, Ti:Er:LiNbO_3 , Ti:Fe:LiNbO_3 , and Ti:Fe:Er:LiNbO_3 have been investigated individually or in a combination of two. They were characterized in terms of losses, size of the guided mode(s), optical gain, and photorefractive sensitivity. Analyzing these results, the optimized fabrication parameters have been determined.

A compact holographic setup was developed with an argon laser ($\lambda = 488 \text{ nm}$, $P = 1 \text{ W}$) for the holographic recording of photorefractive gratings. Using this setup refractive index gratings of $L = 18 \text{ mm}$, $\lambda_B \sim 1.55 \mu\text{m}$, $R > 95\%$, and $\text{FWHM} < 60 \text{ pm}$, could be fabricated with a holographic exposure of $< 5 \text{ min}$. Such a refractive

index grating formed at room temperatures is volatile due to electronic conduction in the dark. Therefore, the holographic exposure is done at an elevated sample temperature (180 °C). At this temperature mobile H^+ ions form another grating that compensates the periodic spacecharge. Upon cooling of the sample, a permanent ionic grating is developed by a homogeneous illumination with blue light (from an array of blue LEDs).

Finally, a family of narrow linewidth integrated optical DBR, DFB, and DFB/DBR-coupled cavity lasers with Er-doped $LiNbO_3$ single-mode waveguide has been developed. They have one or two photorefractive gratings in Fe-doped waveguide sections. Antireflection (AR) and high-reflection (HR) coatings were deposited on the polished end faces accordingly where they are necessary. For laser operation, the pump light ($\lambda = 1480$ nm) is fed into the laser resonator through the grating via the common branch of a fibre-optic wavelength-division demultiplexer (WDM). The laser output is extracted through the second branch of the WDM and isolated to protect the laser from optical feedback.

Two types of DBR-lasers have been developed. The first type has a cavity consisting of one Bragg-grating in a Ti:Fe: $LiNbO_3$ waveguide, a gain section with Ti:Er: $LiNbO_3$ waveguide, and a multi-layer dielectric mirror deposited on one polished end face. Although, this laser was running with three longitudinal modes (in TE-polarization) but it stimulates for further investigations to achieve a single-frequency laser. Later on a second DBR-cavity comprised of two gratings in Ti:Fe: $LiNbO_3$ on both sides of the Er-doped waveguide has been developed. Single-frequency operation could be achieved in this case at various wavelengths in the Er-band (1530 nm $< \lambda < 1575$ nm) with up to 1.12 mW output power. Emission wavelength of this laser could also be tuned with temperature with a slope of about 8 pm/K.

For the first time, a DFB-laser with two lowest-order modes ($\lambda \sim 1531$ nm) has been demonstrated with a photorefractive grating in a Ti:Fe:Er: $LiNbO_3$ waveguide; it is combined with an integrated optical amplifier on the same substrate. The laser emission could be extracted from both sides: about 0.1 mW at the grating side and 1.1 mW at the amplifier side.

Moreover, an attractive DFB/DBR-coupled cavity laser has been developed and investigated. Its cavity consists of a photorefractive Bragg grating in the Ti:Fe:Er: $LiNbO_3$ waveguide section close to one end face of the sample, a Ti:Er: $LiNbO_3$ gain section and a broadband dielectric multi-layer mirror of high reflectivity on the other end face. The laser runs with single-frequency emission and a maximum output power of 8 mW. The emission wavelength of this type of laser is temperature tuned with a slope of 5 pm/K and electro-optically tuned with a slope of ± 0.75 pm/V.

In conclusion, using photorefractive Bragg gratings, four different types of lasers with

Er-doped LiNbO₃ waveguides have been investigated. Single-frequency laser operation is obtained from the DBR-laser with two cavity gratings as well as from the DFB/DBR coupled cavity laser. The linewidth of such a single-frequency laser can be as narrow as ~ 10 kHz [18], i.e, it has a very large coherence length ($\sim 3 \times 10^4$ m). Therefore, these lasers have applications in the field of interferometric instrumentation and in fiber-optic ultra-dense wavelength division multiplexed systems. A prospective immediate future work in this field could be the integration of one of the above mentioned single-frequency laser in an integrated optical heterodyne interferometer in LiNbO₃, which has also been developed in our group [85].

In spite of the above mentioned potentials, there are some difficulties to integrate these lasers with other optical components: the lasers are fabricated with Z-propagating waveguides in X-cut substrates. This is because efficient photorefractive Bragg gratings can only be fabricated in Z-propagating waveguides on a X- or Y-cut substrate. But the devices based on electro-optic/ acousto-optic effects (for tuning, modulation, switching, etc.), usually have waveguides aligned either parallel to the Y- or to X-axis. However, we are optimistic as there are some efforts to fabricate photorefractive Bragg gratings even in waveguides fabricated in Z-cut substrates [86].

Bibliography

- [1] K. Nassau, H.J. Levinstein, and G.M. Loiacono. “Ferroelectric lithium niobate. 1. Growth, domain structure, dislocations and etching”. *J. Phys. Chem. Solids*, 27:983–988, 1966.
- [2] K. Nassau, H.J. Levinstein, and G.M. Loiacono. “Ferroelectric lithium niobate. 2. Preparation of single domain crystals”. *J. Phys. Chem. Solids*, 27:989–996, 1966.
- [3] S.C. Abrahams, J.M. Reddy, and J.L. Bernstein. “Ferroelectric lithium niobate. 3. Single crystal x-ray diffraction study at 24°C”. *J. Phys. Chem. Solids*, 27:997–1012, 1966.
- [4] S.C. Abrahams, W.C. Hamilton, and J.M. Reddy. “Ferroelectric lithium niobate. 3. Single crystal neutron diffraction study at 24°C”. *J. Phys. Chem. Solids*, 27:1013–1018, 1966.
- [5] S.C. Abrahams, H.J. Levinstein, and J.M. Reddy. “Ferroelectric lithium niobate. 3. Polycrystal x-ray diffraction study between 24° and 1200°C”. *J. Phys. Chem. Solids*, 27:1019–1026, 1966.
- [6] A. Räuber. “Chemistry and physics of lithium niobate”. *Current Topics in Materials Science*, I, edited by E. Kaldis:481–601, 1978.
- [7] R.S. Weis and T.K. Gaylord. “Lithium niobate: Summary of physical properties and crystal structure”. *Applied Physics A*, 37:191–203, 1985.
- [8] P.G. Suchoski and F.J. Leonberger. “Commercialization of lithium niobate modulators”. *Integrated Optical Circuits and Components: Design and Applications; Series of Optical Engineering*, 66:9–19, 1999.
- [9] E. Lallier, J.P. Pocholle, M. Papuchon, C. Grezes-Besset, M. De Micheli, M.J. Li, Q. He, and D.B. Ostrowski. “Laser oscillation of single mode channel waveguide in Nd:MgO:LiNbO₃”. *Electronics Letters*, 25:1491–1492, 1989.
- [10] R. Brinkmann, W. Sohler, H. Suche, and Ch. Wersig. “Single mode Ti-diffused optical strip guides and lasers in Nd:MgO:LiNbO₃”. *Tech. Dig. Integrated Photonics Res.*, 5:116–117, 1990.

- [11] E. Lallier, J.P. Pochole, M. Papuchon, Q. He, M. De Micheli, D.B. Ostrowski, C. Grezes-Besset, and E. Pelletier. "Integrated Nd:MgO:LiNbO₃ FM mode-locked waveguide laser. *Electronics Letters*, 27:936–937, 1991.
- [12] E. Lallier, D. Papillon, J.P. Pochole, M. Papuchon, M. De Micheli, and D.B. Ostrowski. "Short pulse, high power Q-switched Nd:MgO:LiNbO₃ waveguide laser". *Electronics Letters*, 29:175–176, 1993.
- [13] J. Amin, M. Hempsted, J.E. Roman, and J.S. Wilkinson. "Tunable coupled-cavity waveguide laser at room temperature in Nd-diffused Ti:LiNbO₃". *Optics Letters*, 19:1541–1543, 1994.
- [14] J.P. de Sandro, J.K. Jones, D.P. Shepherd, J. Webjörn, M. Hempsted, J. wang, and A.C. Tropper. "Tm³⁺ indiffused LiNbO₃ waveguide lasers". *7th Eur. Conf. Intgr. Optics (ECIO '95), Delft, The Netherlands*, pages 17–20, 1995. post deadline papers.
- [15] J.K. Jones, J.P. De Sandro, M. Hempsted, D.P. Shepherd, A.C. Large, A. C. Tropper, and J.S. Wilkinson. "Channel waveguide laser at 1 μ m in Yb-indiffused LiNbO₃". *Optics Letters*, 20:1477–1479, 1995.
- [16] W. Sohler and H. Suche. "Erbium-doped lithium niobate waveguide devices". *Integrated Optical Circuits and Components: Design and Applications; Series of Optical Engineering*, 66:127–159, 1999.
- [17] I. Baumann, S. Bosso, R. Brinkmann, R. Corsini, M. Dinand, A. Greiner, K. Schäfer, J. Söchtig, W. Sohler, H. Suche, and R. Wessel. "Er-doped integrated optical devices in LiNbO₃". *IEEE J. Sel. Topics in Quantum Electron.*, 2:355–366, 1996.
- [18] C. Becker, T. Oesselke, J. Pandavenes, R. Ricken, K. Rochhausen, G. Schreiber, W. Sohler, H. Suche, R. Wessel, S. Balsamo, I. Montrosset, and D. Sciancalepore. "Advanced Ti:ErLiNbO₃ waveguide lasers". *IEEE Trans. Sel. Top. Quantum Electron.*, 6:1–13, 2000.
- [19] J. Söchtig, R. Gross, I. Baumann, W. Sohler, H. Schütz, and R. Widemer. "DBR waveguide laser in erbium-diffused-doped LiNbO₃". *Electronics Letters*, 31:351–352, 1995.
- [20] Ch. Becker, A. Greiner, Th. Oesselke, A. Pape, W. Sohler, and H. Suche. "Integrated optical Ti:Er:LiNbO₃ distributed Bragg reflector laser with a fixed photorefractive grating". *Optics Letters*, 23(15):1194–1196, 1998.
- [21] J.E. Carroli, J. Whiteaway, and D. Plumb. *Distributed feedback semiconductor lasers*. ISBN 0-85296-917-1. IEE, 1998.

- [22] G. Morthier and P. Vankwikelberge. *Handbook of distributed feedback laser diodes*. ISBN 0-89006-607-8. Artech House Inc., 1997.
- [23] M.C. Amann and J. Buus. *Tunable laser diodes*. ISBN 0-89006-963-8. Artech House Inc., 1998.
- [24] G. A. Ball and W. W. Morey. “Continuously tunable single-mode erbium fiber laser”. *Optics Letters*, 17:420–422, 1992.
- [25] J. L. Zyskind, V. Mizrahi, D. J. DiGiovanni, and J. W. Sulhoff. “Short single frequency erbium-doped fiber laser”. *Electron. Lett.*, 28:1385–1387, 1992.
- [26] G.A. Ball, C.E. Holton, G. Hull-Allen, and W.W. Morey. “60 mW 1.5 μm single frequency low noise fiber laser MOPA”. *IEEE Photon. Technol. Lett.*, 6:192–194, 1994.
- [27] J.T. Kringlebotn, J.-L. Archambault, L. Reekie, J.E. Townsend, G.G. Vienne, and D.N. Payne. “Highly efficient, low noise grating feedback $\text{Er}^{3+}:\text{Yb}^{3+}$ codoped fiber laser. *Electron. Lett*, 30:972–973, 1994.
- [28] W.H. Loh and R. I. Laming. “1.55 μm phase-shifted distributed feedback fiber laser”. *Electron. Lett.*, 31:1440–1442, 1995.
- [29] M. Sejka, P. Varming, J. Hubner, and M. Kristensen. “Distributed feedback Er^{3+} -doped fiber laser. *Electron. Lett.*, 31:1445–1446, 1995.
- [30] W.H. Loh, B.N. Samson, L. Dong, G. J. Cowle, and K. Hsu. “High performance single frequency fiber grating-based Erbium:Ytterbium-codoped fiber lasers”. *IEEE J. Lightwave Technol*, 16:114–118, 1998.
- [31] J. Söchtig, H. Schütz, R. Widmer, R. Corsini, D. Hiller, C. Carmannini, G. Consonni, S. Bosso, and L. Gobbi. “Monolithically integrated DBR waveguide laser and intensity modulator in erbium-doped LiNbO_3 ”. *Electronics Letters*, 32:899–900, 1996.
- [32] A. Yariv and M. Nakamura. “Periodic structures for integrated optics”. *IEEE Journal of Quantum Electronics*, QE-13:233–253, 1977.
- [33] T. Suhara and H. Nishihara. “Integrated optics components and devices using periodic structures”. *IEEE Journal of Quantum Electronics*, QE-22:845–867, 1986.
- [34] B.K. Das, H. Suche, and W. Sohler. “Single Frequency $\text{Ti}:\text{Er}:\text{LiNbO}_3$ Distributed Bragg Reflector (DBR)- Waveguide Laser with Two Integrated Photorefractive Gratings”. *Proc. Eur. Conf. Integr. Optics - 01, Paderborn*, pages 87–90, 2001.

- [35] B.K. Das, H. Suche, and W. Sohler. Single-frequency Ti:Er:LiNbO₃ distributed bragg reflector waveguide laser with thermally fixed photorefractive cavity. *Applied Physics B*, 73:439–442, 2001.
- [36] B.K. Das, R. Ricken, and W. Sohler. “Integrated optical DFB-laser with Ti:Fe:Er:LiNbO₃ waveguide”. *Proc. Conf. Laser and Electro-Optics - 02, Post Deadline Papers*, pages CPDB11.1–CPDB11.3, 2002.
- [37] B.K. Das, R. Ricken, and W. Sohler. “Integrated optical distributed feedback laser with Ti:Fe:Er:LiNbO₃ waveguide”. *Applied Physics Letters*, 82:1515–1517, 2003.
- [38] B.K. Das, R. Ricken, V. Quiring, H. Suche, and W. Sohler. “DFB-DBR coupled cavity laser in Ti:Fe:Er:LiNbO₃”. *Proc. Eur. Conf. Opt. Comm.-02, Copenhagen, Denmark*, 4:11.2.2, 2002.
- [39] B.K. Das, R. Ricken, V. Quiring, H. Suche, and W. Sohler. “DFB-DBR coupled cavity laser with Ti:(Fe):Er:LiNbO₃ waveguide”. *Optics Lett.*, to be submitted.
- [40] M. Taya, M.C. Bashaw, and M.M. Fejer. “Photorefractive effects in periodically poled ferroelectrics”. *Optics Letters*, 21:857–859, 1996.
- [41] J.J. Amodei and D.L. Staebler. Holographic pattern fixing in electro-optic crystals. *Applied Physics Letters*, 18:540–542, 1971.
- [42] K. Buse, A. Adibi, and D. Psaltis. “Non-volatile holographic storage in doubly-doped lithium niobate”. *Nature*, 393:665–668, 1998.
- [43] J. Hukriede, I. Nee, D. Kip, and E. Krätzig. “Thermally fixed reflection gratings for infrared light in LiNbO₃:Ti:Fe channel waveguides”. *Optics Letters*, 23:1405–1407, 1998.
- [44] A. Ashkin, G.D. Boyd, J.M. Dziedzic, R.G. Smith, A. A. Ballman, J.J. Levinstein, and K. Nassau. “Optically-induced refractive index inhomogeneities in LiNbO₃ and LiTaO₃”. *Applied Physics Letters*, 9:72–74, 1966.
- [45] F.S. Chen, J.T. LaMacchia, and D.B. Fraser. “Holographic Storage in Lithium Niobate”. *Applied Physics Letters*, 13:323–325, 1968.
- [46] A.M. Glass. “The photorefractive effect”. *Optical Engineering*, 17:470–479, 1978.
- [47] N.V. Kukhtarev, V.B. Markov, S.G. Odulov, M.S. Soskin, and V.L. Vinetskii. “Holographic storage in electrooptic crystals: I. Steady state”. *Ferroelectrics*, 22:949–960, 1979.
- [48] N.V. Kukhtarev, V.B. Markov, S.G. Odulov, M.S. Soskin, and V.L. Vinetskii. “Holographic storage in electrooptic crystals: II. Beam coupling - Light Amplification”. *Ferroelectrics*, 22:961–964, 1979.

- [49] G.E. Peterson, A.M. Glass, and T.J. Negran. “Control of the susceptibility of lithium niobate to laser-induced refractive index changes”. *Applied Physics Letters*, 19:130–132, 1971.
- [50] A.M. Glass, D. von der Linde, and T.J. Negran. “High-voltage bulk photovoltaic effect and the photorefractive process in LiNbO_3 ”. *Applied Physics Letters*, 25:233–235, 1974.
- [51] F. Jermann, M. Simon, and E. Krätzig. “Photorefractive properties of congruent and stoichiometric lithium niobate at high light intensities”. *Journal of the Optical Society of America B*, 12:2066–2070, 1995.
- [52] V.I. Belinicher, V.K. Malinowski, and B.I. Sturman. “Photogalvanic effect in a crystal with polar axis”. *Sov. Phys. JETP*, 46:362–366, 1977.
- [53] J.F. Nye. *Physical Properties of Crystals*. Clarendon Press, 1957.
- [54] H.G. Festl, P. Hertel, E. Krätzig, and R. von Baltz. “Investigations of the photovoltaic tensor in doped LiNbO_3 ”. *Phys. Stat. Sol. (b)*, 113:157–164, 1982.
- [55] P. Günter and J.P. Huignard. *Photorefractive Materials and Their Applications I*, volume 61. Springer-Verlag, 1988.
- [56] F.T.S. Yu and S. Yin. *Photorefractive Optics*. Academic Press, 2000.
- [57] R. Sommerfeldt, L. Holtmann, E. Krätzig, and B.C. Grabmaier. “Influence of Mg doping and composition on the light induced charge transport in LiNbO_3 ”. *Phys. Stat. Sol.*, 106:89–98, 1988.
- [58] H. Vormann, G. Weber, S. Kapphan, and E. Krätzig. “Hydrogen as origin of thermal fixing in $\text{LiNbO}_3:\text{Fe}$ ”. *Solid State Comm.*, 40:543–545, 1981.
- [59] M. Carrascosa and F. Agullo-Lopez. “Theoretical modeling of the fixing and developing of holographic gratings in LiNbO_3 ”. *Journal of the Optical Society of America B*, 7:2317–2322, 1990.
- [60] A. Yariv. “Coupled-mode theory for guided wave optics”. *IEEE Journal of Quantum Electronics*, QE-9:919–933, 1973.
- [61] D. Marcuse. “Optimal electrode design for integrated optic modulators”. *IEEE Journal of Quantum Electronics*, QE-18:393–398, 1982.
- [62] E. Strake, G.P. Bava, and I. Montrosset. “Guided modes of $\text{Ti}:\text{LiNbO}_3$ channel waveguides: a novel quasianalytical technique in comparison with the finite element method”. *IEEE Journal of Lightwave Technology*, 6:1126–1135, 1988.

- [63] N.H. Zhu, X.S. Zheng, Y.K. Lin, and X. Yu. “Calculation of the field distribution of a Ti:LiNbO₃ optical waveguide and its applications”. *Optical and Quantum Electronics*, 24:737–743, 1992.
- [64] D. Zhang, G. Ding, and C. Chen. “Theoretical analysis of guided mode and effective refractive index profiles at 1.53 μ m in Ti:LiNbO₃ strip waveguides”. *IEEE Journal of Lightwave Technology*, 16:459–464, 1998.
- [65] B.K. Das, P. Ganguly, J.C. Biswas, and S.K. Lahiri. “Modeling of titanium indiffused lithium niobate optical waveguide by variational method”. *SPIE Proceedings*, 3666:193–198, 1999.
- [66] H. Kogelnik. “Filter response of nonuniform almost-periodic structures”. *The Bell Sys. Tech. Journal*, 55:109–126, 1976.
- [67] R. Brinkmann, I. Baumann, M. Dinand, W. Sohler, and H. Suche. “Erbium-doped single- and double-pass Ti:LiNbO₃ waveguide amplifiers”. *IEEE Journal of Quantum Electronics*, 30:2356–2360, 1994.
- [68] B.K. Das, K. Kamaldev, P. Ganguly, J.C. Biswas, and S.K. Lahiri. “Simulation of gain characteristics of erbium-doped titanium indiffused lithium niobate optical waveguide amplifiers”. *J. Optics*, 27:37–47, 1998.
- [69] B.K. Das, R. Chakraborty, P. Ganguly, J.C. Biswas, and S.K. Lahiri. “Design of high-gain integrated optic amplifier using erbium-doped titanium indiffused lithium niobate optical waveguide”. *Proc. Int. Conf. on Computer and Devices for Commun., Calcutta/India*, 1:571–574, 1998.
- [70] I. Baumann, R. Brinkmann, M. Dinand, W. Sohler, L. Beckers, C. Buchal, M. Fleuster, H. Holzbrecher, H. Paulus, K.H. Müller, T. Gog, G. Materlik, O. Witte, H. Stolz, and W. von der Osten. “Erbium incorporation in LiNbO₃ by diffusion doping”. *Applied Physics A*, 64:33–44, 1997.
- [71] J. Crank. *The Mathematics of Diffusion*. Clarendon Press, 2nd edition, 1975.
- [72] J.M. Cabrera M. Carrascosa and F. Agullo-Lopez. “Steady holographic gratings formed in photorefractive materials: Influence of material parameters”. *IEEE Journal of Quantum Electronics*, 27:509–515, 1991.
- [73] K. Buse, S. Breer, K. Peithmann, S. Kapphan, M. Gao, and E. Krätzig. “Origin of thermal fixing in photorefractive lithium niobate crystals”. *Phys. Rev. B*, 56:1225–1235, 1997.
- [74] R. Regener and W. Sohler. “Loss in low-finesse Ti:LiNbO₃ optical waveguide resonators”. *Applied Physics B*, 36:143–145, 1985.

- [75] V.T. Gabrielyan, A.A. Kaminskii, and L. Li. “Absorption and luminescence spectra and energy levels of Nd^{3+} and Er^{3+} ions in LiNbO_3 ”. *Phys. Stat. Sol. (a)*, 3:K37–K42, 1970.
- [76] R. Brinkmann. *Integrierte optische verstärker in erbium dotiertem LiNbO_3* . Dissertation, Dept. of Applied Physics, University of Paderborn, Germany, 1994.
- [77] Christian Becker. “Integrierte optische DBR-laser mit photorefraktivengittern in erbiumdotiertem LiNbO_3 ”. 1997.
- [78] R. Müller, J.V. Alveraz-Bravo, L. Arizmendi, and J.M. Cabrera. “Tuning of photorefractive interference filters in LiNbO_3 ”. *J. Phys. D: Appl. Phys.*, 27:1628–1632, 1994.
- [79] M. Dinand. *Modellierung erbiumdotierter integriert optischer verstärker und laser in LiNbO_3* . Dissertation, Dept. of Applied Physics, University of Paderborn, Germany, 1995.
- [80] I. Baumann, R. Brinkmann, M. Dinand, W. Sohler, and S. Westenhöfer. “Ti:Er: LiNbO_3 waveguide laser of optimized efficiency”. *IEEE Journal of Quantum Electronics*, 32:1695–1706, 1996.
- [81] M. Dinand and W. Sohler. “Theoretical modeling of optical amplification in Er-doped Ti: LiNbO_3 waveguides”. *IEEE Journal of Lightwave Technology*, 30:1267–1276, 1994.
- [82] H. Kogelnik and C.V. Schank. “Coupled mode theory of distributed feedback laser”. *Journal of Applied Physics*, 43:2327–2335, 1972.
- [83] S. Wang. “Principles of distributed feedback and distributed Bragg reflector lasers”. *IEEE Journal of Quantum Electronics*, QE-10:413–427, 1974.
- [84] S. Wang, R.F. Cordero, and C. Tseng. “Analysis of distributed-feedback and distributed-Bragg-reflector laser structures by method of multiple reflections”. *Journal of Applied Physics*, 45:3975–3977, 1974.
- [85] A. Rubiyanto, H. Herrmann, R. Ricken, F. Tien, and W. Sohler. “Integrated optical heterodyne interferometer in lithium niobate”. *J. Nonlinear Optical Physics and Materials*, 10:163–168, 2001.
- [86] S.M. Kostritskii, Y.N. Korkishko, V.A. Fedorov, R.F. Tavlykaev, and R.V. Ramaswamy. “Integrated optical Ti:Cu: LiNbO_3 distributed Bragg reflector with a photorefractive waveguide grating”. *Proc. SPIE*, 4944, 2003.

Acknowledgement

First of all I would like to express my gratefulness to Prof. Wolfgang Sohler who had kindly accepted me as one of his Ph.D. student nearly four years ago. I must admit that I was fortunate to get an opportunity for my Ph.D. study in an internationally recognized “Integrated Optics Group” headed by a personality like him. During my stay here in Paderborn, I have been benefitted enormously by his excellent guidance not only in academic research but also in everyday-life. After all, Prof. Sohler contributed this thesis work by many helpful discussions and advice.

This work has been carried out under one of the research project of the Integrated Optics Group, “Integrated Optics in LiNbO₃: New Devices, Circuits, and Applications” sponsored by Deutsche Forschungsgemeinschaft (DFG). I am thankful to DFG and the people those who are involved directly or indirectly in this project.

For pursuing my thesis work, I got enormous technological help from Raimund Ricken, Katja Rochhausen, and Viktor Quiring. Without their meaningful cooperations in different sample preparations, this work could not be finished in time. Moreover, I have been acquainted with lots of technological idea from them.

I am specially grateful to Dr. Hubertus Suche, from whom I got help in many fronts. Besides academic discussions, he helped me to build an e-beam evaporation system for iron deposition: an old e-gun was installed inside an old vacuum chamber lying in the junk room, but the system is working as good as new one. The copper holder used in the Lloyd setup was also designed by Dr. Suche. Finally, I am thankful to him for his careful corrections and suggestions for preparing this thesis.

In course of my work, I also got seniors like Klaus Schäfer, Rudolf Wessel, Agus Rubyanto, Ulrich Rust and Harald Hermann. They helped me a lot in terms of teaching me integrated optics, introducing different experimental equipments and giving me valuable friendships. Particularly, I can’t express in words the help I got from Klaus, Rudi, and Rubi for my initial settlement in Paderborn. Thanks also goes to my other friends, like Selim Reza, Yeung-Lak Lee, Yoo Hong Min, Ansgar Hellwig, Marc Hübner, Jie Hun Lee, Suhas Bhandare, and Indira Choudhuri from whom I was benefitted in many ways in everyday life. My special thanks goes to our secretary Mrs. Irmgard Zimmermann who not only assisted me in all the official works but also

helped me for my smooth settlement in Paderborn. Whenever I used to get in trouble, either in the office or in my everyday-life, she always extends her helping hands as the troubleshooter!

Finally, I should admit that I got the most valuable cooperation from my family: my wife Susama, and our sweet twins - Satadru and Bipasa. I must confess that I was extremely cruel to leave them alone from 8-00 am to 10-00 pm. Yes, that is almost everyday! I hope they have already got some taste - What is a Ph.D!

Bijoy Krishna Das

March 2003